MICROCOPY RESOLUTION TEST CHART
NATIONAL BUREAU OF STANDARDS 1963 A

LEVEL

AERODYNAMICALLY INDUCED VIBRATION

EDR 10840

Robert L. Jay

James L. Bettner

September 1981

82 03 02 050

Detroit Diesel Allison
Division of General Motors Corporation

P.O. Box 894 Indianapolis. Indiana 46206

Qualified requestors may obtain
additional copies from the Defense
Technical Information Service.

Conditions of Reproduction

Reproduction, translation, publication,
use and disposal in whole or in part by
or for the United States Government is
permitted.

REPORT DOCUMENTATION PAGE	READ INSTRUCTIONS BEFORE COMPLETING FORM

1. REPORT NUMBER	2. GOVT ACCESSION NO.	3. RECIPIENT'S CATALOG NUMBER
AFOSR-TR- 82-0011	AD-110493	

4. TITLE (and Subtitle)	5. TYPE OF REPORT & PERIOD COVERED
AERODYNAMICALLY INDUCED VIBRATION	INTERIM 1 JUN 80 – 31 JUL 81
	6. PERFORMING ORG. REPORT NUMBER

7. AUTHOR(s)	8. CONTRACT OR GRANT NUMBER(s)
ROBERT L JAY J L BETTNER	F49620-80-C-0078

9. PERFORMING ORGANIZATION NAME AND ADDRESS	10. PROGRAM ELEMENT, PROJECT, TASK AREA & WORK UNIT NUMBERS
DETROIT DIESEL ALLISON, DIV. GMC PO BOX 894 INDIANAPOLIS, IN 46206	2307/A1 61102F

11. CONTROLLING OFFICE NAME AND ADDRESS	12. REPORT DATE
AIR FORCE OFFICE OF SCIENTIFIC RESEARCH/NA BOLLING AFB, DC 20332	SEP 81
	13. NUMBER OF PAGES 126

14. MONITORING AGENCY NAME & ADDRESS(if different from Controlling Office)	15. SECURITY CLASS. (of this report)
	UNCLASSIFIED
	15a. DECLASSIFICATION/DOWNGRADING SCHEDULE

16. DISTRIBUTION STATEMENT (of this Report)

Approved for public release; distribution unlimited.

17. DISTRIBUTION STATEMENT (of the abstract entered in Block 20, if different from Report)

18. SUPPLEMENTARY NOTES

19. KEY WORDS (Continue on reverse side if necessary and identify by block number)

FORCED VIBRATION	UNSTEADY FLOW
AERODYNAMICALLY INDUCED VIBRATION	AXIAL FLOW COMPRESSOR
TURBOMACHINERY	ENDWALL BOUNDARY LAYER FLOWS

20. ABSTRACT (Continue on reverse side if necessary and identify by block number)

An experimental investigation, performed in a large scale low-speed, single-stage compressor, was conducted to provide the radial and chordwise distribution of basic unsteady pressure data on the stator. Radial and circumferential distributions of streamwise and transverse velocity fluctuations were determined at stations upstream, inside and immediately downstream of the stator. Analysis of the results indicated a correlation of the normalized transverse fluctuation velocity component with stator incidence angle. The

DD FORM 1473   1 JAN 73   EDITION OF 1 NOV 65 IS OBSOLETE

fluctuations were very large in the endwall regions and were attributed to poor flow conditions generated in the hub and tip endwall regions of the rotor.

TABLE OF CONTENTS

1

LIST OF ILLUSTRATIONS

3

4

5

LIST OF TABLES

I. INTRODUCTION

The demand for advanced, high-performance aircraft gas turbine engines that feature high thrust-to-weight ratios with increased fuel economy and durability has created a need for the development of analytical techniques for predicting the structural response of airfoils under the influence of periodic aerodynamic loading. The technical areas that must be correctly formulated in an ideal predictive model are (1) structural dynamics, (2) structural damping, (3) aerodynamic forcing function, and (4) aerodynamic damping.

Of the four areas, structural dynamics is best understood at this time. Models using finite element concepts have been correlated with stationary, individual airfoil and bladed disk experimental frequencies to demonstrate close agreement. This agreement has provided the background necessary for predicting frequencies of rotating systems. Current experimental research is directed toward verification of models in the rotating frame.

Structural damping calculations have been and continue to be an empirically based process. Material or hysteresis damping and coulomb/sliding friction comprise structural damping. Analytical models of structural damping are currently being developed, but are unavailable at this time.

The aerodynamic forcing function denotes the time-variant loading created on an airfoil or disk. This loading can be created either by passage of the airfoil or disk through perturbations in an otherwise uniform aerodynamic field or by passage of a similar field beyond a stationary airfoil or disk. Examples of this are a rotating airfoil passing through the potential field created by a downstream stator or a downstream stator being acted upon by the wakes from upstream rotor airfoils. Predictive techniques for the aerodynamic forcing functions need to be greatly improved as current techniques are based on unloaded flat plates operating in compressible, inviscid flow fields.

9

Aerodynamic damping defines the resistance of an airfoil to movement due to energy dissipated in the surrounding aerodynamic field. Flutter, generally considered to be created by negative aerodynamic damping, defines the condition in which an airfoil moves and, in so moving, absorbs energy from the surrounding aerodynamic field. This damping, positive or negative, is currently assessed by use of models that have the same severe limitations as those in the forcing function models.

Thus, analytical investigations are needed in each of the four areas that comprise the field of aeroelasticity. Each area must be investigated thoroughly, not only through analysis, but also by using experimental results for definition and discovery of the key physical parameters.

Detroit Diesel Allison (DDA) has been gathering experimental data from a large diameter, low-speed compressor stage to address the specific problem of wake-induced aerodynamic loading of a stator vane. This work has been accomplished under Air Force Office of Scientific Research (AFOSR) funding in Contracts F49620-74-C-0065, F49620-77-C-0024, and F49620-78-C-0070.

Measurements of the upstream rotor wake and the resultant time-variant pressures on the surface of the stator vane have been used to examine the credibility of existing predictive techniques. Results indicate that the linear, inviscid models, which assume zero thickness, unloaded flat plates for the airfoil, predict surface pressures well if the incidence angle remains near zero. When the incidence angle becomes more negative, then significant differences between the measured and predicted values begin to develop due to convected wave motion on the stator surface.

This reaction raises question concerning the use of unconnected aerodynamic strips at various radial cuts to predict the full span aerodynamic loading. Since endwall effects created by secondary, viscous flows substantially affect the air inlet angles to a stator row, realistic stators operate with large incidence angles at the hub and tip and with low incidence angles prevalent only in the region of the midspan radius. The extent to which a stator is influenced by interactions between these high and near-zero incidence regions determines, in part, the ultimate usefulness of the zero-loaded, flat plate aerodynamic models.

10

The purpose of the experimental program described in this report was to quantitatively examine the radial and chordwise loading on a stator airfoil operating in the wakes of an upstream rotor stage. To accomplish this, the time-based definition of the rotor wake was needed, as it passes through the stator passage and the surface pressures on the stator surfaces.

The results of this investigation in terms of surface pressures and wake perturbation velocities are included in this report. Conclusions and observations based on examination of these results are presented for consideration.

II. TEST CONFIGURATION

The test facility used in this experimental study was the DDA low-speed rotating cascade. This single-stage compressor rig features blading with an outer diameter of 48.0 in. and a hub/tip radius ratio of 0.80 in. Thus, the rotor blades and stator blades are large, allowing detailed aerodynamic measurements to be made. The chord of the rotor blades measures 4.489 in., the stator blades, 5.089 in. The design tip speed of the rotor is 183.5 ft/sec, resulting in a design-corrected rotor speed of 876.3 rpm. The 42 rotor blades and 40 stator blades have NACA 65 series profiles. No radial blockage was used in this study and the rotor blade tip clearance was 0.140 in. or 3% of span.

The single stage was designed to have aerodynamic loading and geometric characteristics that are representative of the aft stages of modern compressors. Table 1 contains more specific information regarding airfoil section data and compressor design point conditions. Figure 1 shows the rig assembled without rotor blading, which would normally be located immediately upstream of the visible stators. In Figure 2 the stators are shown installed in the static casing. The research compressor was driven by a 50 hp D/C motor.

Table 1.
Airfoil mean section characteristics and
compressor design point conditions.

	Rotor	Stator
Type of airfoil	65 series	65 series
Number	42	40
Chord, C--in.	4.589	5.089
Solidity, $\sigma = c/s$	1.435	1.516
Camber, ϕ--deg	20.42	48.57
Aspect ratio, AR = 1/C	1.046	0.943
Leading edge radius/C	0.0044	0.0049
Trailing edge radius/C	0.0028	0.0030
Inlet angle, β_1--deg	59.38	37.84
Exit angle, β_2--deg	42.41	0.00

13

Table 1. (Cont)

	Rotor	Stator
Flow rate, $W \sqrt{\theta}/\delta$	31.02 lb/sec	
Tip speed, $U_t/\sqrt{\theta}$	183.5 ft/sec	
Rotational speed, $N/\sqrt{\theta}$	876.3 rpm	
Stage pressure ratio	1.012	
Inlet tip radius	24.00 in.	
Hub/tip radius ratio	0.80	
Stage efficiency--%	88.1	
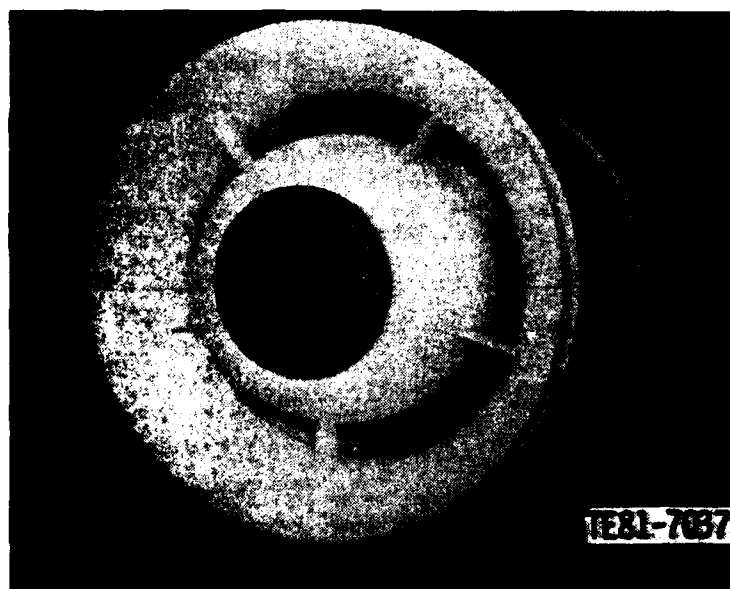
Figure 1. View of assembled single-stage research compressor.
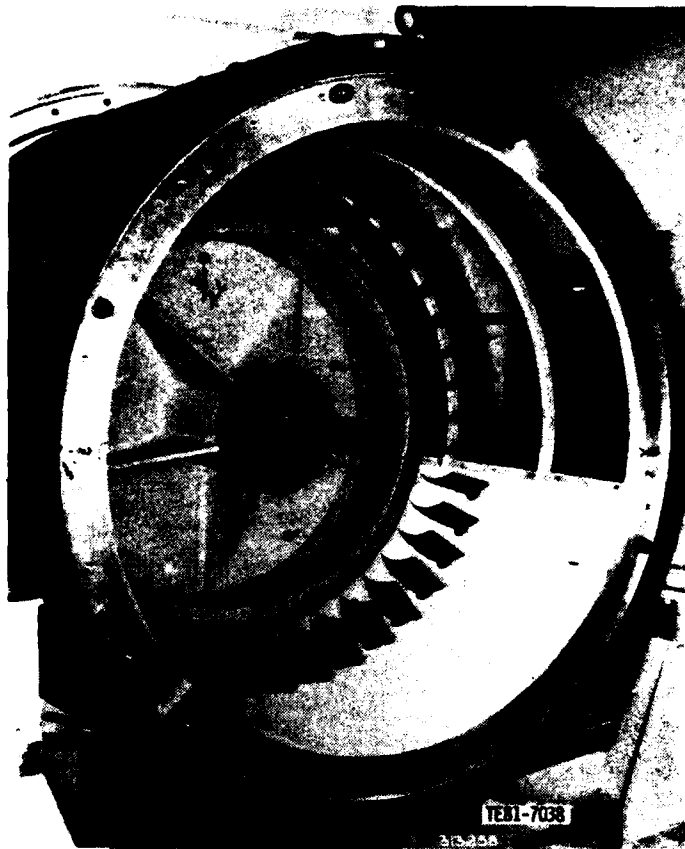
Figure 2. View of single-stage research compressor stator row.

Steady-state operation of the compressor rig is defined by static and total pressures and temperatures at the inlet to the rotor stage and the exit to the stator. On-line computations are made of the velocity fields into the rotor and out of the stator. In addition, operating total pressure ratio and corrected mass flow rate are calculated. A computer, which interrogates a 6-channel (48 ports per channel) Scannivalve and temperature junction boxes, is used for these on-line computations.

For time-variant measurements, miniature pressure transducers and a crossed-wire probe are used. Kulite thin-line transducers are located on the surfaces of four stator airfoils. These transducers are flush-mounted by grooving the surface. The grooves, designed to accommodate the transducer, bonding agent, and lead wires, extend from the particular transducer through the stator trun-

15

nion. The grooves are clearly seen in Figure 3 on two of the instrumented
airfoils used in this experimental program. Figure 4 shows the location of
the Kulite pressure transducers on the remaining two instrumented airfoils.
Table 2 lists radial and axial locations of the instrumentation on the stator
airfoils. Figure 5 is a schematic of the instrumented airfoils showing the
numbering system used. A view of the crossed-wire probe used in the experi-
ment is shown in Figure 6. In this photograph the wire is located near the
center span instrumented airfoils.

The rotor wake was measured at four axial locations: approximately 10% of
axial chord upstream of the stators, 12% of axial chord downstream of the sta-
tor row, 13% of axial chord from leading edge, and 73% of axial chord from
leading edge. Circumferential and radial surveys were obtained at each of
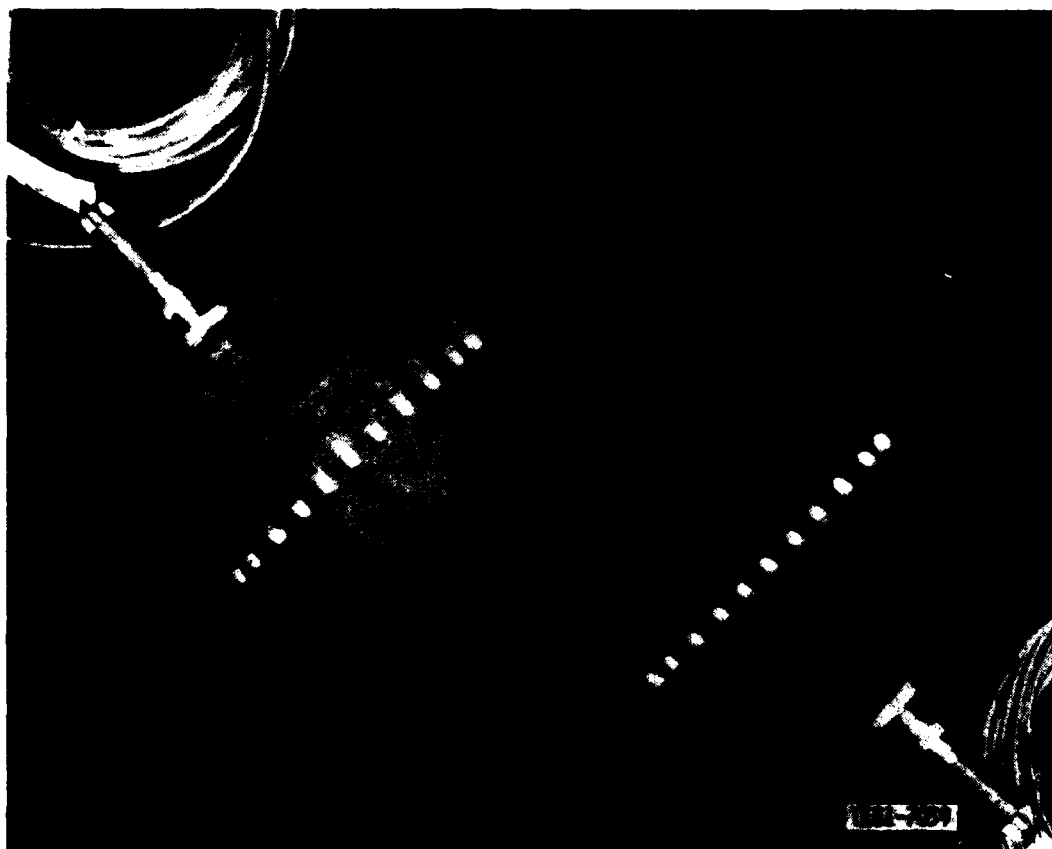
Figure 3. Dynamically instrumented stator vanes.

Figure 4. Radial and chordwise suction and pressure surface transducer
instrument locations.

these axial stations. For the locations forward and aft of the stator row, an
L. C. Smith actuation system shown in Figure 7 was used to provide circumfer-
ential, radial, and yaw movements of the hot wire. For the intrapassage mea-
surements, the hardware shown in Figure 8 was designed and fabricated. This
figure shows a Kulite total pressure probe installed. In the actual experi-
ment, a DISA cross hot wire was used. The hot wire was installed on the
slider assembly at the aft traverse location (73% axial chord). The blank-off
plate for sealing at the forward traverse location (13% axial chord) is seen
immediately forward of the stator trunnions.

Table 2.
Location of Kulites transducers on stators.

Kulite number	% Span from tip	% X/C from leading edge
1	50	2.94
2	50	10.0
3	50	20.0
4	50	30.0
5	50	40.0
6	50	50.0
7	50	60.0
8	50	70.0
9	50	80.0
10	50	90.0
11	50	97.0

		Pressure surface	Suction surface
12	5.0	3.5	2.0
13	5.0	14.4	13.7
14	5.0	45.0	45.3
15	5.0	74.9	75.5
16	5.0	89.6	90.4
17	25.0	3.5	2.0
18	25.0	89.6	90.4
19	50.0	3.5	2.0
20	70.0	3.5	2.0
21	70.0	89.6	90.4
22	90.0	3.5	2.0
23	90.0	14.4	13.7
24	90.0	45.0	45.3
25	90.0	74.9	75.5
26	90.0	89.6	90.4

Blades 19, 20   Tip

Leading
edge   ○ ○ ○ ○ ○ ○ ○ ○ ○ ○ ○
          1 2 3 4 5 6 7 8 9 10 11

                                                 Hub

Blades 1, 2   Tip

          ○   ○   ○   ○   ○
          12   13   14   15   16

          ○   ○
          17   18

Leading   ○
edge   19

          ○   ○
          20   21

          ○   ○   ○   ○   ○
          22   23   24   25   26
                                                 Hub
                                        TE81-7041
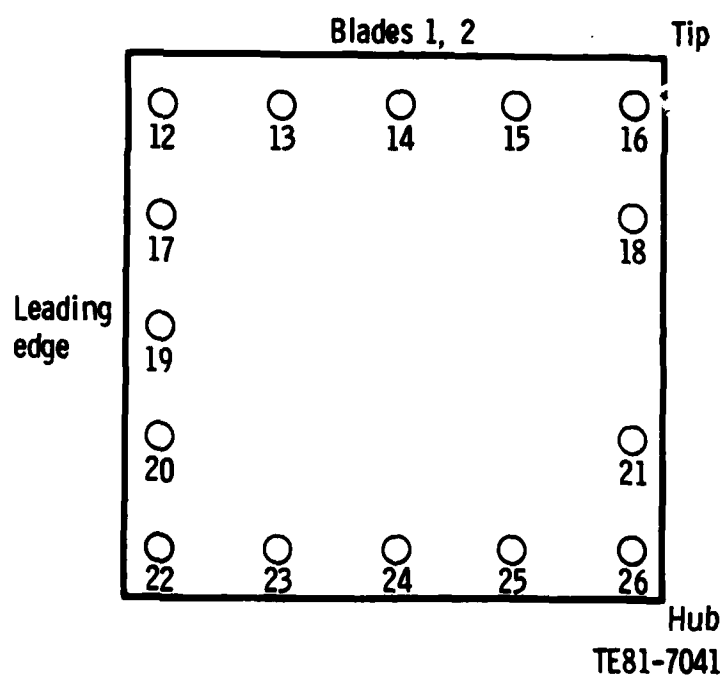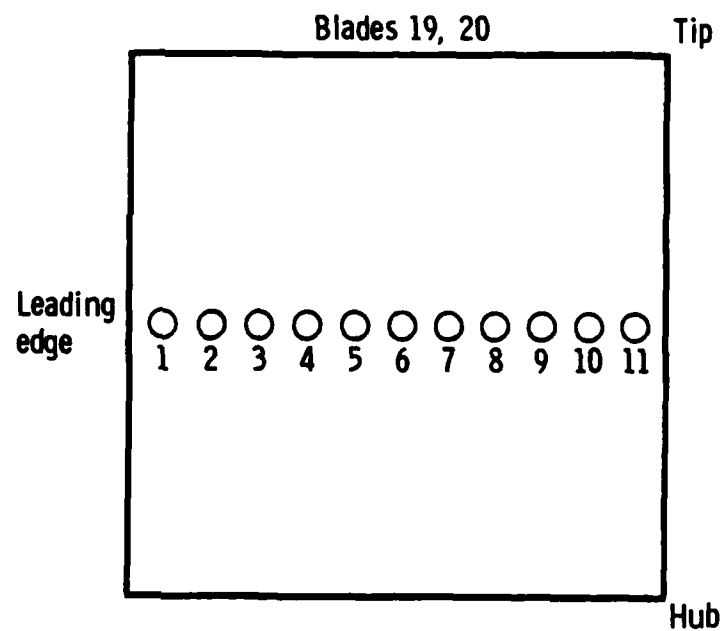
Figure 5.   Location of Kulites on airfoils.

19

Figure 6. View of typical hot wire installation in low-speed compressor vane row.

The intrapassage traverse assembly included four blades located on a machined Plexiglass insert designed for installation in a machined window of the low-speed rig original casing assembly. The assembly is shown in Figure 9. The through holes for the adjoining stators are shown at the left and right edges of the photograph.

Figure 7. View showing hot wire traversing gear on low-speed compressor.
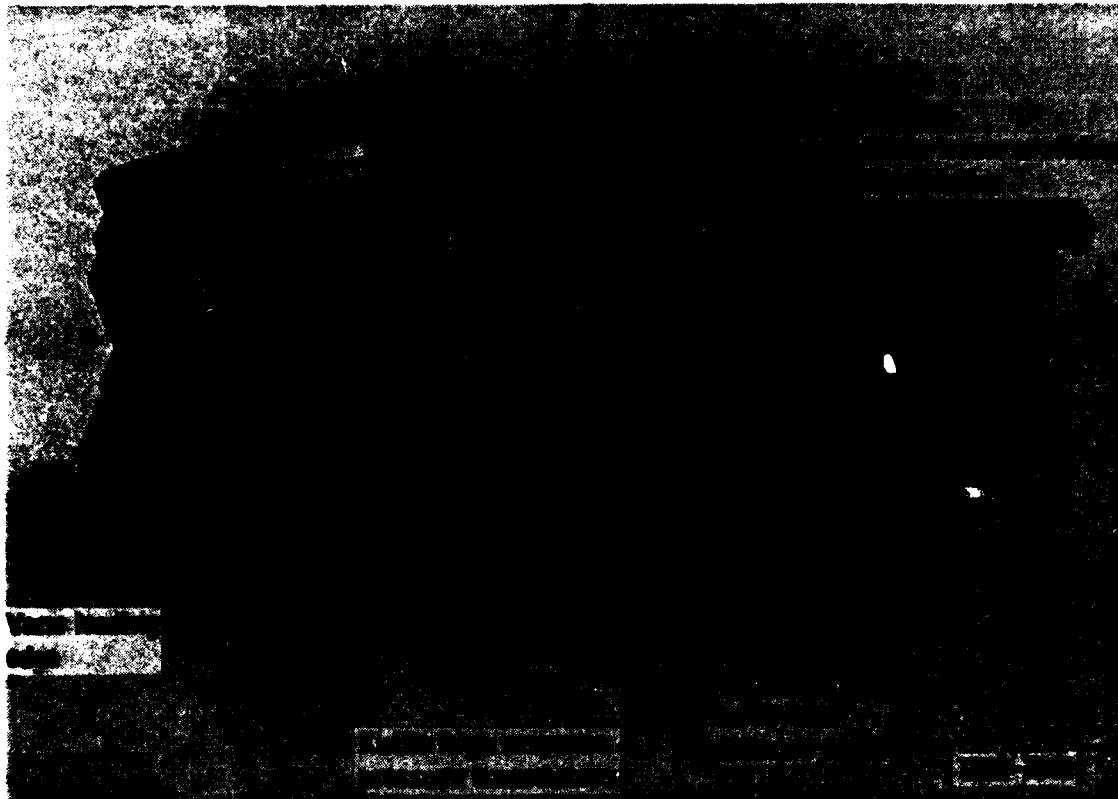
Figure 8. Instrumented four-vane annular cascade assembly.

Vane trailing edge

Adjacent vane trunnion mounting hole

TE81-7045
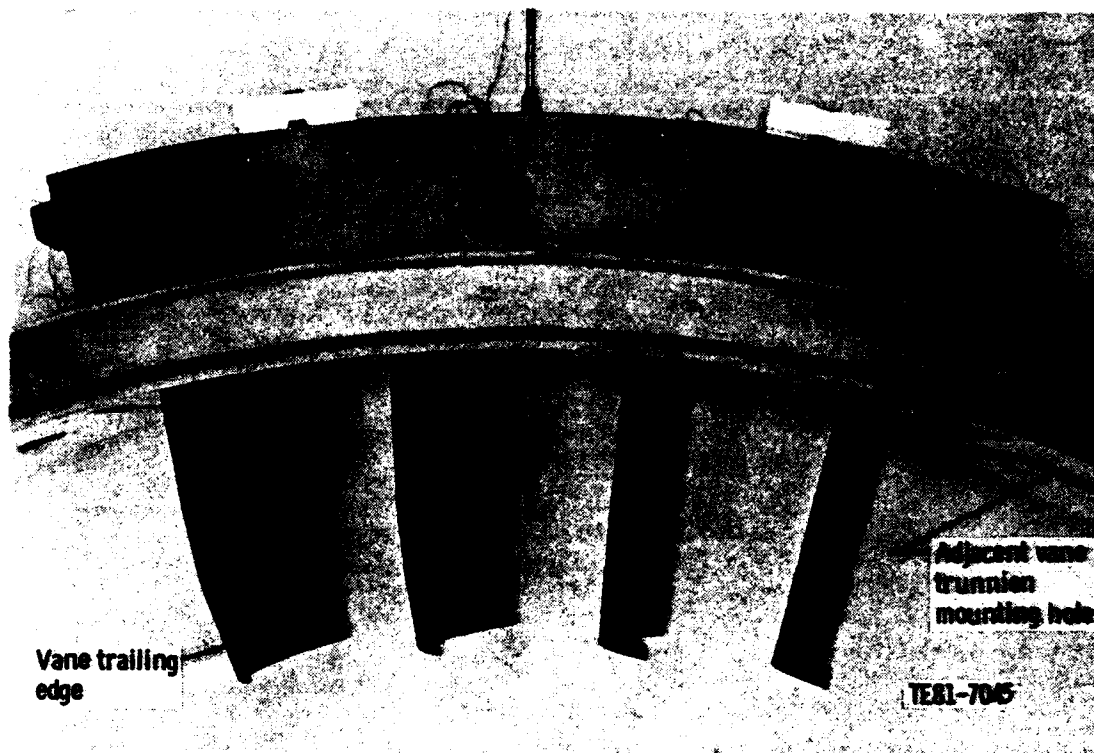
Figure 9. Instrumented four-vane cascade assembly installed in compressor casing.

23

III. DATA ACQUISITION SYSTEM

The central element in the acquisition of the time-variant and steady-state data in this experiment was a digital computer with its specialized peripheral hardware. An HP Model 2117F computer operating under RTEIVB software is used with a Preston GMAD-2 analog-to-digital (A/D) conversion system to acquire data at a rate of 50,000 points per sec for each of the transducers. For data acquisition in the steady-state mode, the computer is interfaced with a Digitec scanner which allows conversion of Scannivalve voltages to appropriate pressures as well as calculation of operating temperatures.

Calibration of the steady-state pressure measuring system is accomplished automatically and on line. A dead weight system provides reference pressures of 0, 0.5, and 1.0 psia to the Scannivalve transducers. When the computer reads these pressures, a linear curve fit is used to establish a calibration curve for each of the six transducers. Then the data channels are interpreted, based on the proper curve. For time-variant pressures, the instrumented stators were placed in a pressure chamber, and five levels of pressure, ranging from 8 psia to slightly above ambient, were used to construct a calibration curve for each of the installed transducers. These curves were read into the computer for transducer voltage conversions to pressure.

Calibration of the crossed-wire probe is obtained via a controlled temperature air jet capable of furnishing velocities over the range of interest. Data at standard temperature (room ambient) are obtained and represent a base-line velocity versus wire output voltage curve. This curve is linearized electronically using built-in features of the anemometry system. Corrections for temperature are made internally in the computer based on the temperature difference from the base-line value.

In the performance of this experimental effort, the data acquisition sequence was divided into three segments: steady-state performance, measurement of pressures, and measurement of wake velocity. The steady-state data acquisition followed the standard format of establishing corrected rotor speed and calculating pressure ratio, mass flow rate, and other compressor performance parameters.

25

Time-variant measurements of the surface pressures and rotor wake passage followed concepts developed in earlier AFOSR-sponsored research. An optical encoder, which delivers a positive, 1.5 microsecond duration voltage spike during each rotor revolution, is used to trigger the Preston A/D converter. Each time the converter is triggered, data points are taken over a time period equal to the passage time of two rotor wakes. These data are stored in the computer in digital form and the A/D trigger is reset by the computer. When the encoder voltage spike is recognized, another sample of data containing an identical number of points as the first sample is acquired and stored. Three hundred of these samples (ensembles) are acquired and stored for each data sequence.

A computer retrieval algorithm is used to read the data from a disk storage location and to arrange the data according to transducer identification. The data ensembles are averaged in a point-to-point manner. Since each ensemble contains an identical number of points, the first point of each ensemble is averaged over the number of ensembles, followed by the second, etc., until all points have been averaged. This ensemble overlay drastically improves the ability to distinguish signals occurring at blade passage frequency.

Tables 3 through 7 present a typical output of the data acquisition system. In this example, calibration of the system was being performed. A 0.5 volt sinusoidal signal was simultaneously fed into the A/D converter terminals. The frequency of this signal was chosen to be 630 Hz to correspond to a rotor speed of 900 rpm. With the 630 Hz frequency and a digitizing rate of 50,000 points per channel per second, two cycles of data require 158 points for each channel. Kulites 37, 38, 39, and 40 were assumed to provide the 0.5 volt signal while operating through amplifier gains of 2400. Three hundred ensembles were acquired, averaged for each of the required 158 points, multipled by appropriate calibration values to obtain psia, and printed in Table 3.

Table 3.

Typical pressure output as function of time for Kulite locations 37, 38, 39, and 40.

Rpm = 900,000

Digitizing rate = 200,000

Points per channel = 158

	Kulite # = 37 AMP = 2400.0 psi	Kulite # = 38 AMP = 2400.0 psi	Kulite # = 39 AMP = 2400.0 psi	Kulite # = 40 AMP = 2400.0 psi
1	0.01126	0.01214	0.01087	0.01297
2	0.01200	0.01301	0.01184	0.01410
3	0.01308	0.01409	0.01257	0.01506
4	0.01416	0.01521	0.01340	0.01587
5	0.01496	0.01629	0.01428	0.01671
6	0.01577	0.01720	0.01499	0.01743
7	0.01623	0.01811	0.01596	0.01824
8	0.01695	0.01880	0.01655	0.01903
9	0.01759	0.01953	0.01725	0.01974
10	0.01812	0.01999	0.01777	0.02023
11	0.01855	0.02044	0.01812	0.02087
12	0.01889	0.02064	0.01850	0.02121
13	0.01909	0.02085	0.01866	0.02162
14	0.01937	0.02087	0.01859	0.02153
15	0.01940	0.02077	0.01828	0.02136
16	0.01937	0.02061	0.01809	0.02097
17	0.01915	0.02031	0.01770	0.02065
18	0.01884	0.02007	0.01731	0.01999
19	0.01839	0.01962	0.01678	0.01927
20	0.01769	0.01904	0.01631	0.01846
21	0.01705	0.01833	0.01575	0.01780
22	0.01625	0.01766	0.01519	0.01698
23	0.01544	0.01675	0.01446	0.01611
24	0.01443	0.01575	0.01377	0.01524

27

Table 3. (Cont)

	Kulite # = 37 AMP = 2400.0 psi	Kulite # = 38 AMP = 2400.0 psi	Kulite # = 39 AMP = 2400.0 psi	Kulite # = 40 AMP = 2400.0 psi
25	0.01352	0.01463	0.01287	0.01438
26	0.01260	0.01350	0.01186	0.01319
27	0.01155	0.01219	0.01079	0.01214
28	0.01049	0.01085	0.00960	0.01088
29	0.00944	0.00962	0.00827	0.00943
30	0.00828	0.00821	0.00703	0.00783
31	0.00689	0.00678	0.00563	0.00629
32	0.00554	0.00538	0.00432	0.00463
33	0.00413	0.00382	0.00284	0.00284
34	0.00261	0.00246	0.00157	0.00109
35	0.00098	0.00078	0.00021	-0.00041
36	-0.00062	-0.00078	-0.00109	-0.00211
37	-0.00209	-0.00238	-0.00237	-0.00356
38	-0.00358	-0.00389	-0.00350	-0.00493
39	-0.00499	-0.00558	-0.00480	-0.00614
40	-0.00620	-0.00696	-0.00595	-0.00753
41	-0.00735	-0.00845	-0.00714	-0.00862
42	-0.00838	-0.00957	-0.00821	-0.00975
43	-0.00931	-0.01070	-0.00930	-0.01090
44	-0.01011	-0.01154	-0.01020	-0.01188
45	-0.01090	-0.01247	-0.01103	-0.01289
46	-0.01171	-0.01312	-0.01176	-0.01381
47	-0.01249	-0.01392	-0.01246	-0.01472
48	-0.01315	-0.01443	-0.01293	-0.01547
49	-0.01385	-0.01508	-0.01330	-0.01594
50	-0.01447	-0.01552	-0.01361	-0.01630
51	-0.01486	-0.01606	-0.01387	-0.01669
52	-0.01524	-0.01640	-0.01397	-0.01669
53	-0.01558	-0.01670	-0.01416	-0.01681
54	-0.01556	-0.01681	-0.01421	-0.01662

Table 3. (Cont)

	Kulite # = 37 AMP = 2400.0 psi	Kulite # = 38 AMP = 2400.0 psi	Kulite # = 39 AMP = 2400.0 psi	Kulite # = 40 AMP = 2400.0 psi
55	-0.01536	-0.01688	-0.01420	-0.01637
56	-0.01503	-0.01655	-0.01405	-0.01619
57	-0.01474	-0.01629	-0.01384	-0.01587
58	-0.01435	-0.01578	-0.01361	-0.01543
59	-0.01388	-0.01523	-0.01314	-0.01500
60	-0.01327	-0.01435	-0.01256	-0.01444
61	-0.01260	-0.01370	-0.01186	-0.01374
62	-0.01195	-0.01268	-0.01108	-0.01295
63	-0.01124	-0.01186	-0.01020	-0.01203
64	-0.01056	-0.01087	-0.00926	-0.01090
65	-0.00963	-0.01003	-0.00827	-0.00982
66	-0.00871	-0.00884	-0.00727	-0.00845
67	-0.00763	-0.00786	-0.00617	-0.00711
68	-0.00641	-0.00657	-0.00506	-0.00561
69	-0.00506	-0.00540	-0.00389	-0.00422
70	-0.00365	-0.00380	-0.00273	-0.00269
71	-0.00218	-0.00233	-0.00148	-0.00124
72	-0.00074	-0.00061	-0.00013	0.00053
73	0.00086	0.00093	0.00109	0.00184
74	0.00245	0.00272	0.00255	0.00331
75	0.00374	0.00437	0.00410	0.00486
76	0.00512	0.00599	0.00548	0.00649
77	0.00655	0.00759	0.00688	0.00792
78	0.00775	0.00908	0.00823	0.00952
79	0.00896	0.01037	0.00949	0.01078
80	0.01013	0.01165	0.01066	0.01227
81	0.01126	0.01262	0.01168	0.01349
82	0.01232	0.01370	0.01257	0.01476
83	0.01340	0.01459	0.01335	0.01572
84	0.01438	0.01564	0.01408	0.01671

Table 3. (Cont)

	Kulite # = 37 AMP = 2400.0 psi	Kulite # = 38 AMP = 2400.0 psi	Kulite # = 39 AMP = 2400.0 psi	Kulite # = 40 AMP = 2400.0 psi
85	0.01543	0.01659	0.01481	0.01739
86	0.01616	0.01744	0.01545	0.01837
87	0.01699	0.01822	0.01605	0.01890
88	0.01771	0.01912	0.01663	0.01952
89	0.01831	0.01992	0.01726	0.01984
90	0.01868	0.02044	0.01777	0.02050
91	0.01897	0.02083	0.01819	0.02080
92	0.01911	0.02105	0.01851	0.02115
93	0.01932	0.02126	0.01867	0.02115
94	0.01920	0.02107	0.01863	0.02134
95	0.01909	0.02083	0.01846	0.02114
96	0.01894	0.02040	0.01819	0.02089
97	0.01868	0.02010	0.01777	0.02042
98	0.01834	0.01951	0.01723	0.01999
99	0.01795	0.01900	0.01652	0.01905
100	0.01738	0.01837	0.01593	0.01839
101	0.01673	0.01770	0.01523	0.01750
102	0.01601	0.01696	0.01452	0.01654
103	0.01522	0.01619	0.01368	0.01541
104	0.01419	0.01528	0.01296	0.01451
105	0.01320	0.01426	0.01214	0.01340
106	0.01200	0.01296	0.01119	0.01231
107	0.01094	0.01182	0.01014	0.01105
108	0.00965	0.01046	0.00909	0.00986
109	0.00842	0.00892	0.00787	0.00853
110	0.00720	0.00732	0.00647	0.00702
111	0.00591	0.00605	0.00505	0.00535
112	0.00452	0.00419	0.00360	0.00390
113	0.00310	0.00270	0.00211	0.00215
114	0.00173	0.00106	0.00058	0.00043

30

Table 3. (Cont)

	Kulite # = 37 AMP = 2400.0 psi	Kulite # = 38 AMP = 2400.0 psi	Kulite # = 39 AMP = 2400.0 psi	Kulite # = 40 AMP = 2400.0 psi
115	0.00015	-0.00035	-0.00070	-0.00124
116	-0.00130	-0.00201	-0.00213	-0.00292
117	-0.00262	-0.00329	-0.00337	-0.00454
118	-0.00415	-0.00478	-0.00451	-0.00595
119	-0.00554	-0.00609	-0.00561	-0.00725
120	-0.00684	-0.00758	-0.00665	-0.00847
121	-0.00800	-0.00877	-0.00771	-0.00962
122	-0.00907	-0.00998	-0.00860	-0.01058
123	-0.01010	-0.01113	-0.00957	-0.01144
124	-0.01094	-0.01223	-0.01040	-0.01235
125	-0.01162	-0.01303	-0.01123	-0.01329
126	-0.01236	-0.01392	-0.01209	-0.01408
127	-0.01299	-0.01456	-0.01275	-0.01477
128	-0.01357	-0.01524	-0.01337	-0.01549
129	-0.01395	-0.01556	-0.01379	-0.01607
130	-0.01441	-0.01588	-0.01405	-0.01654
131	-0.01477	-0.01610	-0.01423	-0.01686
132	-0.01512	-0.01640	-0.01436	-0.01699
133	-0.01532	-0.01644	-0.01434	-0.01699
134	-0.01539	-0.01655	-0.01415	-0.01679
135	-0.01534	-0.01632	-0.01395	-0.01649
136	-0.01508	-0.01627	-0.01373	-0.01609
137	-0.01477	-0.01595	-0.01345	-0.01566
138	-0.01435	-0.01565	-0.01301	-0.01506
139	-0.01373	-0.01495	-0.01265	-0.01440
140	-0.01301	-0.01430	-0.01207	-0.01380
141	-0.01227	-0.01342	-0.01142	-0.01285
142	-0.01148	-0.01256	-0.01071	-0.01214
143	-0.01061	-0.01147	-0.00998	-0.01125
144	-0.00974	-0.01044	-0.00894	-0.01033

31

Table 3. (Cont)

	Kulite # = 37 AMP = 2400.0 psi	Kulite # = 38 AMP = 2400.0 psi	Kulite # = 39 AMP = 2400.0 psi	Kulite # = 40 AMP = 2400.0 psi
145	-0.00883	-0.00923	-0.00790	-0.00917
146	-0.00787	-0.00813	-0.00685	-0.00796
147	-0.00674	-0.00676	-0.00563	-0.00657
148	-0.00566	-0.00551	-0.00433	-0.00519
149	-0.00442	-0.00419	-0.00305	-0.00348
150	-0.00307	-0.00281	-0.00182	-0.00198
151	-0.00163	-0.00134	-0.00034	-0.00021
152	-0.00007	0.00017	0.00084	0.00145
153	0.00156	0.00181	0.00217	0.00303
154	0.00310	0.00344	0.00346	0.00452
155	0.00463	0.00504	0.00482	0.00617
156	0.00608	0.00670	0.00617	0.00751
157	0.00749	0.00826	0.00746	0.00896
158	0.00884	0.00983	0.00866	0.01013

Table 4.

Typical Kulite no. 37 Fourier analysis.

Channel # = 26

Harmonic analysis of input Y (I)

Average value = 0.19730795E-02

Harm.	Cosine coefficient	Sine coefficient	Resultant	Phase angle	Relative amplitude
1	-0.9639202E-04	-0.1092428E-03	0.1456894E-03	41.42	0.00834171
2	0.8021245E-02	0.1551424E-01	0.1746516E-01	27.34	1.00000000
3	0.7796816E-04	0.1876813E-03	0.2032321E-03	22.56	0.01163643
4	0.3683029E-04	0.9909060E-04	0.1057138E-03	20.39	0.00605284
5	0.3437311E-04	0.7537189E-04	0.8283980E-04	24.51	0.00474314

Table 4. (Cont)

Harm.	Cosine coefficient	Sine coefficient	Resultant	Phase angle	Relative amplitude
6	0.2569716E-03	0.8274101E-04	0.2699639E-03	72.15	0.01545728
7	0.4823232E-04	0.4879393E-04	0.6860908E-04	44.67	0.00392834
8	0.1637491E-04	-0.9112606E-06	0.1640025E-04	-86.81	0.00093903
9	0.4517150E-04	0.3997350E-04	0.6031870E-04	48.49	0.00345366
10	0.1560322E-03	-0.7864537E-04	0.1747316E-03	-63.25	0.01000458
11	0.1728783E-03	0.7371955E-04	0.1879401E-03	66.90	0.01076085
12	-0.7735053E-04	-0.7938976E-05	0.7775688E-04	84.14	0.00445211
13	-0.1509521E-04	0.7031967E-05	0.1665274E-04	-65.02	0.00095348
14	0.7482457E-05	0.1082528E-04	0.1315956E-04	34.65	0.00075347
15	-0.3741960E-05	0.1989269E-04	0.2024158E-04	-10.65	0.00115897
16	0.3856712E-05	0.2192582E-04	0.2226243E-04	9.98	0.00127468
17	0.8645267E-05	0.1388173E-04	0.1635369E-04	31.91	0.00093636
18	0.5393513E-05	0.2109157E-04	0.2177026E-04	14.34	0.00124650
19	0.1056238E-05	0.1823790E-04	0.1826847E-04	3.31	0.00104599
20	0.8925512E-05	0.1620493E-04	0.1850039E-04	28.85	0.00105927

Table 5.

Typical Kulite no. 38 Fourier analysis.

Channel # = 27

Harmonic analysis of input Y (I)

Average value = 0.20862771E-02

Harm.	Cosine coefficient	Sine coefficient	Resultant	Phase angle	Relative amplitude
1	-0.1293006E-03	-0.1144276E-03	0.1726625E-03	48.49	0.00910661
2	0.9019682E-02	0.1667728E-01	0.1896012E-01	28.41	1.00000000
3	0.7667948E-04	0.2055122E-03	0.2193514E-03	20.46	0.01156909
4	0.2308642E-04	0.1006117E-03	0.1032264E-03	12.92	0.00544440
5	0.1424126E-04	0.9083889E-04	0.9194844E-04	8.91	0.00484957

Table 5. (Cont)

Harm.	Cosine coefficient	Sine coefficient	Resultant	Phase angle	Relative amplitude
6	0.2531388E-03	0.8527836E-04	0.2671173E-03	71.38	0.01408838
7	0.1706447E-04	0.5874671E-04	0.6117494E-04	16.20	0.00322651
8	-0.1521644E-04	0.1547706E-04	0.2170437E-04	-44.51	0.00114474
9	0.2050749E-05	0.7386976E-04	0.7389822E-04	1.59	0.00389756
10	0.1086379E-03	-0.5995191E-04	0.1240824E-03	-61.11	0.00654439
11	-0.2364173E-04	0.1845427E-03	0.1860509E-03	-7.30	0.00981275
12	0.4739380E-04	-0.1030991E-03	0.1134707E-03	-24.69	0.00598470
13	0.2996072E-04	-0.3113945E-04	0.4321239E-04	-43.89	0.00227912
14	0.3246416E-04	-0.3163402E-05	0.3261792E-04	-84.43	0.00172034
15	0.3758700E-05	0.6140023E-05	0.7199146E-05	31.47	0.00037970
16	0.1766162E-04	0.9898351E-05	0.2024624E-04	60.73	0.00106783
17	0.1344712E-04	0.8110497E-06	0.1347156E-04	86.55	0.00071052
18	0.1840911E-04	0.7830115E-05	0.2000515E-04	66.96	0.00105512
19	0.7561938E-05	0.8803736E-05	0.1160555E-04	40.66	0.00061210
20	0.1194672E-04	-0.3562355E-06	0.1195203E-04	-88.29	0.00063038
21	0.6727308E-05	0.5802281E-05	0.8883870E-05	49.22	0.00046856

Table 6.

Typical Kulite no. 39 Fourier analysis.

Channel # = 28

Harmonic analysis of input Y (I)

Average value = 0.19385300E-02

Harm.	Cosine coefficient	Sine coefficient	Resultant	Phase angle	Relative amplitude
1	-0.1205791E-03	-0.9595168E-04	0.1540975E-03	51.49	0.00933124
2	0.8135976E-02	0.1437091E-01	0.1651416E-01	29.52	1.00000000
3	0.5919118E-04	0.1773111E-03	0.1869300E-03	18.46	0.01131938
4	0.8120473E-05	0.9184305E-04	0.9220134E-04	5.05	0.00558317

Table 6. (Cont)

Harm.	Cosine coefficient	Sine coefficient	Resultant	Phase angle	Relative amplitude
5	-0.8393691E-08	0.7265508E-04	0.7265508E-04	-0.01	0.00439956
6	0.2103726E-03	0.5265912E-04	0.2168631E-03	75.95	0.01313195
7	0.9549003E-06	0.5396007E-04	0.5396851E-04	1.01	0.00326802
8	-0.3134662E-04	-0.3493235E-05	0.3154066E-04	83.64	0.00190992
9	-0.2562669E-04	0.3553059E-04	0.4380811E-04	-35.80	0.00265276
10	0.3710931E-04	-0.9319960E-04	0.1003158E-03	-21.71	0.00607454
11	-0.1404478E-03	-0.3004428E-05	0.1404799E-03	88.77	0.00850664
12	0.1403272E-03	0.2797883E-04	0.1430893E-03	78.72	0.00866465
13	0.5221152E-04	0.2396382E-04	0.5744831E-04	65.35	0.00347873
14	0.3766549E-04	0.1892079E-04	0.4215074E-04	63.33	0.00255240
15	0.2341600E-04	0.1874873E-04	0.2999706E-04	51.32	0.00181645
16	0.2641311E-04	0.2529622E-04	0.3657254E-04	46.24	0.00221462
17	0.1453141E-04	0.1952270E-04	0.2433717E-04	36.66	0.00147372
18	0.1840494E-04	0.1660506E-04	0.2478850E-04	47.94	0.00150105
19	0.1756033E-04	0.1122073E-04	0.2083915E-04	57.42	0.00126190
20	0.1219488E-04	0.6213328E-05	0.1368651E-04	63.00	0.00082877
21	0.1604987E-04	0.1263846E-04	0.2042863E-04	51.78	0.00123704
22	0.1272368E-04	0.1118198E-04	0.1693898E-04	48.69	0.00102572

Table 7.

Typical Kulite no. 40 Fourier Analysis.

Channel # = 29

Harmonic analysis of input Y (I)

Average value = 0.21026526E-02

Harm.	Cosine coefficient	Sine coefficient	Resultant	Phase angle	Relative amplitude
1	-0.1304587E-03	-0.1128429E-03	0.1724906E-03	49.14	0.00900186
2	0.9775981E-02	0.1648027E-01	0.1916166E-01	30.68	1.00000000

Table 7. (Cont)

Harm.	Cosine coefficient	Sine coefficient	Resultant	Phase angle	Relative amplitude
3	0.7946166E−04	0.1988299E−03	0.2141202E−03	21.78	0.01117441
4	0.2173061E−04	0.1054438E−03	0.1076597E−03	11.64	0.00561850
5	0.2016155E−04	0.7838842E−04	0.8093969E−04	14.42	0.00422404
6	0.2553129E−03	0.3473440E−04	0.2576648E−03	82.25	0.01344690
7	0.2386855E−04	0.4583988E−04	0.5168174E−04	27.51	0.00269714
8	−0.2427371E−04	−0.1569675E−04	0.2890676E−04	57.11	0.00150857
9	0.8210587E−05	0.1722826E−04	0.1908472E−04	25.48	0.00099598
10	0.6690276E−04	−0.1595070E−03	0.1729696E−03	−22.75	0.00902686
11	0.8379804E−05	−0.1394109E−03	0.1396626E−03	−3.44	0.00728865
12	0.5474903E−04	0.1459044E−03	0.1558383E−03	20.57	0.00813282
13	0.1481133E−04	0.6490719E−04	0.6657567E−04	12.85	0.00347442
14	0.2514684E−04	0.4984393E−04	0.5582814E−04	26.77	0.00291353
15	0.1551244E−04	0.4259447E−04	0.4533128E−04	20.01	0.00236573
16	0.9097535E−05	0.4584973E−04	0.4674360E−04	11.22	0.00243943
17	0.1242233E−04	0.4017877E−04	0.4205530E−04	17.18	0.00219476
18	0.1859396E−04	0.3455231E−04	0.3923771E−04	28.29	0.00204772
19	0.1374333E−04	0.2791245E−04	0.3111244E−04	26.21	0.00162368
20	0.1254515E−04	0.2270344E−04	0.2593891E−04	28.92	0.00135369
21	0.1338141E−04	0.2484901E−04	0.2822296E−04	28.30	0.00147289
22	0.1273964E−04	0.1684588E−04	0.2112066E−04	37.10	0.00110224
23	0.4982788E−05	0.2470840E−04	0.2520582E−04	11.40	0.00131543

Fourier analyses of each of the four signals were performed and are presented
in Tables 4, 5, 6, and 7 for the respective Kulite channels. Note the predom-
inant second harmonic, which represents a 630 Hz signal. Using the assumed
amplifier gains and the correct calibration values for each of the Kulites,
the Fourier analyses all indicate 0.497 volts as the input voltage, an excel-
lent reproduction of the 0.5 volt read-in signal. For the second harmonic
(630 Hz), the phase angles for Kulites 37 (channel 26) through 40 (channel 29)
are 27.34, 28.41, 29.52, and 30.68 deg, referenced to the encoder pulse. The
change in phase between channels averages 1.113 deg. Based on the slew rate

of the A/D converter, this value should be 1.134 deg. Again, excellent agreement is shown in this calibration step, which has been used to illustrate a typical handling of Kulite data.

For the crossed-wire probe, velocity calibration is performed for varying temperatures. A standard velocity versus voltage curve is linearized using the anemometry system. The effects of temperature are calculated using the calibration data furnished to the computer. Figure 10 illustrates the physical elements of the data acquisition system. Each of the dynamic pressure transducers are hard-wired into a patch panel. Selection of any four can be made using a four-element plug. This plug is hard-wired into the inputs to four dynamic amplifiers. The outputs from each of these amplifiers goes to three connections: the A/D converter, a small signal monitor oscilloscope, and a switchbox from which the signal can be displayed on a dual-beam storage oscilloscope. Therefore, the signal can be viewed, interpreted, and photographed, if desired, as it is being digitized. Hot-wire signals from each of the crossed wires are treated in a similar manner, although they pass through DISA anemometry conditioners, rather than through the dynamic amplifiers.
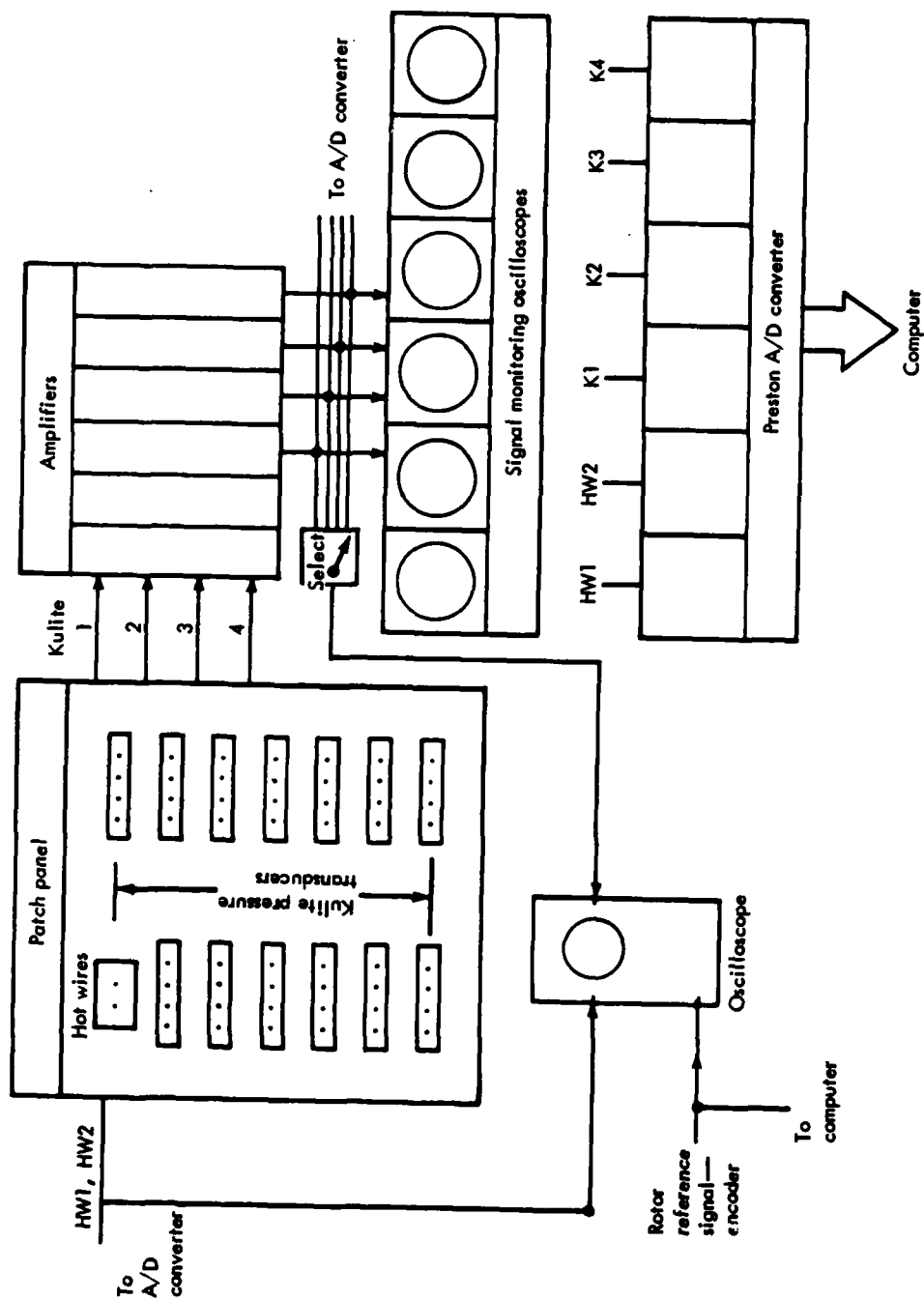
Figure 10. Program data acquisition system.

TE81-7046

38

IV. EXPERIMENTAL PROGRAM

The experimental effort for this program consisted of three phases: (1) steady-state performance evaluation, (2) stator vane surface three-dimensional dynamic pressure measurement, and (3) radial-circumferential hot wire anemometer wake measurements upstream, downstream, and inside the vane passage. The experimental work performed during each of these phases will be discussed in separate sections.

STEADY-STATE PERFORMANCE EVALUATION

The overall steady performance of the DDA low-speed compressor configured for the present investigation is presented in Figure 11. This build (BU18) featured a 3% blade height tip clearance and a nonrotating hub wall under the vane hubs. The clearance between the vane hubs and the endwall was essentially zero.

Several steady-state operating points were selected at which to evaluate the stator surface Kulite dynamic pressure and hot wire anemometry signals. At design speed, four points (data points 1, 2, 3, and 4) were selected so that the vane mean-line section Kulite results could be compared directly with mean-line data that had been obtained during earlier (1977) investigations. Data point (DP) 1 represents a lightly loaded open throttle condition; DP 3 represents the design point operating condition; DP 4 is the most heavily loaded point before stall; and DP 2 fills in between design and the open throttle conditions. In addition to these four points, four other points were investigated at the maximum (125% $N/\sqrt{\theta}$) operating speed. It was of interest to determine whether the increased signal strength of the Kulite gauges and the hot wire obtained at the higher speed would be useful in assessing the details of passage flow field. It was found, however, that the 100% design speed results were completely adequate as far as instrument signal strength was concerned.

39
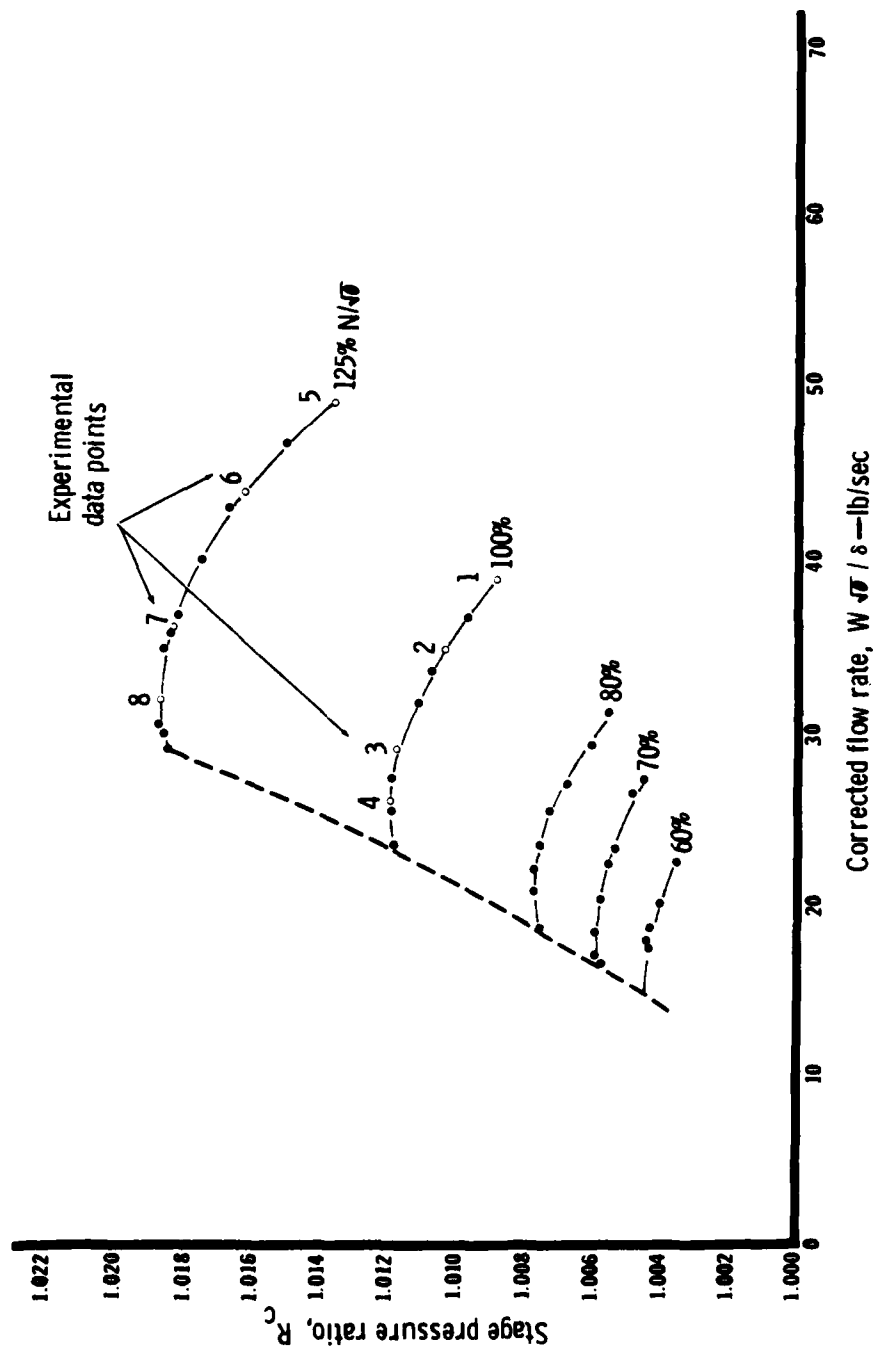
Figure 11. Single-stage low speed compressor (BU18) performance map.

TE81-7047

40

At each of the eight data points shown on Figure 11, the following measurements were made:

o Steady-state pressurse and temperatures throughout the stage

o Dynamic pressure measurements from 52 Kulite gauges on the airfoil surface at hub, mean, and tip sections along the axial span

o Hot wire anemometry wake measurements at various radial-circumferential locations at four axial stations

     o Stator inlet—approximately 10% axial chord upstream of stator

     o Inside stator passage—approximately 13% axial chord

     o Inside stator passage—approximately 73% axial chord

     o Stator exit—approximately 112% axial chord downstream of stator

The following sections deal with the dynamic experimental measurements that were made as the compressor was operating at various steady-state conditions and how those measurements were interpreted.

DYNAMIC PRESSURES INDUCED ON STATOR SURFACES

Experimental Results

In this subsection, a detailed discussion of the pressures measured on the stator surface will be presented. Observations based on these data will be presented for consideration.

Before a discussion of the surface pressures is presented, factors or parameters that have an influence on these pressures must be presented. In Figure 12, the measured air inlet angles at the Kulite locations are presented, along with the stator inlet metal angle. The absolute inlet angle as measured in the static frame increases with increased compressor loading. At the wide-open throttle point (DP 1, Figure 11), the incidence angle at each radial station is negative. At DP 4, the most highly loaded point, the incidence angle over most of the stator are positive. At the endwalls, high positive incidence angles are noted. At intermediate loading, DP 2 and DP 3, the incidence angles alternate between positive at the endwalls and negative in the center span region.

41
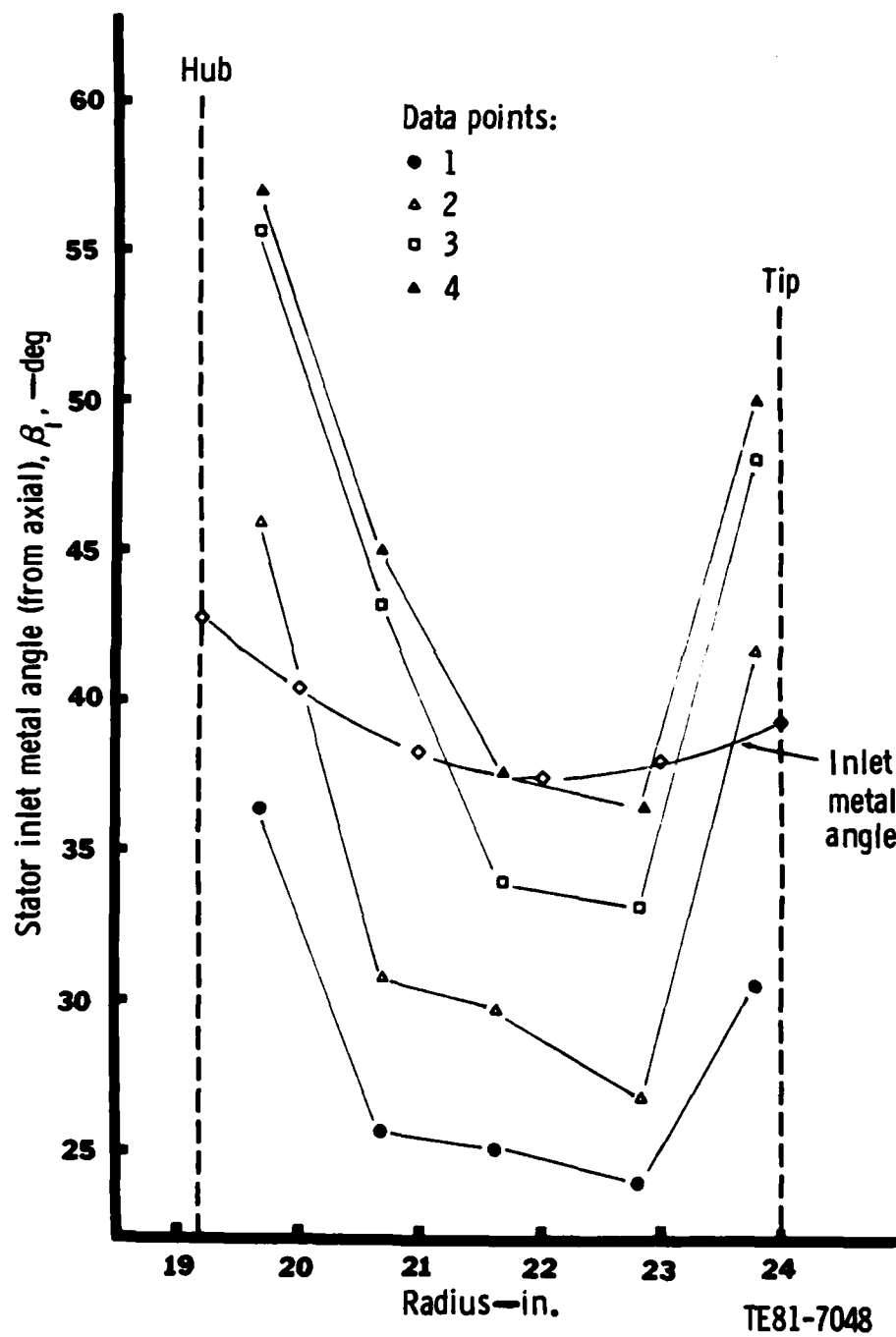
Figure 12. Midpassage stator inlet air angle.

TE81-7048

42

In Figure 13, the time-variant velocity component perpendicular to the flow
direction has been normalized by dividing by the inlet absolute velocity.
This normalized perturbation velocity has been presented versus the percentage
of passage height measured from the outer diameter. With increased compressor
loading, this perturbation quantity, as measured circumferentially midway be-
tween stator leading edges, increases. Note the rapid increase with loading
from DP 2 to DP 3 and DP 4. Another interesting occurrence is the large in-
crease noted between DP 2 and DP 3 at the 70% station, which is near the hub.
The overall trend of the curves indicates that the minimum normalized pertur-
bation velocity is moving from center span to the larger diameters with in-
creased loading. As will be discussed in Section V, the low-pressure ratio
points, DP 1 and DP 2, have classical viscous wakes in the center span region,
25% to 70% span, while the near endwall points are strongly affected by sec-
ondary and end clearance flows. When loading increases, the classical viscous
wake region diminishes as secondary effects in the hub region affect a larger
region on the stator surface.

In defining phase angles for the various parameters measured, a fixed point on
the rotor shaft was used to indicate zero phase angle. All quantities were
then phased relative to the discrete pulse. Therefore, the phase angles were
not referenced to a quantity measured, but rather to a fixed, but arbitrary,
reference time base. Phase comparisons, chordwise and spanwise, for any vari-
able can be made, but correlation with analytical results must be performed by
removing the arbitrary reference time base by assuming that some particular
phase angle being compared yields identical results. This has been done in
this discussion for the analytical comparisons.

Phase angles associated with the normalized velocity perturbation are pre-
sented at the five radial Kulite positions in Figure 14. The data indicate an
overall trend for all loadings. A weak trend of decreasing phase angle with
increased loading is noted. Primarily, the data suggest a sudden shift in
phase between the unloaded points 1 and 2 and the loaded points 3 and 4. This
shift is consistent with the increased normalized perturbation velocity noted
in Figure 13.

43

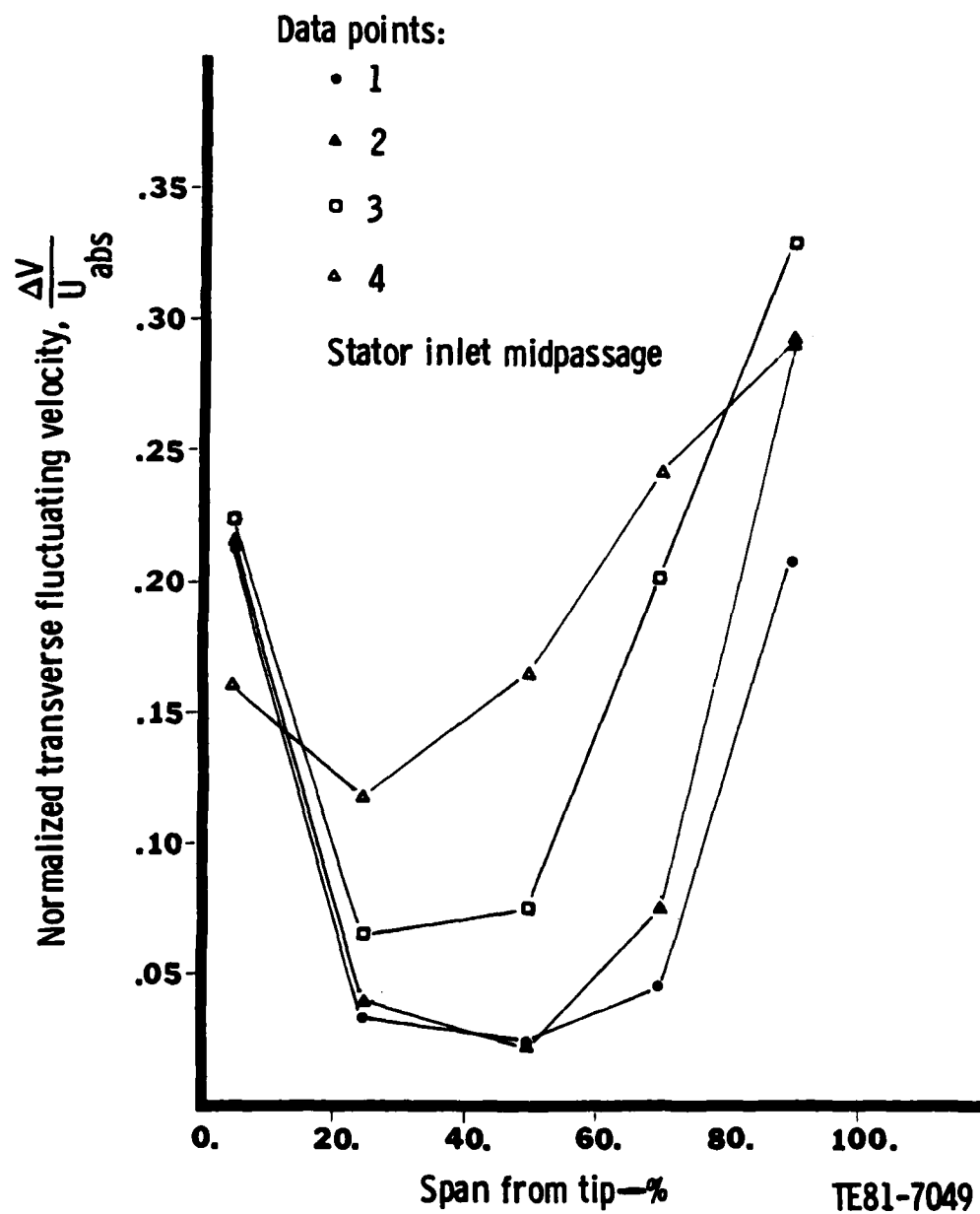Figure 13. Radial distribution of normalized transverse fluctuating velocity in the vane inlet midpassage.

44
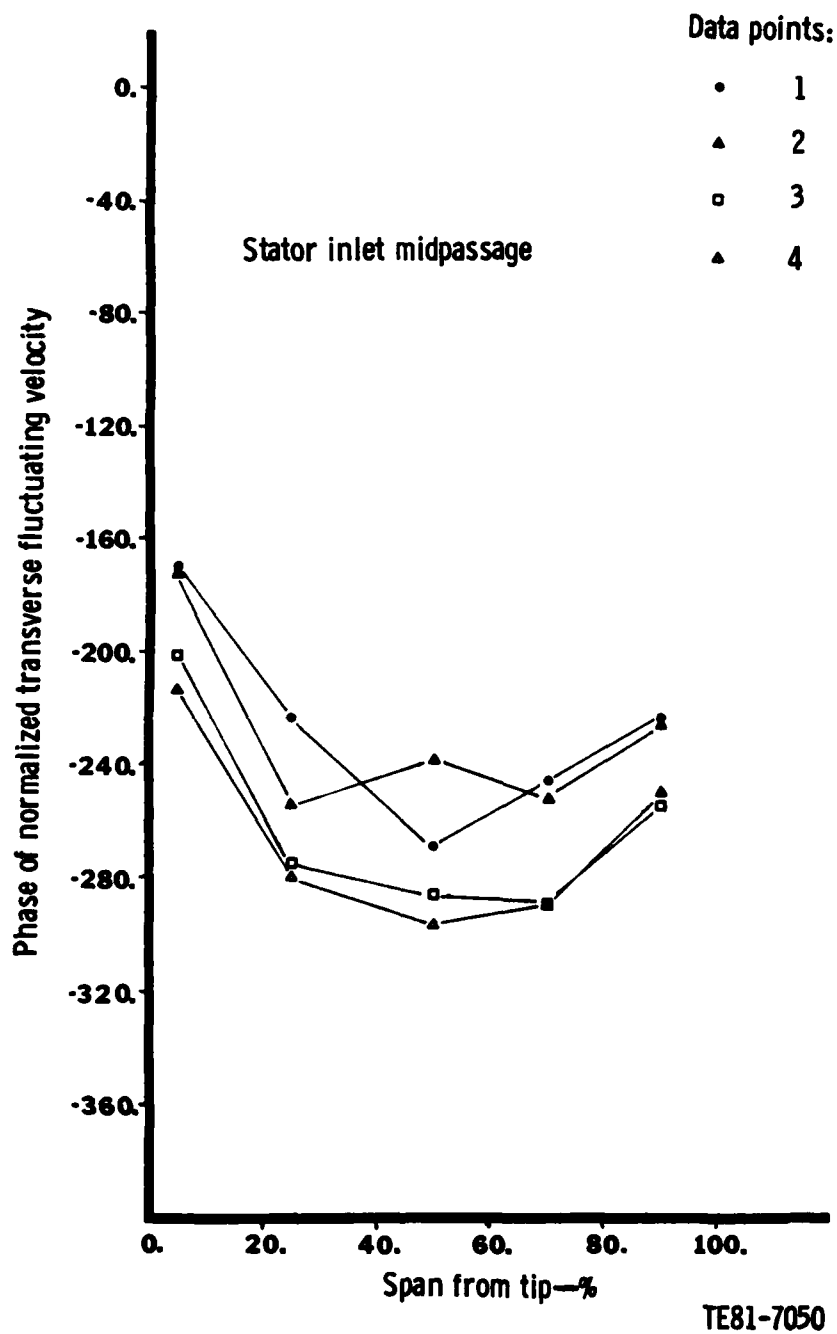
Figure 14. Radial distribution of transverse fluctuating velocity component phase angle in the vane inlet midpassage.

TE81-7050

45

The surface pressures, as measured by the 10 Kulites located on the leading edge of the stator vanes, were used to calculate the magnitude and phase of the time-variant pressure difference across the stator. Figure 15 presents the magnitude of these pressures.

The qualitative trend in Figure 15 indicates higher fluctuating pressures at the endwalls than near the center span of the airfoil. This qualitative trend was also suggested by the perturbation velocities presented in Figure 13. However, the quantitative trend at any particular measuring station does not follow a consistent trend with respect to loading.

In Figure 16 the data presented in Figure 15 have been normalized by dividing by the product of twice the dynamic head and the normalized perturbation velo- city. Examination of this figure is aided by referring also to Figure 12. Consider the five radial measurement stations and note that at each station the minimal normalized pressure difference corresponds to the minimum inci- dence angle. The trend at all stations is for larger positive or negative incidence angles to result in increasing normalized pressure difference.

This influence of incidence angle is seen more clearly in Figure 17. The data from each leading edge Kulite have been plotted versus incidence angle. At each radial location an individual curve is needed to portray the correct trend. Taken as a group, the five curves indicate conclusively that minimum normalized pressure difference at the leading edge occurs at near-zero inci- dence conditions.

The phase angle of the normalized pressure difference at the leading edge of the stator is presented in Figure 18. The banding of the data is similar to the grouping noted in Figure 14, in which the phase of the normalized velocity was presented versus radial location. To establish the correlation between the phasing of the pressures and the incoming velocity perturbations, the phase angle of the normalized velocity perturbation was subtracted from the corresponding phase angles of the pressure differences at the leading edge. This normalized phase is presented in Figure 19. The data in this plot do not collapse into a single constant value as would be expected if phenomenal events at each leading edge location were the same. A slight trend of in-

46

Data points:

● 1

▲ 2

□ 3

▲ 4

.16

Stator leading edge
locations

.14

Pressure difference across airfoil, ΔP_s —psia

.12

.10

.08

.06

.04

.02

0.0

0.   20.   40.   60.   80.   100.

Span from outer diameter—%
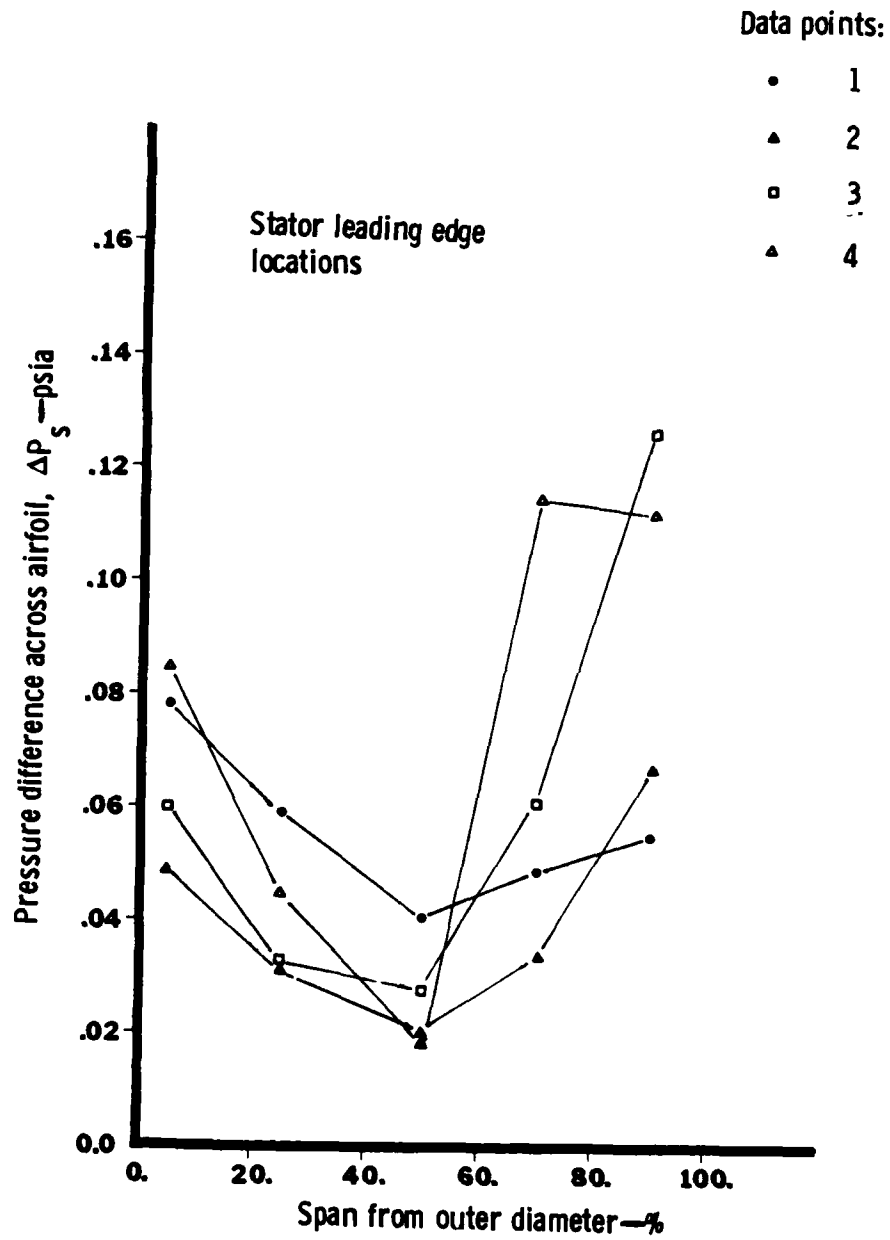
TE81-7051

Figure 15.   Radial variation of time-dependent static pressure across vane
leading edge.
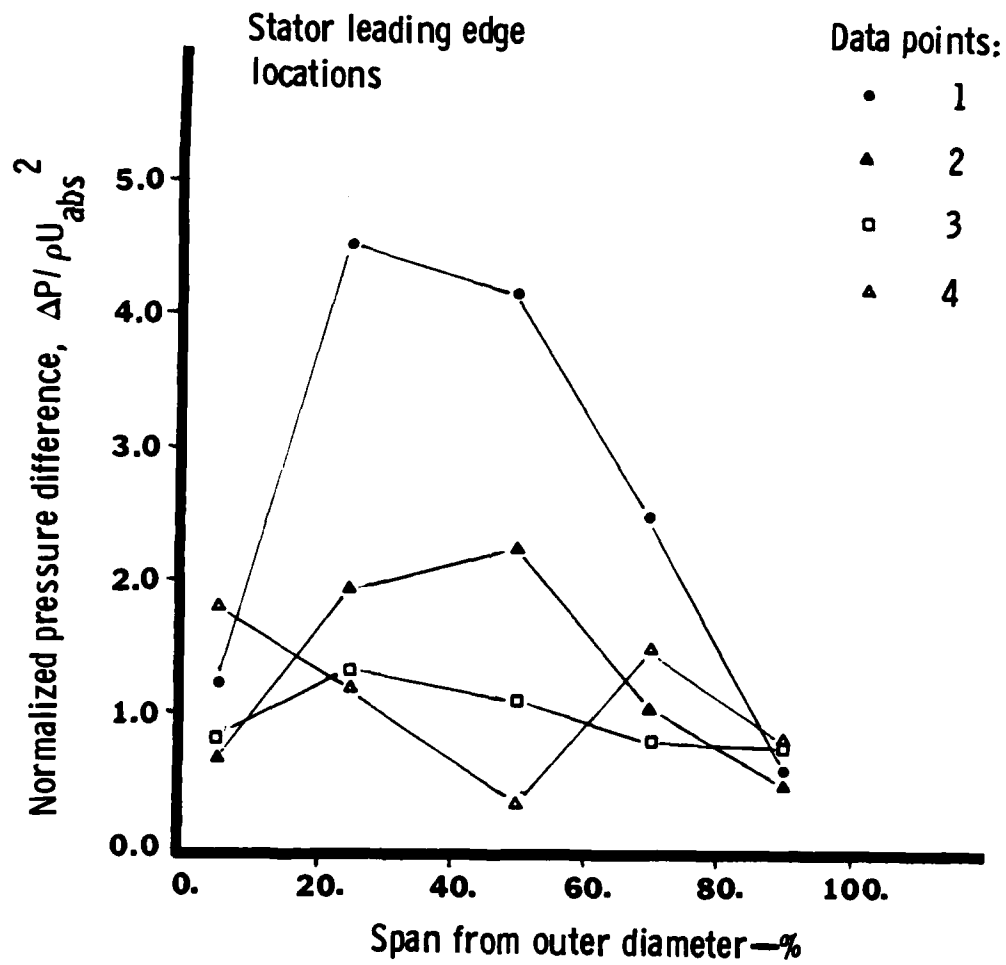
Figure 16. Radial variation of normalized time-dependent static pressure across vane leading edge.
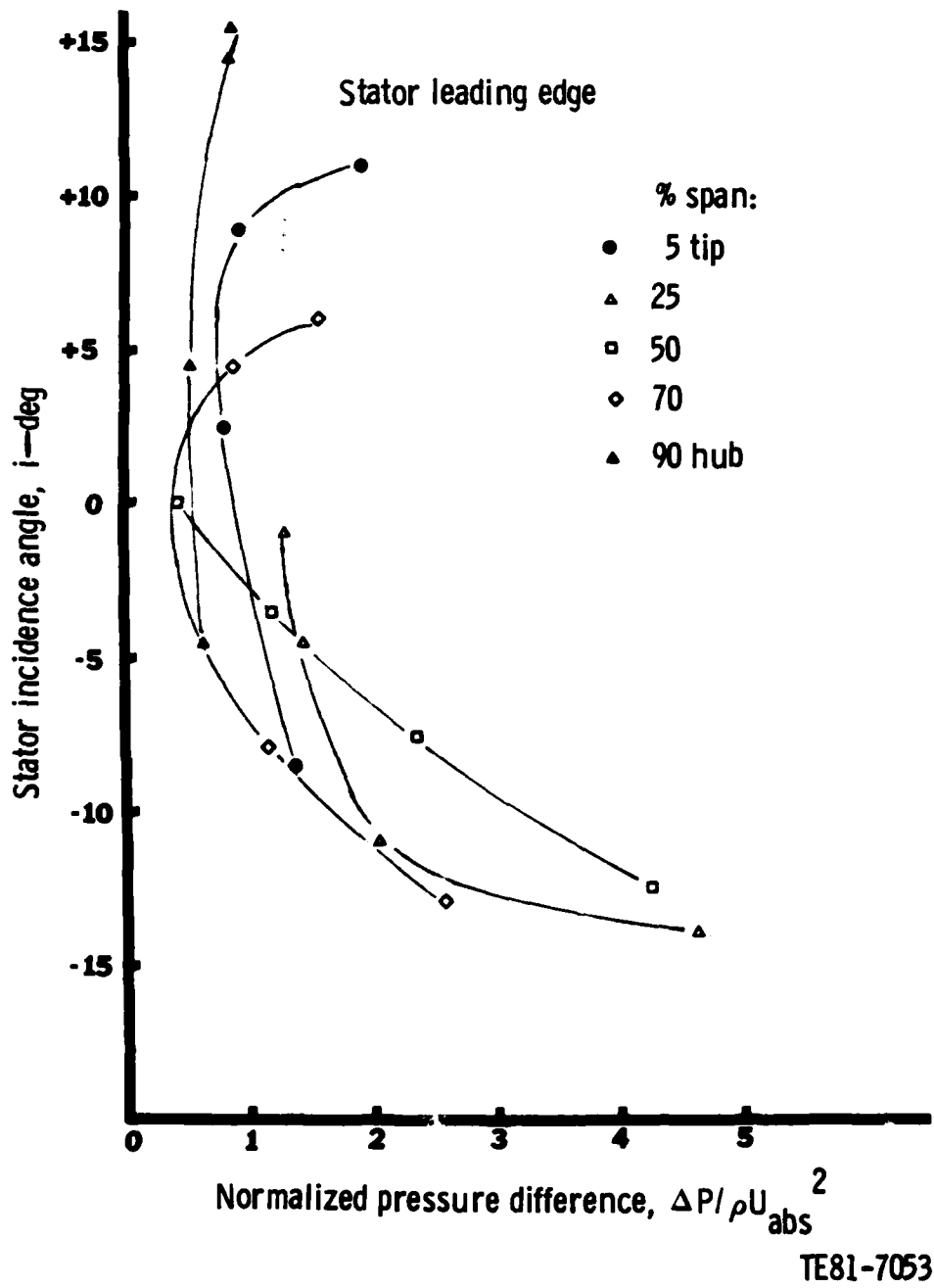
Figure 17. Correlation of vane leading edge normalized pressure difference to stator incidence angle.

49
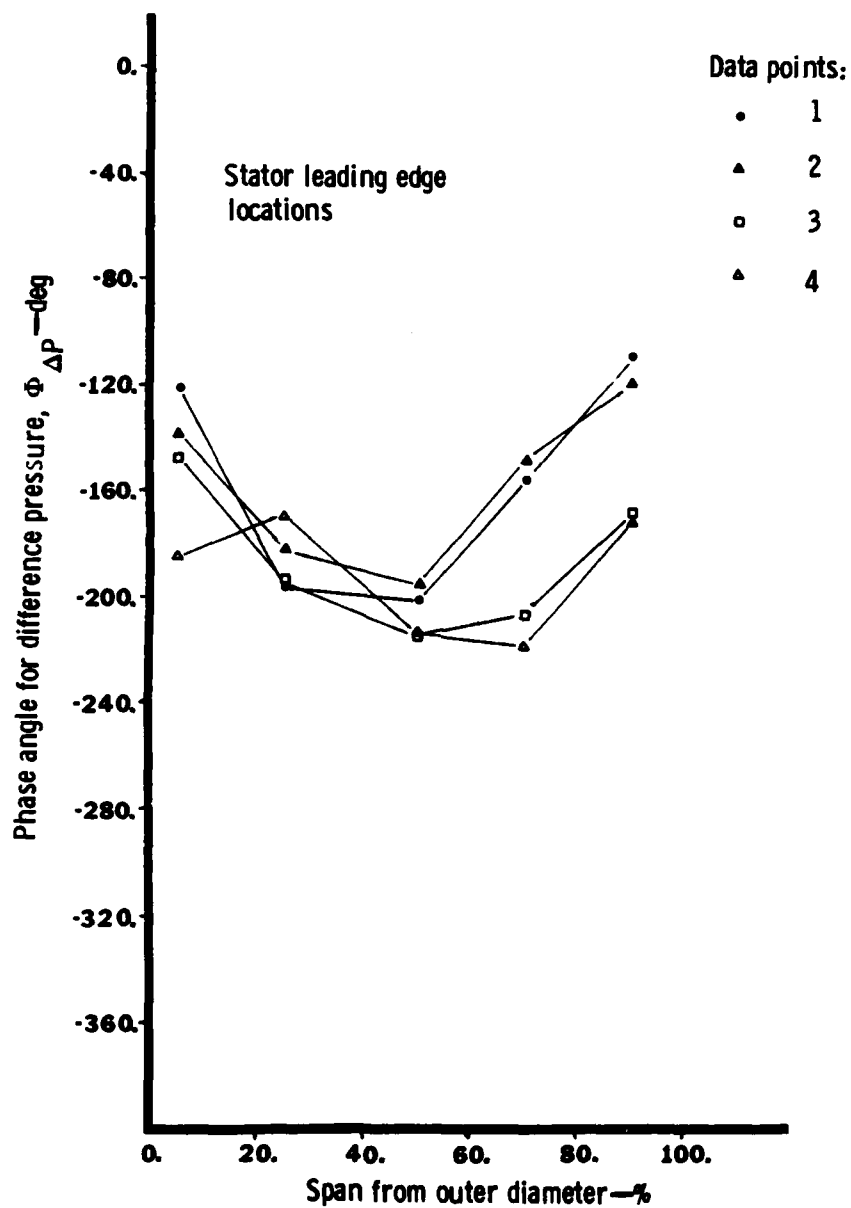
Figure 18. Radial distribution of the pressure difference phase angle at the stator leading edge.

TE81-7054

50
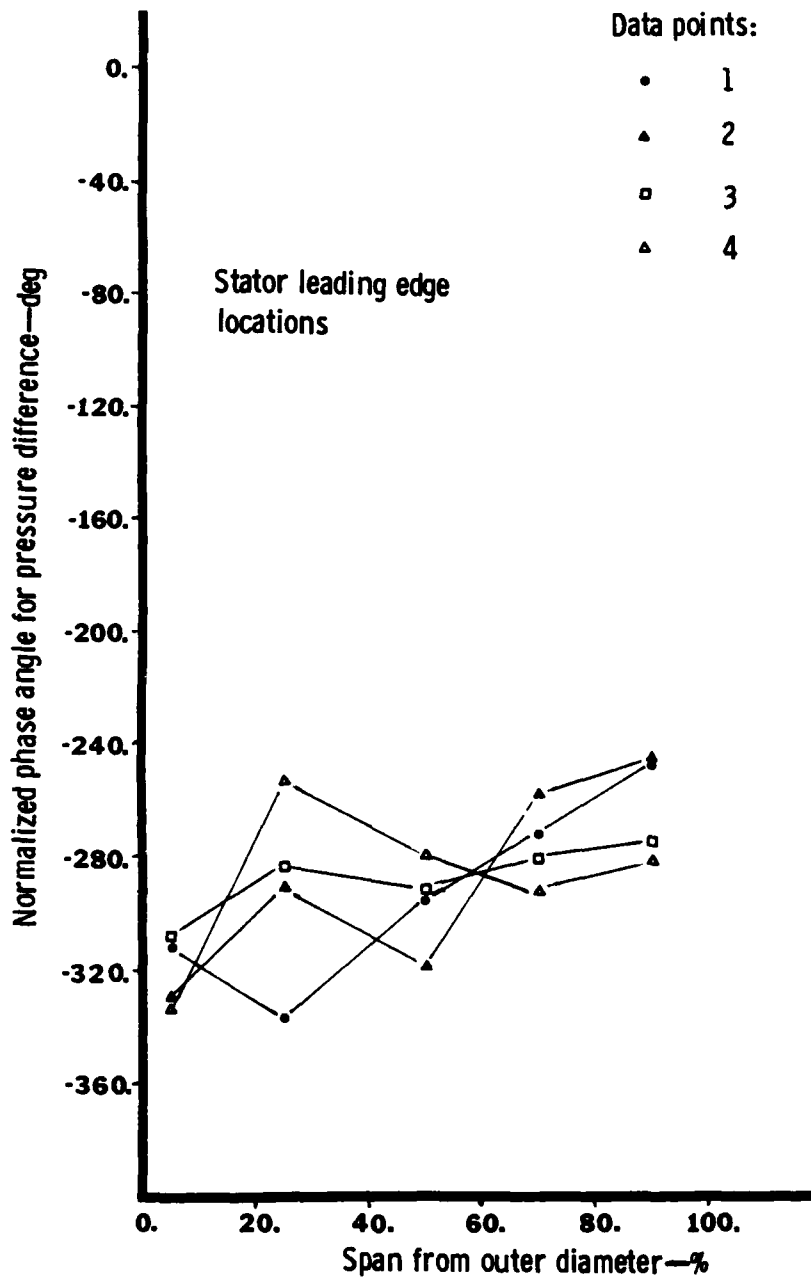
Figure 19. Radial variation of vane leading edge normalized phase angles.

51

creasing phase angle from tip to hub of the stator is noted but is not understood. Normalization by the transverse perturbation velocity phase angle groups the data somewhat closer, but not sufficiently close to present a definitive conclusion.

On each surface of the stator airfoil, behavioral trends of the dynamic pressure quantities vary somewhat. In Figures 20 and 21 are presented the fluctuating surface pressure magnitudes for the suction and pressure surfaces, respectively. The data included in Figure 20 indicate that the minimal pressures occur on the suction surface with negative or near-zero incidence angles. This is true at all stations except the tip section, where the unloaded point, DP 1, is the largest fluctuating pressure. For the pressure surface, Figure 21, the highest pressure loading is noted at the largest negative incidence angles for the three intermediate span locations. For the other operating points, the data are closely grouped.

The leading edge surface pressure data were normalized using the normalization parameter discussed previously. The resulting suction- and pressure-surface normalized pressures are presented versus operating incidence angles in Figure 22.

From this figure, an indication of the phenomena creating the fluctuating pressures can be seen. Trend lines are drawn on the normalized pressure data for each surface. The trend line for the leading edge suction surface indicates a sudden increase in normalized pressure for the tip and 70% station with increasing positive incidence angle. Although the hub runs even higher in incidence angle, no such sudden increase is noted. On the pressure surface, increasing negative incidence leads to a sudden increase in normalized pressure. Examining the data presented in the manner of Figure 22 now shows that the illustration of normalized pressure difference variation with incidence is strongly influenced by the individual surface incidence. Also, anomalies in Figures 20 and 21 are seen to be created by the combination of the magnitude of the transverse perturbation velocity and the operating incidence angle.
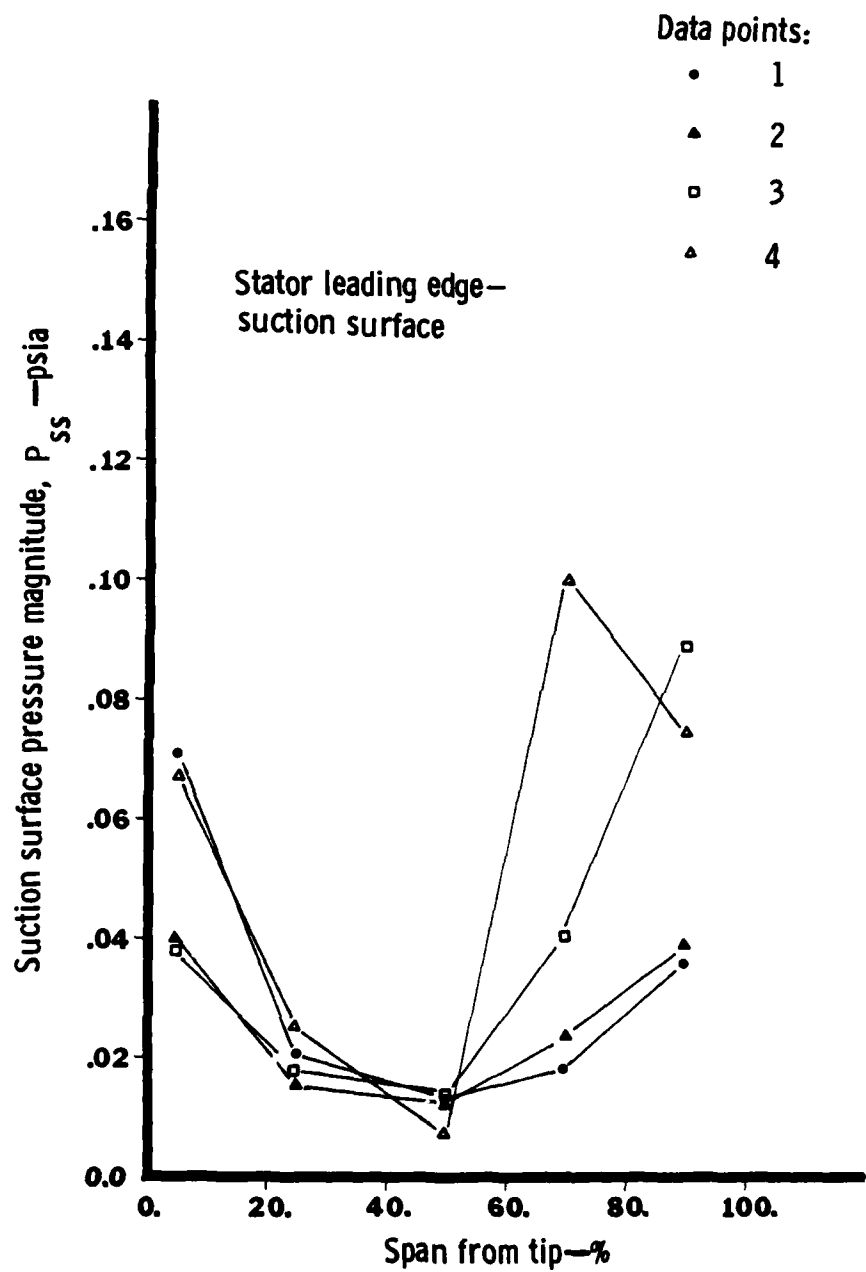
Figure 20. Radial variation of the suction surface fluctuating static
pressure at the stator leading edge.
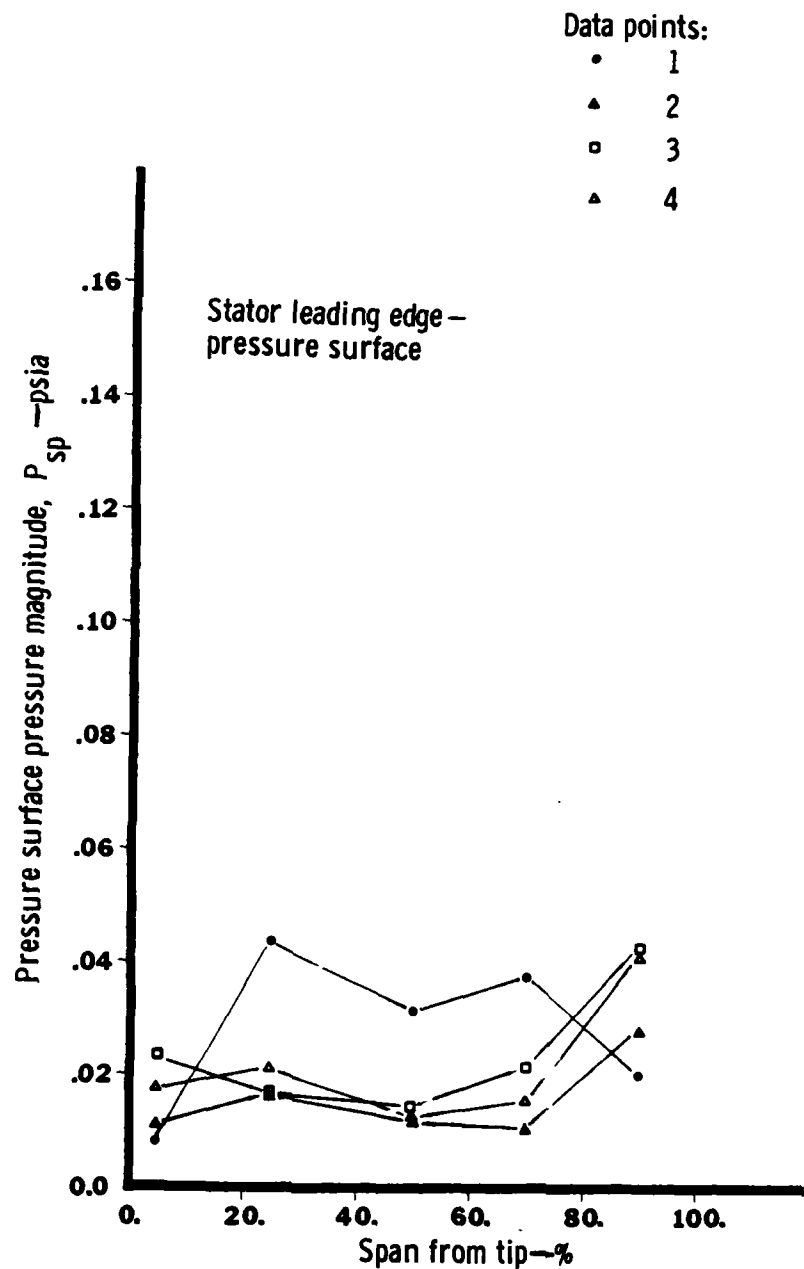
Figure 21. Radial variation of the pressure surface fluctuating static pressure at the stator leading edge.
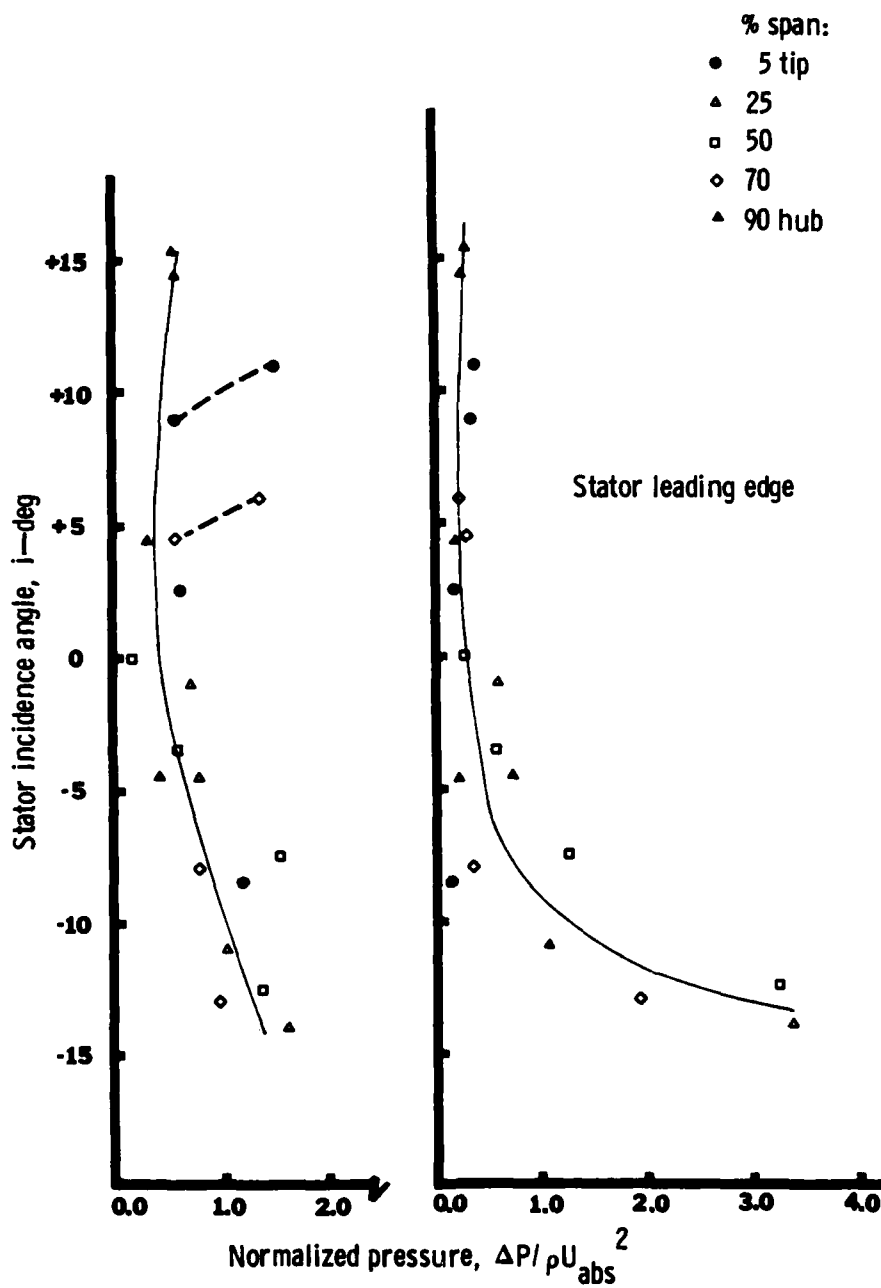
TE81-7057

Figure 22. Correlation of vane leading edge suction and pressure surface normalized pressure to the stator incidence angle.

TE81-7058

55

Figure 13 has shown that strong fluctuating velocity components prevail upstream of the vane principally on the hub and tip regions of the flow path. As these components proceed downstream and are impressed on the vane leading edge at varying degrees of incidence, the flow may alternately separate from the suction and pressure surfaces. Since the results presented in Figure 22 resemble a blade element incidence-loss bucket, it is implied that flow separation from the airfoil surfaces may be a prime variable in influencing the dynamic pressure amplitude.

The phase angles of the pressure perturbations along the leading edge are presented for both surfaces in Figures 23 and 24. The differential phase angles between the two curves are not 180 deg, which is somewhat surprising at the leading edge. Data from points 1 and 2 follow similar trends, as do data from points 3 and 4.

Figures 25 and 26 present the pressure magnitudes and phase angles for the trailing edge Kulites. No real trends are noted from either. The only relative comment is that the magnitude of the pressure disturbance is substantially lower than that of the leading edge.

In the following discussion, only the normalized pressure distributions will be presented. The tabulated pressure data are included for reference in the appendix.

In Figures 27, 28, and 29, the normalized pressure distributions along the chord of the stator for the near hub, inner diameter station; mean radial station; and near tip, outer diameter station are presented. The hub section has the smallest normalized pressure distribution, while the mean-line section has the largest chordwise normalized loading. As discussed previously, the normalized pressure magnitudes are influenced strongly by the operating incidence angle. In the mean-line plot, Figure 28, the overall chordwise loading can be seen to be influenced by the operating incidence angle. The phase angles of these stations are presented in Figures 30, 31, and 32, respectively. In each figure, the phasing is seen to be influenced greatly by loading. However, no clear trends are obvious from these phasing data.
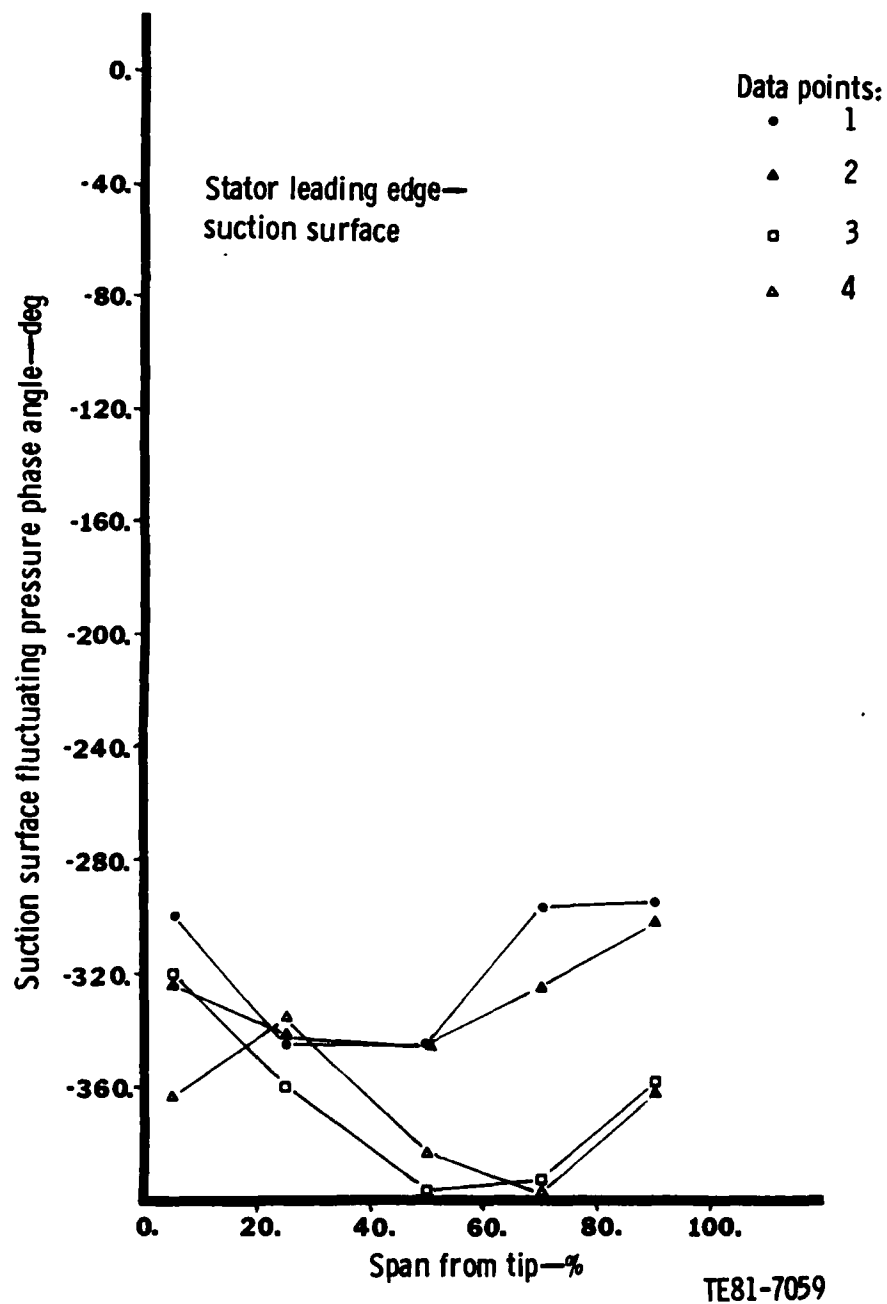
Figure 23. Radial variation of the suction surface fluctuating pressure phase angle at the stator leading edge.

57
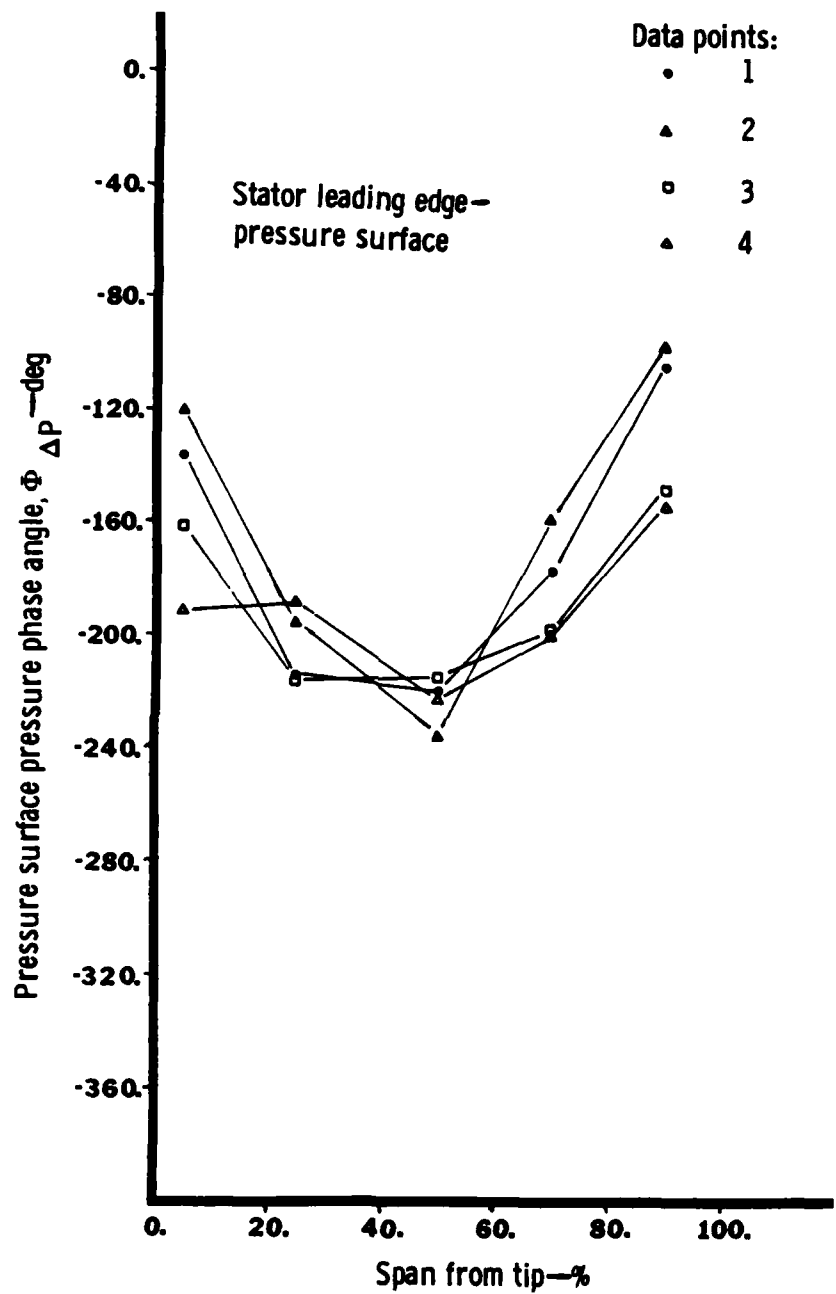
Figure 24. Radial variation of the pressure surface fluctuating pressure
phase angle at the stator leading edge.

TE81-7060

58
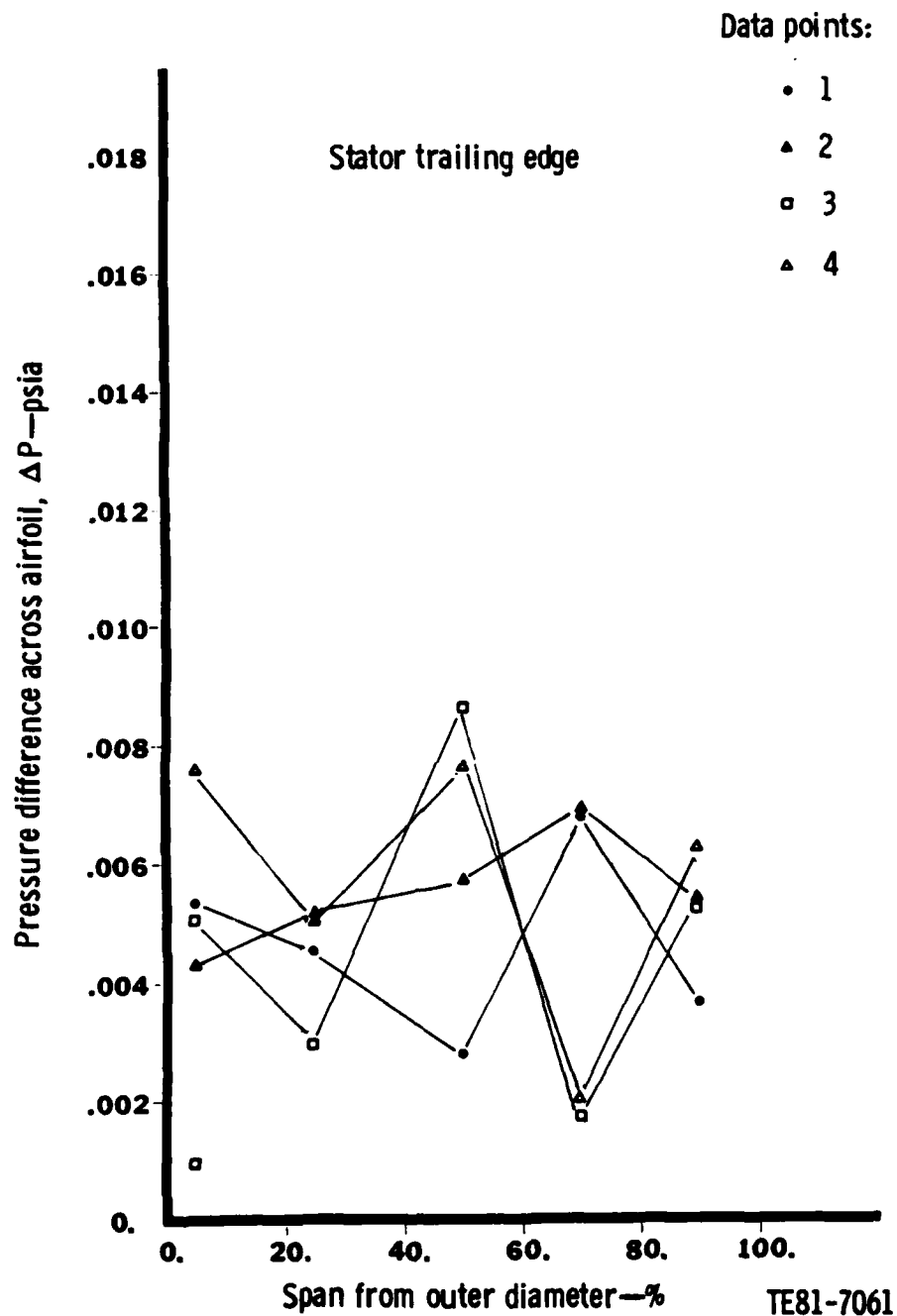
Figure 25. Radial variation of fluctuating pressure difference across
stator at trailing edge.
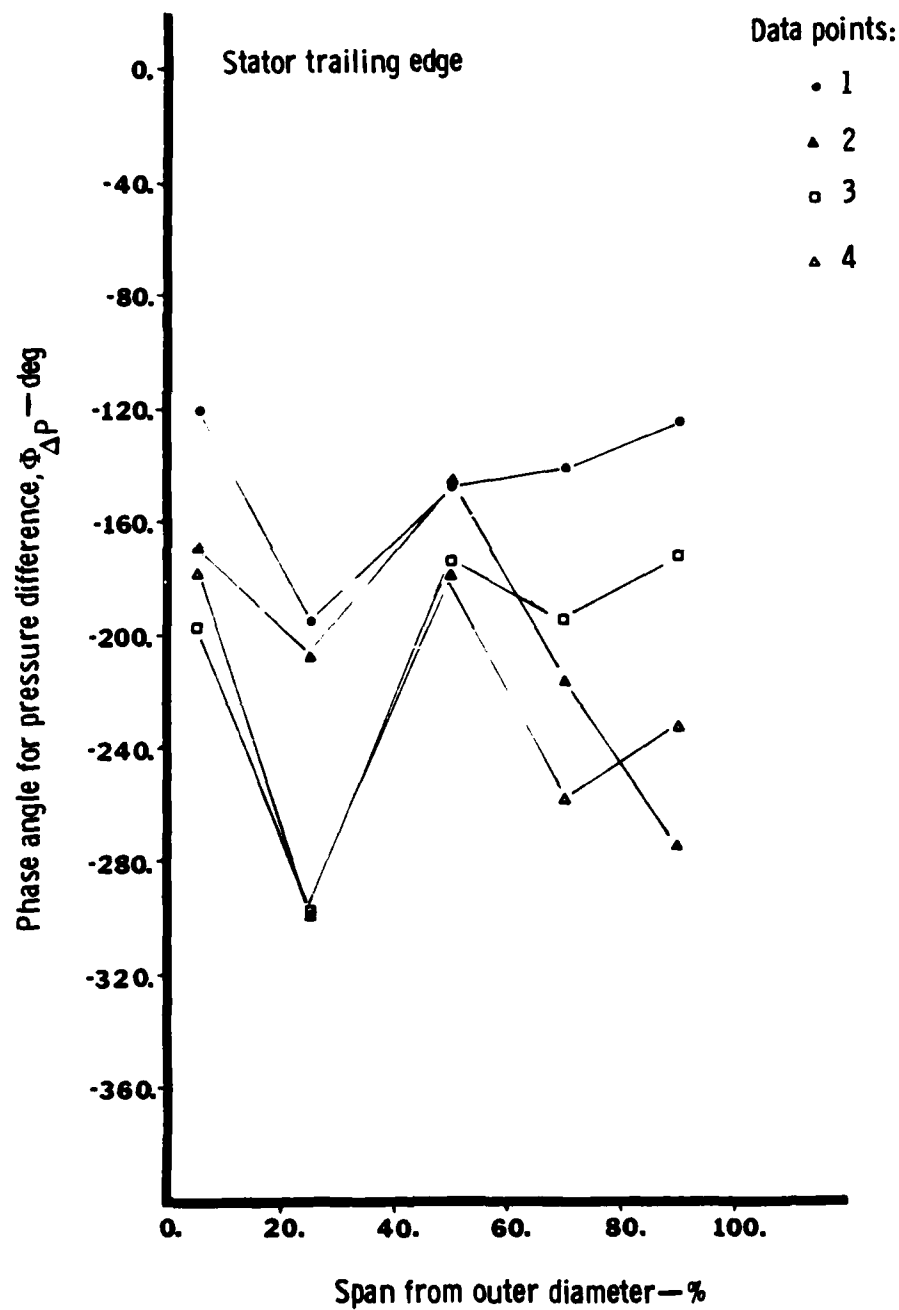
Figure 26.   Radial variation of fluctuating pressure difference phase
angle across stator at trailing edge.
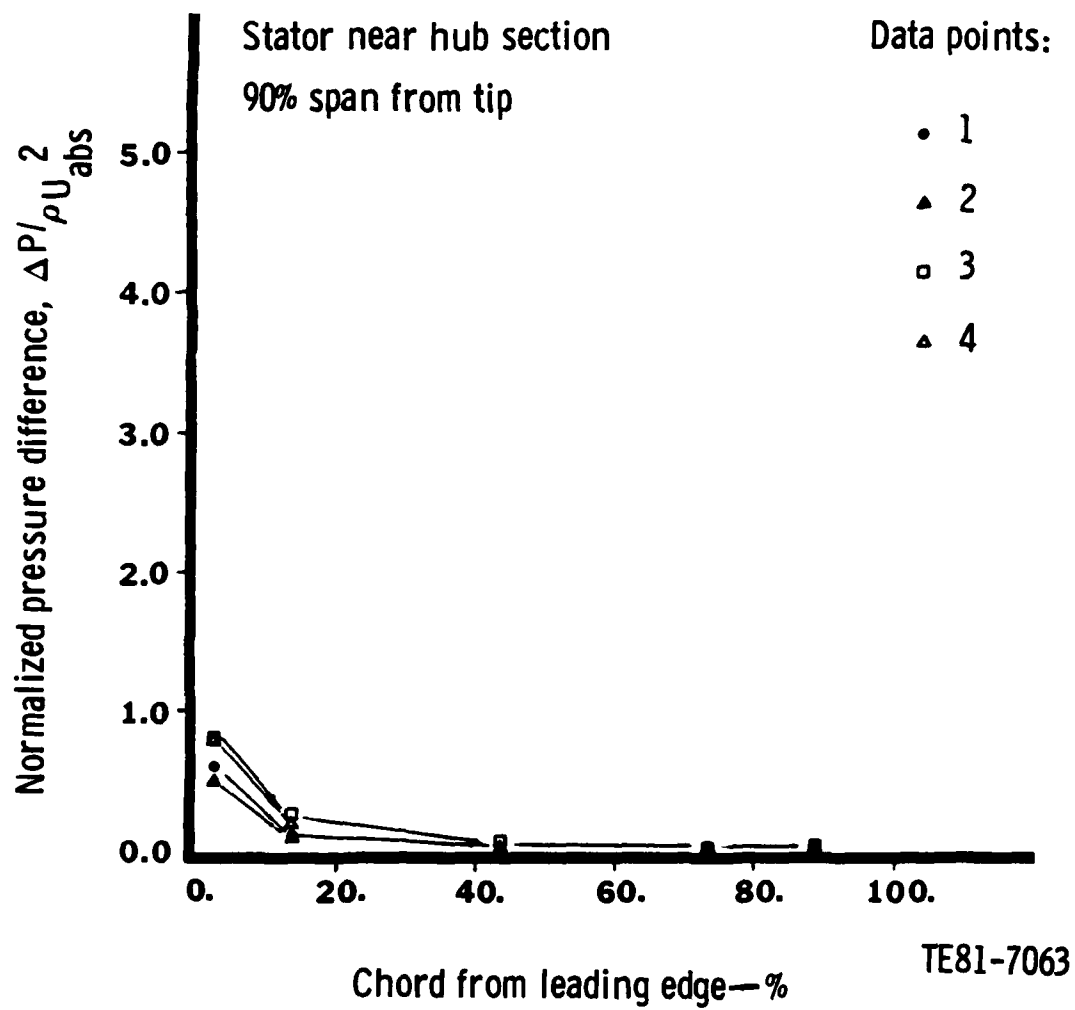
TE81-7062

Figure 27.   Variation of normalized pressure difference along chord at stator near hub section.

61
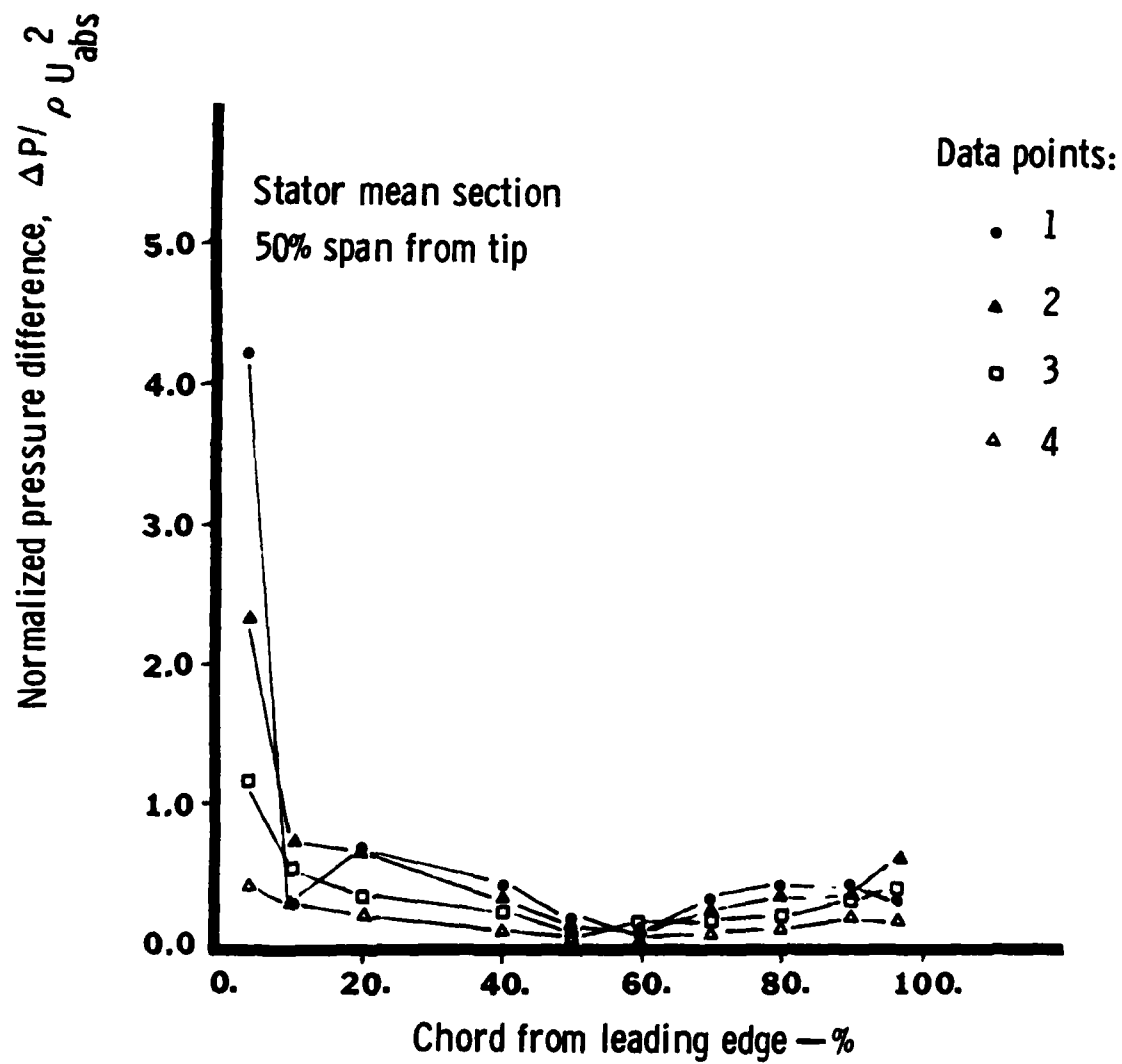
Figure 28. Variation of normalized pressure difference along chord at
stator mean section.
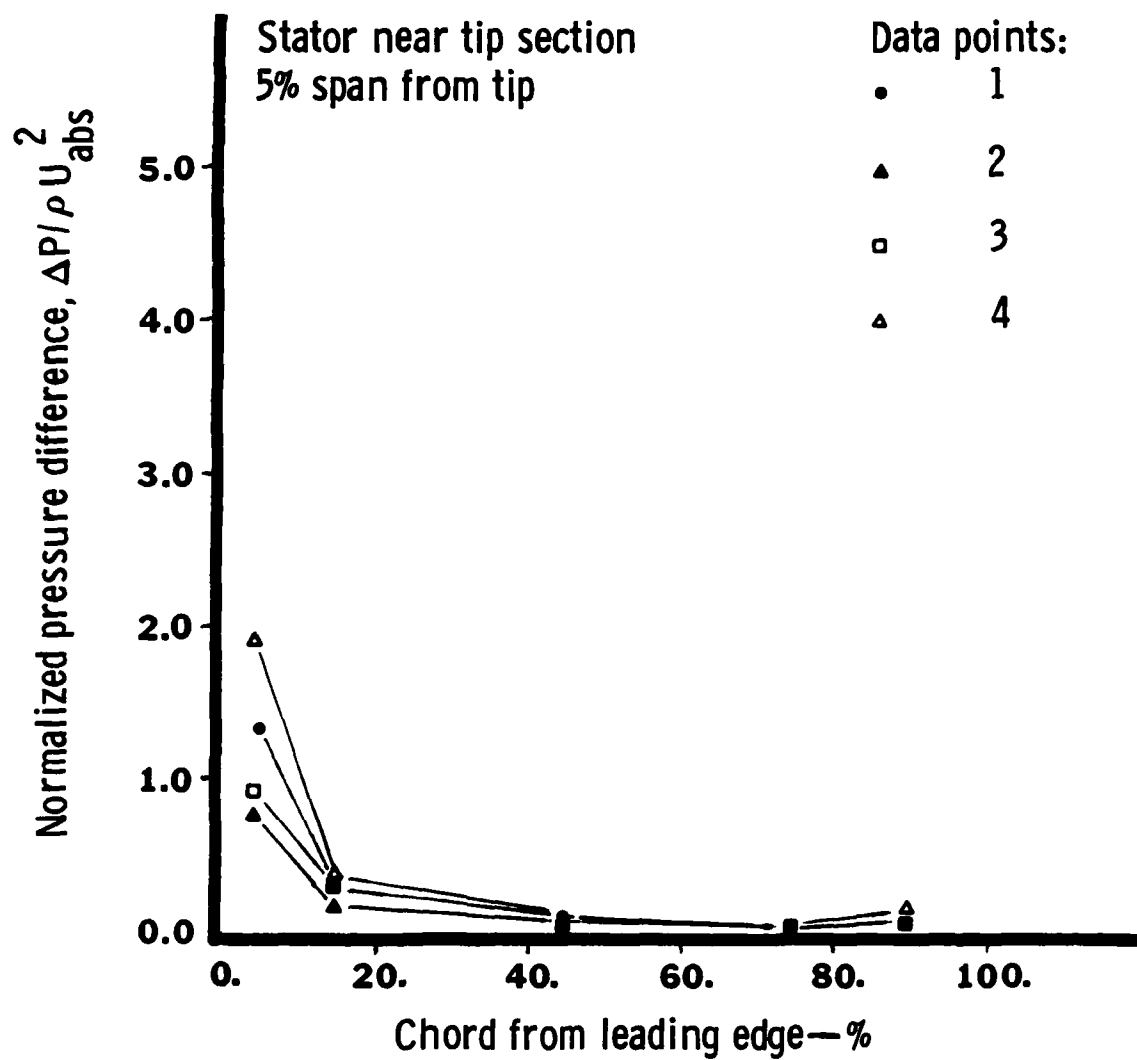
Figure 29. Variation of normalized pressure difference along chord at stator near tip section.
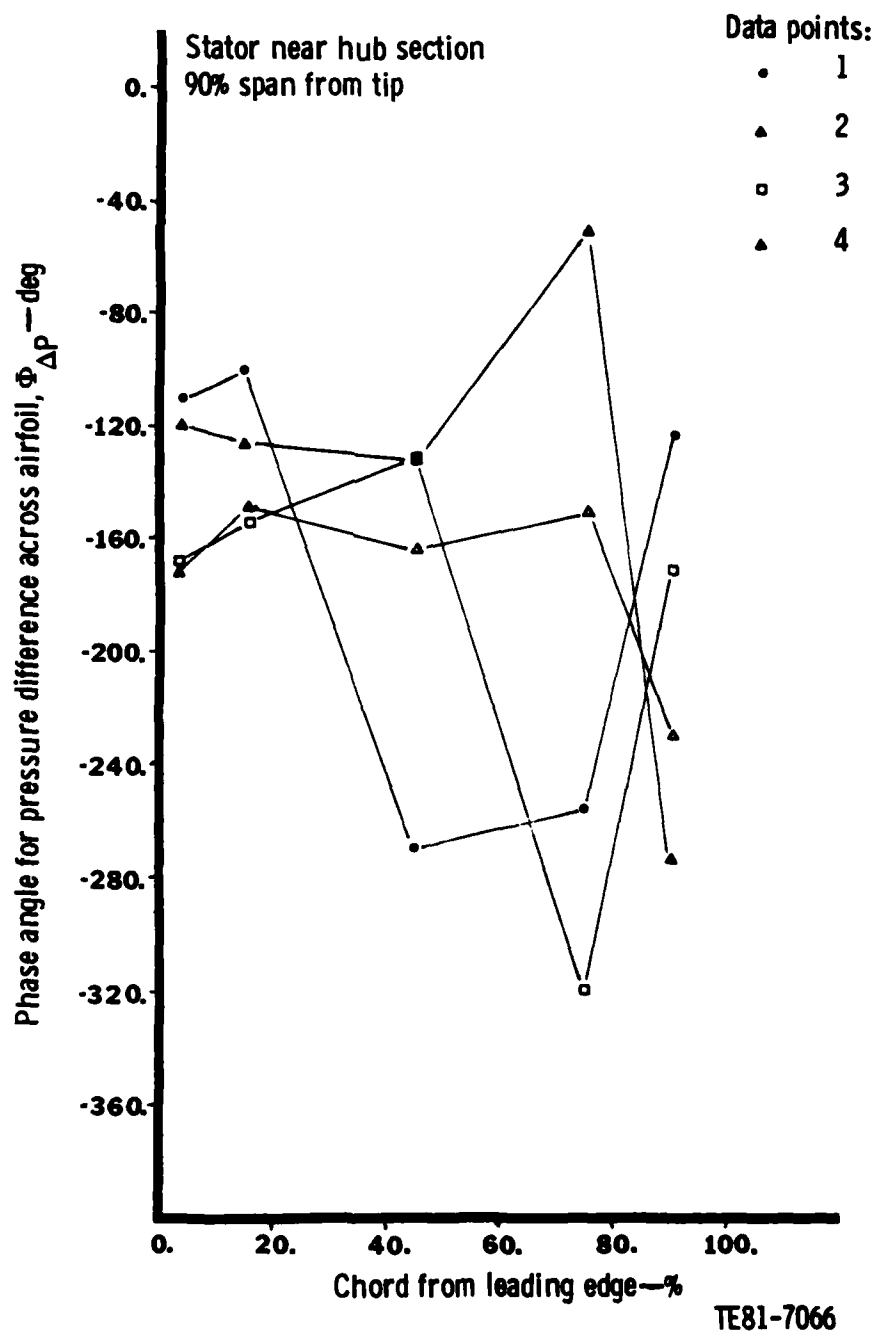
Figure 30. Variation of pressure difference phase angle along chord at stator hub section.
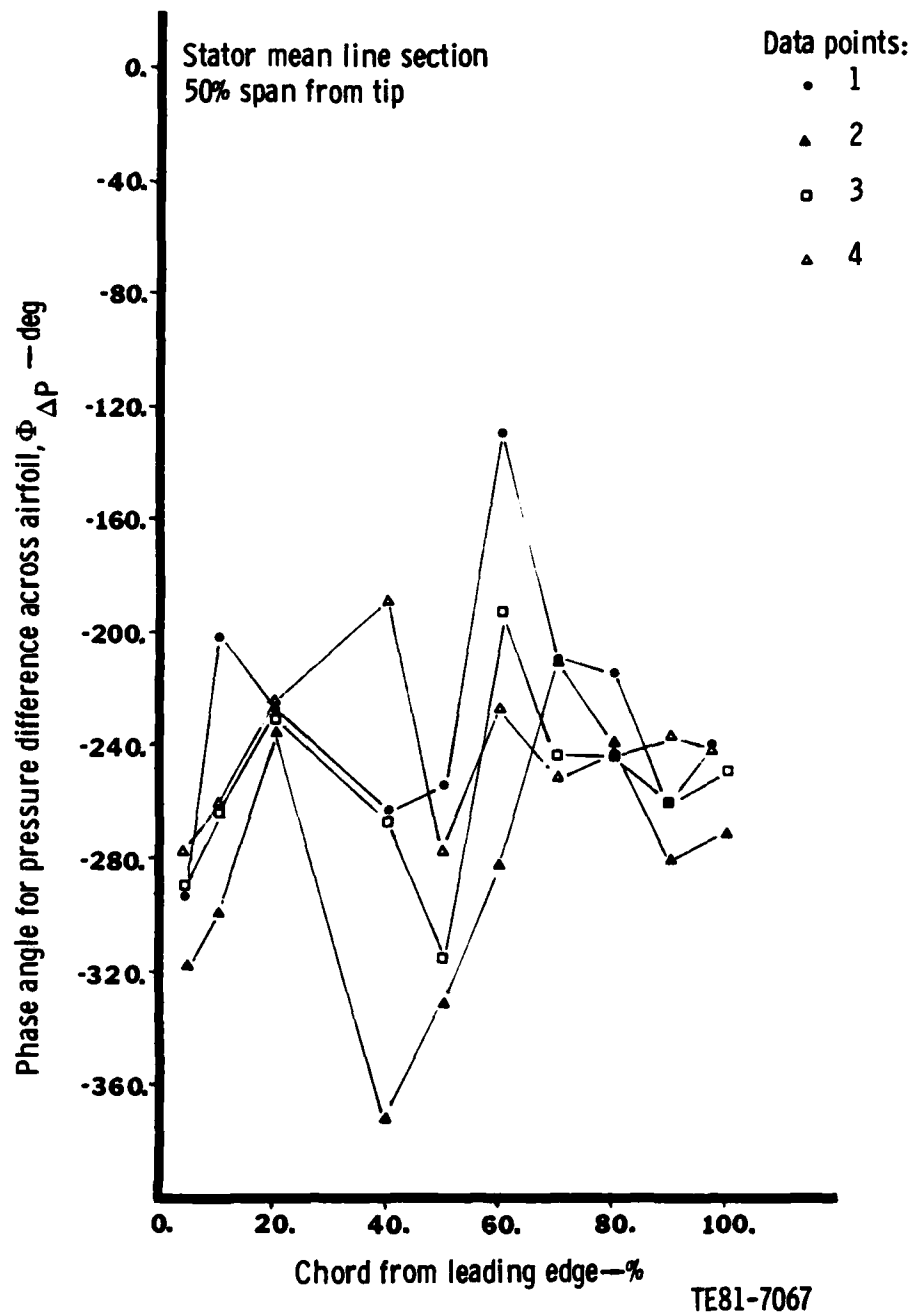
TE81-7066

TE81-7067

Figure 31. Variation of pressure difference phase angle along chord of
stator mean section.

65
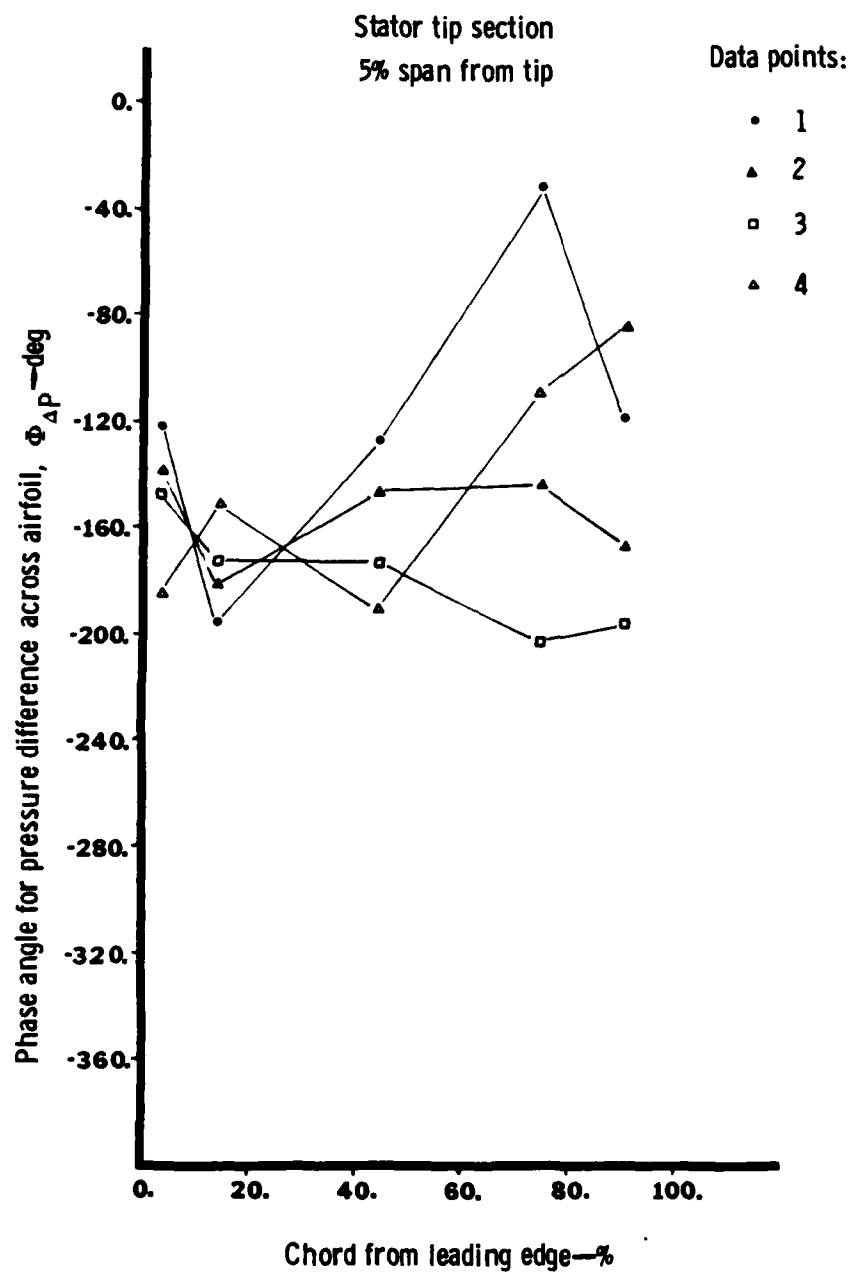
Figure 32.   Variation of pressure difference phase angle along chord at
stator tip section.

A note regarding the normalized data must be made. Although the normalized pressure magnitude may be larger at the mean line than at either the hub or tip of the stator, it must be remembered that in terms of actual pressures, the mean line has the smallest values.

Repeatability and correlation of experimental data are always of great concern. In Figures 33, 34, 35, and 36, data taken during this experiment is compared with both the data taken in 1977 and the analytical results from the DDA unsteady aerodynamic model.

Comparison with Analytical Prediction

In the DDA analytical formulation, the cascade is represented as a two-dimensional array of arbitrary airfoils having both thickness and camber. The flow is constrained to remain subsonic throughout the field; however, nonzero incidence angles are permissible. A finite difference numerical technique is employed to solve the linearized differential equation in the near field. Far field energy radiation conditions are satisfied by matching numerical results to analytical expansions at arbitrary planes upstream and downstream of the cascade. The presence of the steady pressure field causes a skewing of the incoming disturbance field as it passes through the cascade. This phenomenon can result in dramatic changes in both unsteady pressure amplitude and phase. There are presently no other analyses available for prediction of gust-induced loading that are this general.

In Figures 33 and 34 the comparison between experimental data gathered in 1977 and data from this experiment reveals striking similarities. Overall and detailed trends remain the same, as do the quantitative values. The open throttle point, DP 1, is the object of comparison in these two figures. The DDA gust analysis does not represent the physical phenomena well, particularly with respect to phase angle. In Figures 35 and 36, experimental data gathered at the design point DP 3 are presented. Again, good repeatability over a number of years is demonstrated. However, even at this low incidence condition, the analytical model is not descriptive of the physical processes.
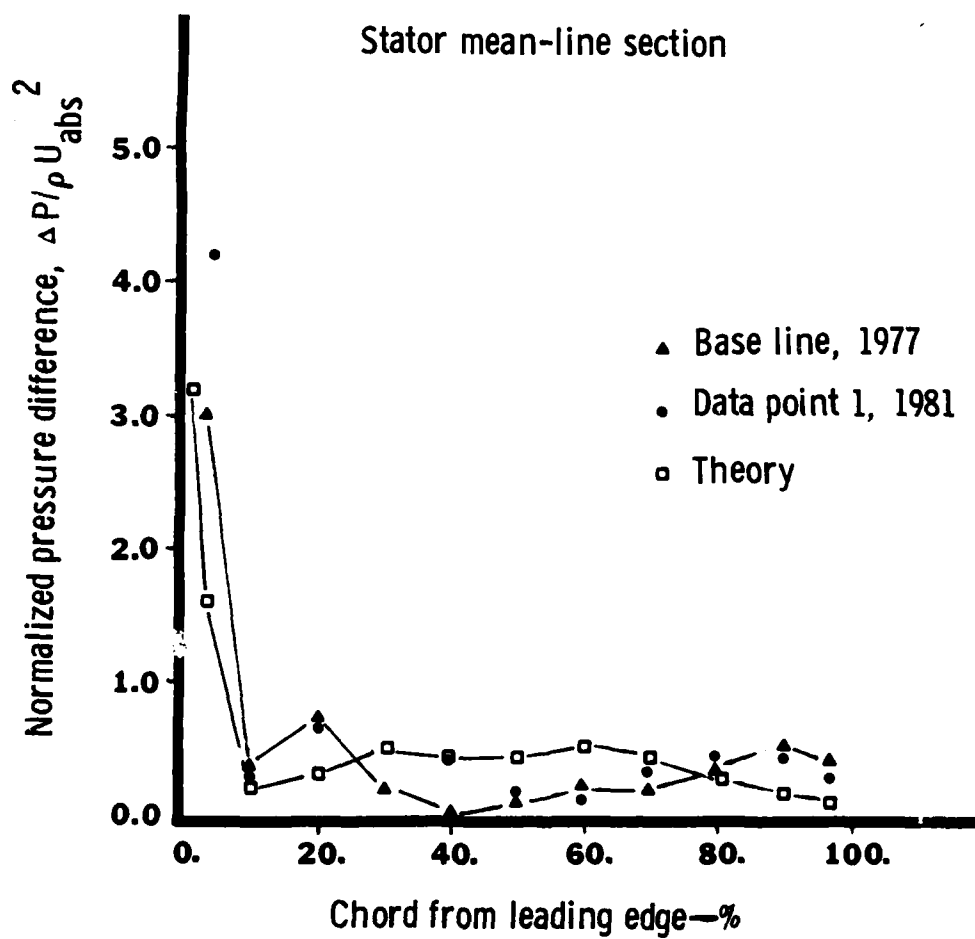
Figure 33. Comparison of stator mean-line 1981 data point 1 normalized
pressure results with similar 1977 results and analytical prediction.
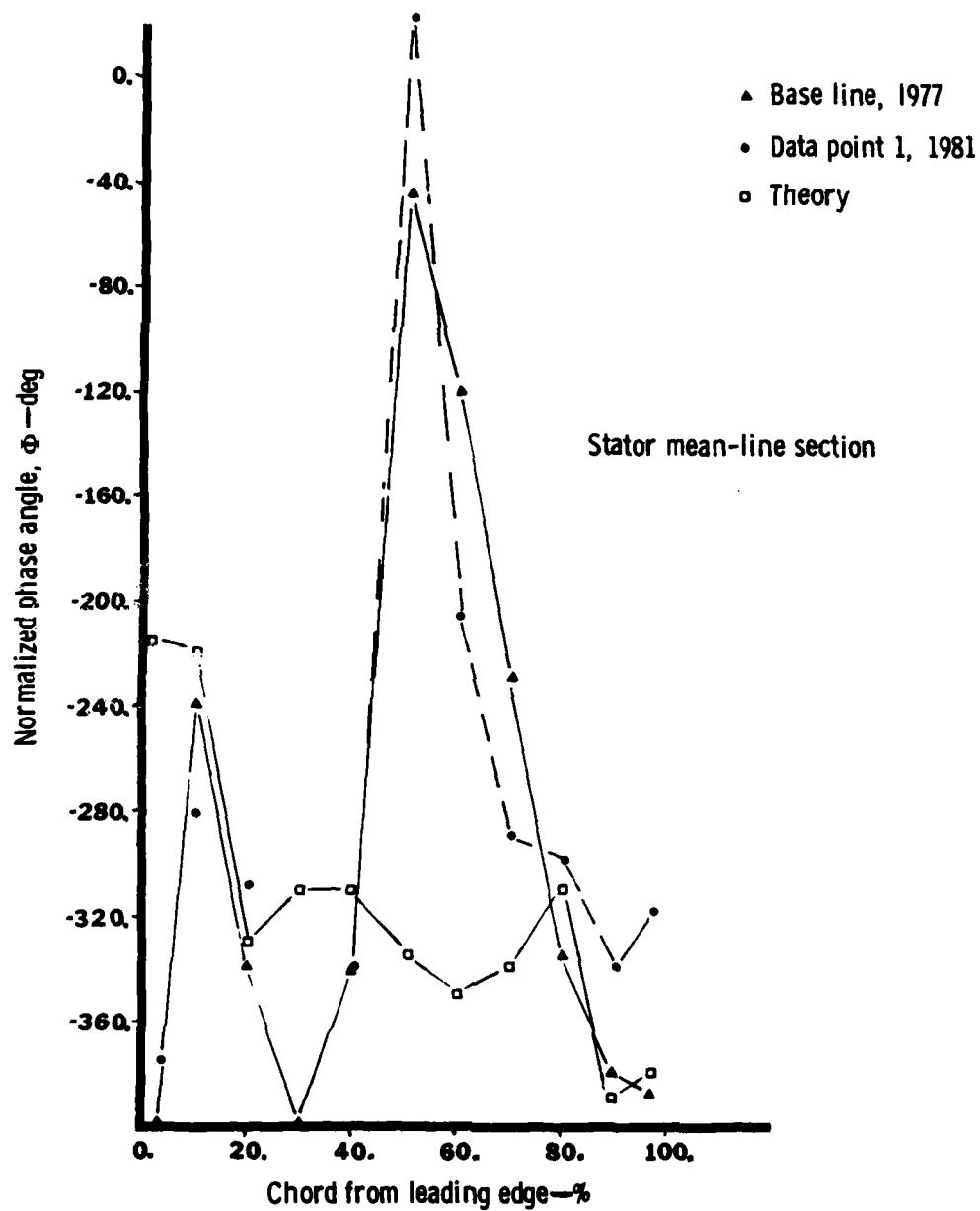
TE81-7069

Figure 34. Comparison of stator mean-line 1981 data point 1 phase angle
results with similar 1977 results and analytical prediction.

TE81-7070

69
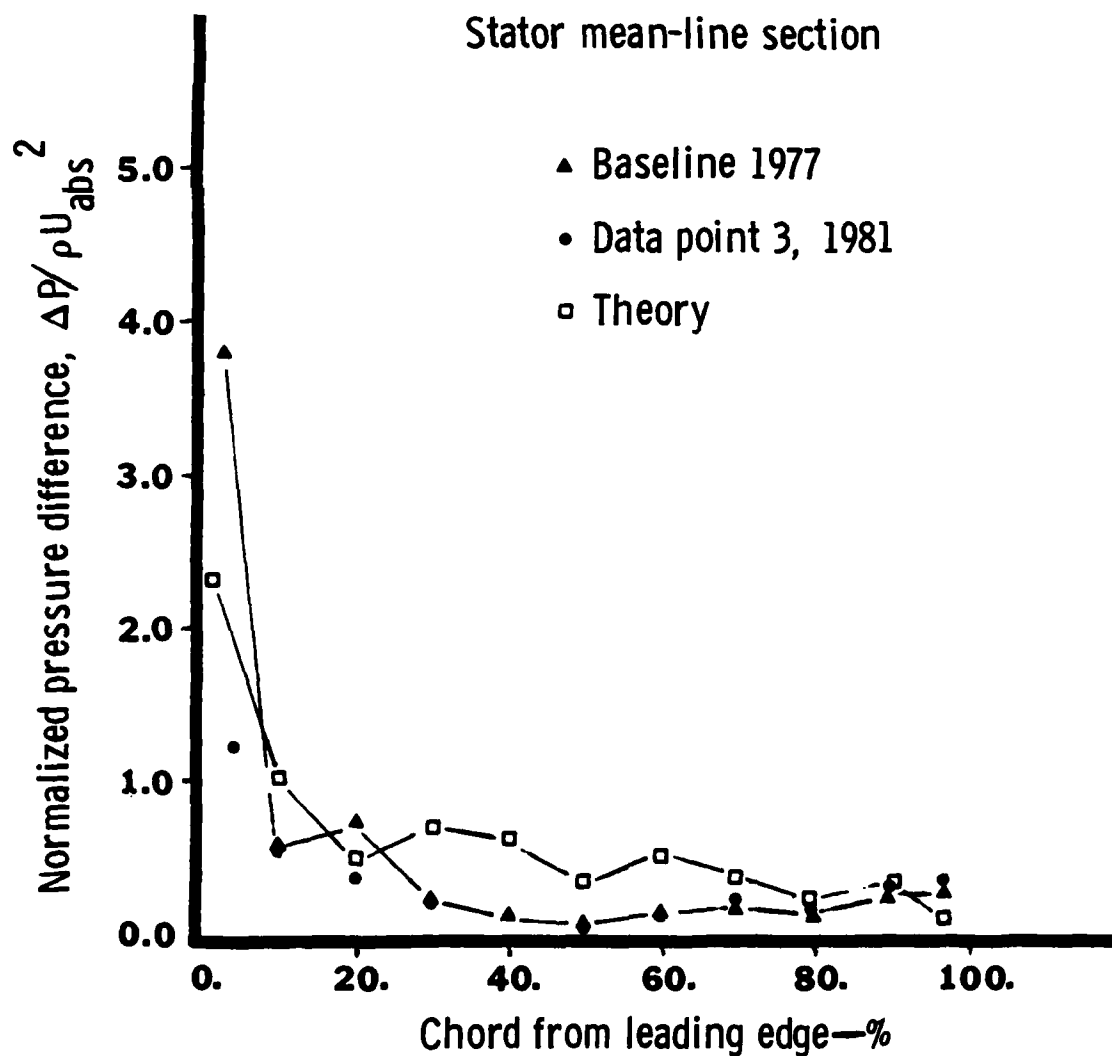
Figure 35. Comparison of stator mean-line 1981 data point 3 normalized pressure results with similar 1977 results and analytical prediction.
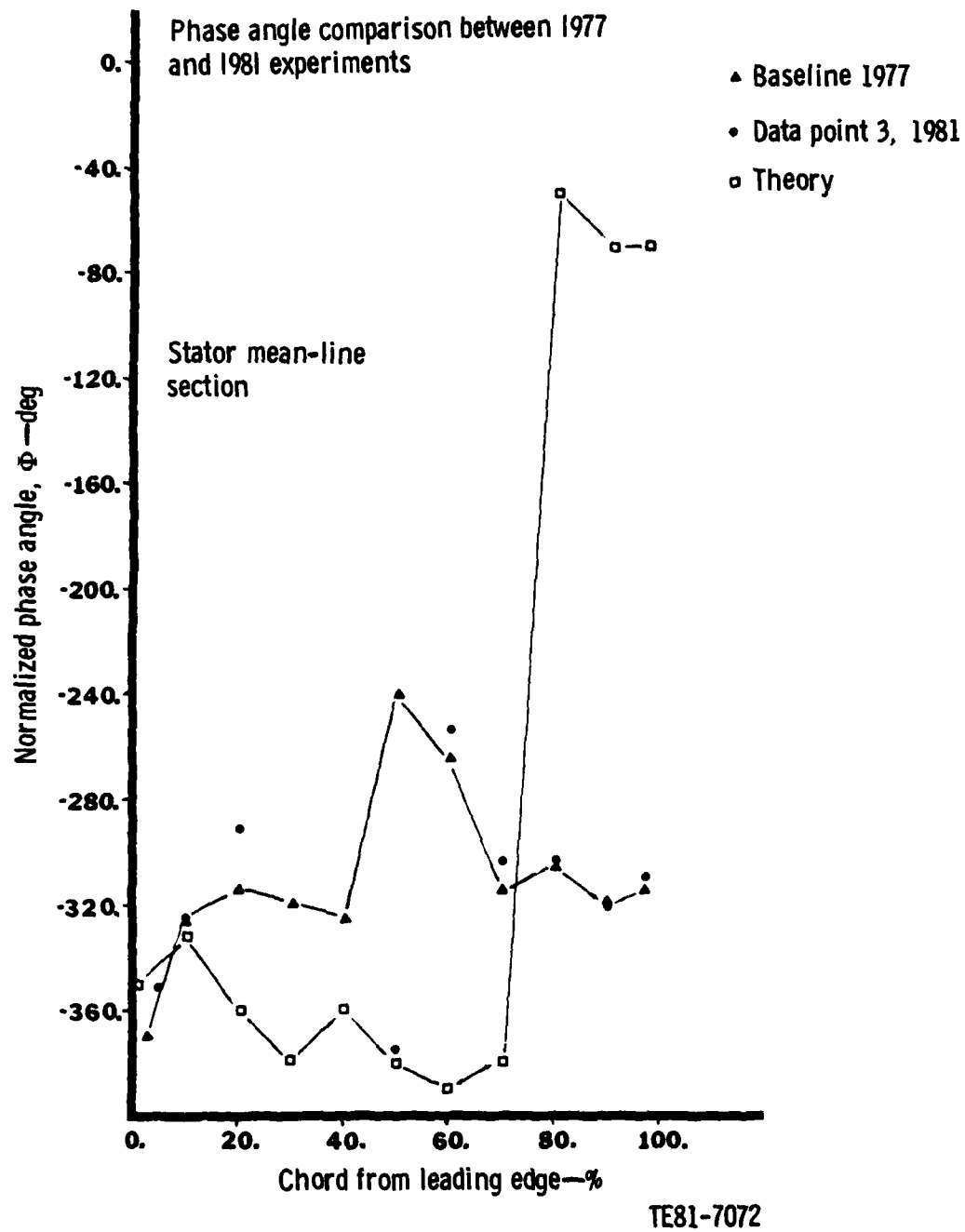
Figure 36.   Comparison of stator mean-line 1981 data point 3 phase angle
results with similar 1977 results and analytical prediction.

Summary

From the results of the pressures induced on the stator airfoil surfaces by
the passage of upstream rotor blades, it can be clearly seen that different
phenomena dictate behavior in the hub, mean, and tip regions. The three-di-
mensional aspects of the fluctuating pressures have been presented and dis-
cussed. Examination of the time-variant pressures has identified two strong
variables: the operating incidence angle and the normalized transverse per-
turbation velocity. Analytical results indicate a weakness in obtaining pro-
per representation of the induced pressure magnitudes and phase relationships.

HOT WIRE ANEMOMETER WAKE MEASUREMENTS

As noted earlier, hot wire anemometer surveys were performed at various ra-
dial, circumferential, and axial stations throughout the compressor stage as
it operated at eight different conditions of corrected speed, flow, and pres-
sure ratio. In general, the variations of the fluctuating streamwise (ΔU) and
transverse (ΔV) velocity component magnitude and phase angle with radius and
axial location were affected somewhat by compressor loading. However, it was
felt that the most informative method of presenting the results would be to
examine one point (e.g., the near-design operating point, DP 3) in particular,
and to both quantitatively and qualitatively describe the distribution of the
dynamic velocity components generated by the rotor blade wake throughout the
complete compressor stage. Similar conclusions would be drawn by examining
any one of the remaining seven operating conditions.

Qualitative Description of Flow Field (Data Point 3)

Figures 37 through 41 represent the variation of the steady and fluctuating
velocity components at various radial stations throughout the stator passage
when the compressor was operating at near design aerodynamic conditions (DP
3). The components were normalized by the value of the stator inlet, midpas-
sage absolute velocity vector. All velocities were corrected to standard day
inlet conditions. The components were drawn to scale and show the streamwise
(ΔU) and transverse (ΔV) fluctuating components superimposed on the steady
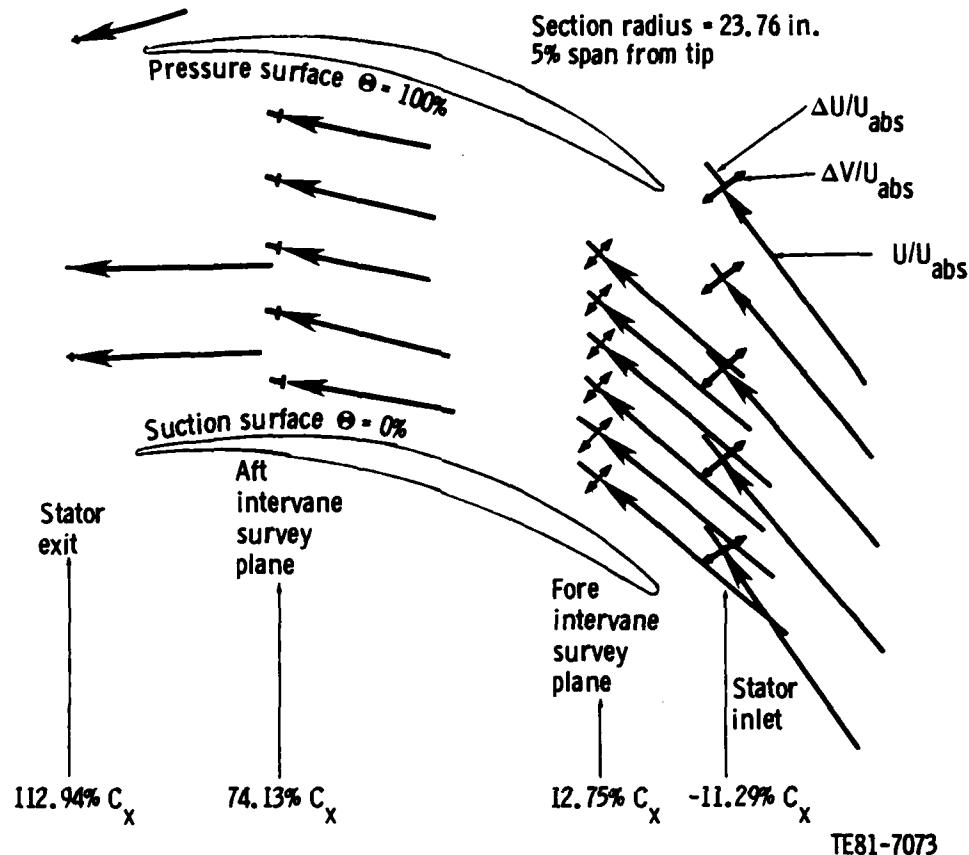
Figure 37. Qualitative description of steady and fluctuating velocity vectors at 23.76-in. radius for compressor at near-design operating conditions.

velocity component. It can be noted from Figure 37, which represents the flow field at 5% span from the tip wall, that there are very large ΔV and ΔU fluctuations at the vane inlet. They are approximately 20% and 10%, respectively, of the free-stream velocity magnitude. As the flow proceeds into the stator passage, the fluctuating velocity magnitudes are damped and barely discernible at the vane exit plane.

Examination of the fluctuating velocity components at the other radial stations (Figures 38 through 41) shows a similar trend of the fluctuating components being strongly damped by the time the flow arrives at the stator exit. Note that the fluctuating components (especially ΔV) are very large near the endwalls (20%-30% of the free-stream value) and yet are only about 10% of free

73
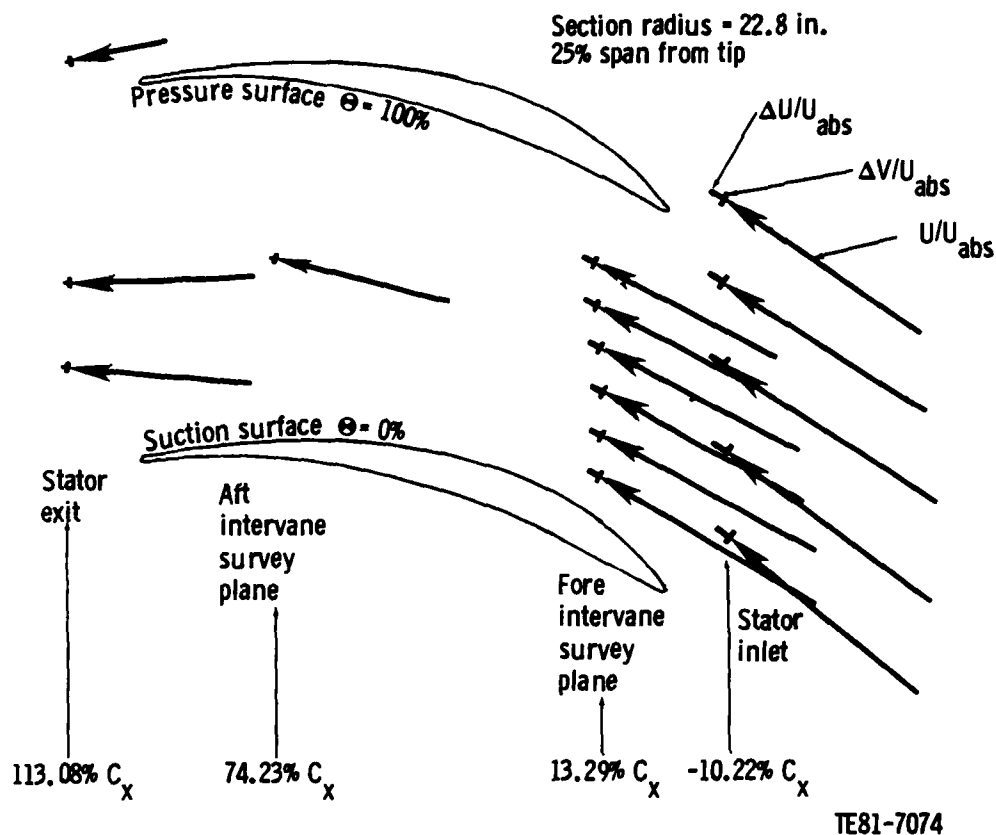
Figure 38. Qualitative description of steady and fluctuating velocity vectors
at 22.80-in. radius for compressor at near-design operating conditions.

stream at the midspan section. Based on previous research on this compressor
stage with much smaller blade tip clearances, in which detailed radial-circum-
ferential aerodynamic surveys were taken, it is recognized that the experi-
mental results at radial sections of 5% span (near the tip) and 70% and 90%
span (near the hub) are in regions where the endwall boundary layers exert a
strong influence on the flow field. These endwall boundary layers are the
result of flow conditions that developed inside the rotor blade passage, re-
sulting in broad wakes and, hence, the shedding of large ΔV and ΔU fluctua-
tions from the passing rotor blades. It is noted from Figures 37 (5% span),
40 (70% span), and 41 (90% span) that the fluctuating components are largest
at the radial locations. It is speculated that if the blade had been operated
with much smaller tip clearances and was more lightly loaded in the endwall

74
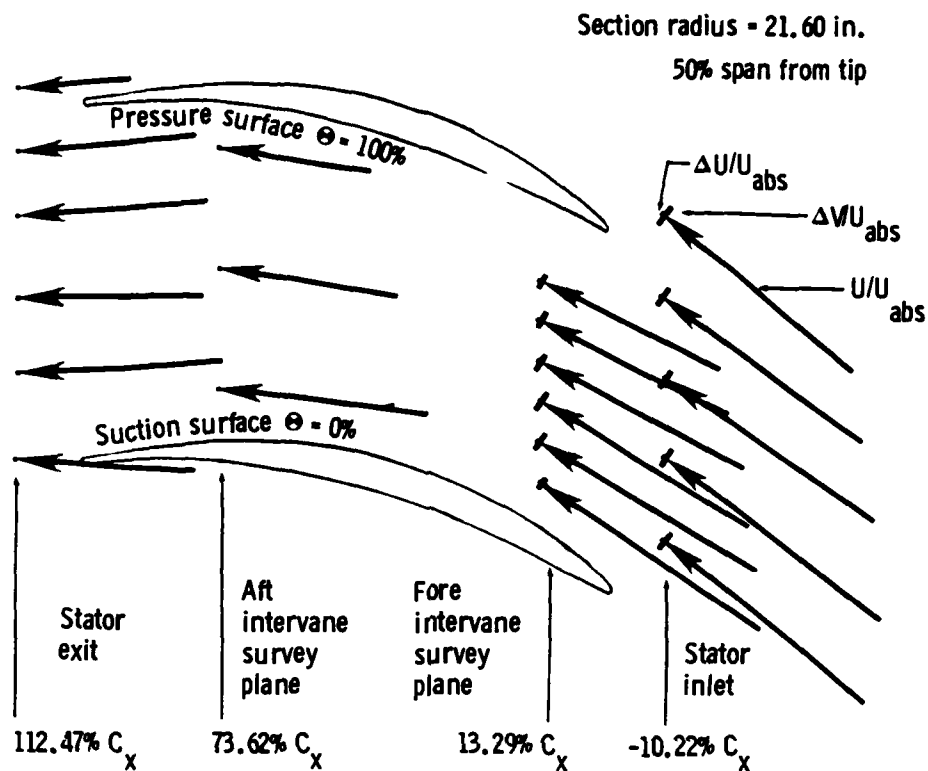
Figure 39. Qualitative description of steady and fluctuating velocity vectors at 21.60-in. radius for compressor at near-design operating conditions.

region, much smaller wakes and, hence, smaller ΔV and ΔU fluctuations would prevail in the endwall regions immediately upstream of the stator.

Quantitative Description of Flow Field

Figures 37 through 41 are a qualitative description of the variation of the steady and fluctuating velocity components in the stator passage. Figures 42 through 46 and 47 through 51 describe the variation of fluctuating components, ΔV and ΔU, respectively, at various radii as they move axially through the stator. For example, Figure 42 shows that at the 5% span section, the ΔV fluctuation was approximately 11% chord upstream of the vane, approximately 20% of the inlet absolute velocity level in the axial plane.

75

Section radius = 20.64 in.
70% span from tip

Pressure surface $\Theta = 100\%$

$\Delta U/U_{abs}$

$\Delta V/U_{abs}$

U/U_{abs}

Suction surface $\Theta = 0\%$

Stator exit	Aft intervane survey plane	Fore intervane survey plane	Stator inlet

112.40% C_x 73.73% C_x 13.24% C_x -10.18% C_x
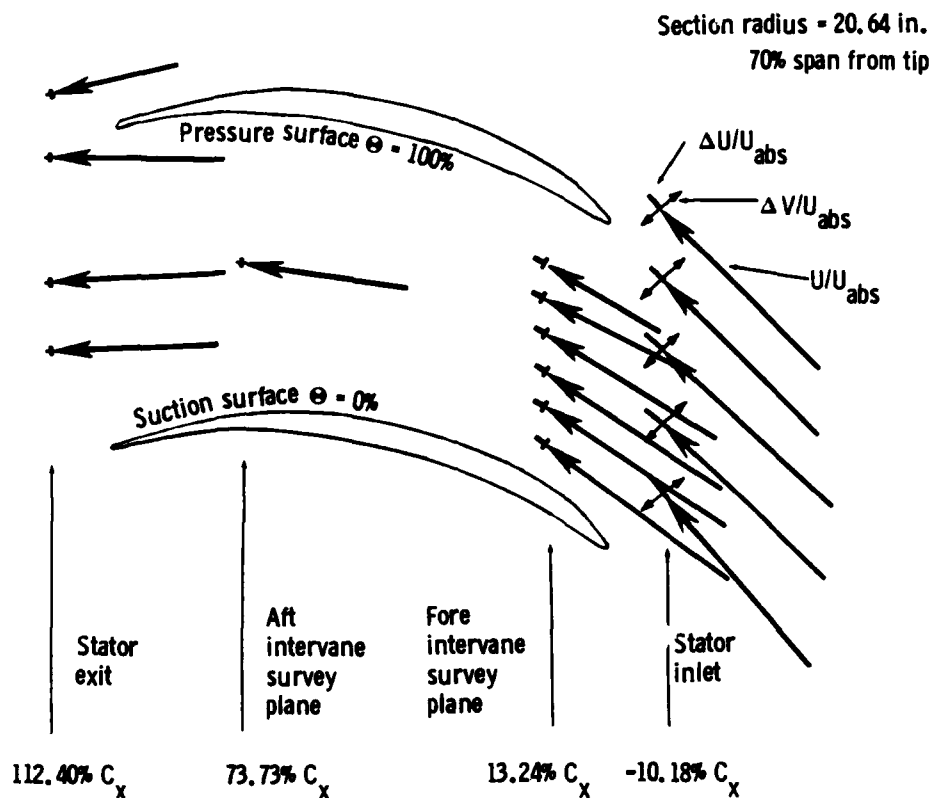
TE81-7076

Figure 40. Qualitative description of steady and fluctuating velocity vectors at 20.60-in. radius for compressor at near-design operating conditions.

Figure 42 shows that as the flow proceeds through the stator, ΔV is damped out to only about 1% of the inlet velocity level. Similar observation can be made at other radial stations from Figures 43 through 46.

Quantitative variations of ΔU through stator passage are presented in Figures 47 through 51. There it can be seen that ΔU was approximately 10%-15% U_{abs} at the vane inlet but also was damped to about 1% of U_{abs} at the vane exit. Note that in the midspan region (50% span), where the blade shed relatively small, well-defined wakes, ΔU varied only from approximately 3% U_{abs} at the inlet to 1% U_{abs} at the vane exit.

76

Section radius = 19.68 in.

90% span from tip

$\Delta U/U_{abs}$

$\Delta V/U_{abs}$

U/U_{abs}

Pressure surface $\Theta = 100\%$

Suction surface $\Theta = 0\%$

| Stator exit	Aft intervane survey plane	Fore intervane survey plane	Stator inlet
110.93% C_x	73.16% C_x	13.91% C_x	-9.94% C_x
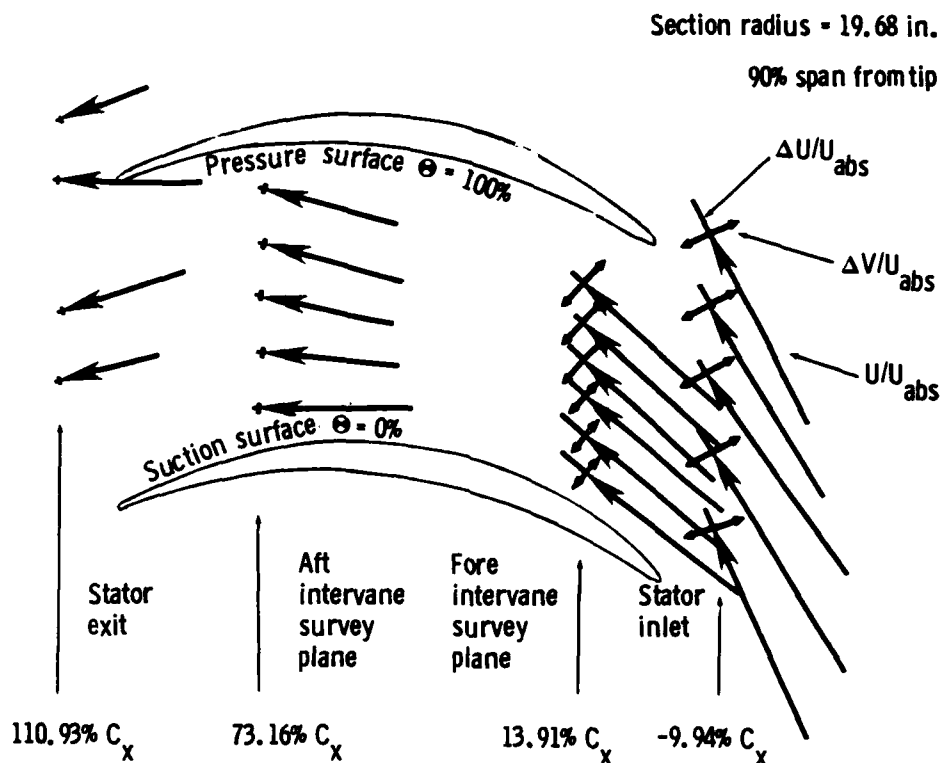
TE81-7077

Figure 41.   Qualitative description of steady and fluctuating velocity vectors at 19.68-in. radius for compressor at near-design operating conditions.

It is of interest to examine the phase relationship of the ΔV and ΔU fluctuating components in the stator passage. Figure 52 illustrates the radial variation of phase angle between the streamwise (ΔU) and transverse (ΔV) fluctuating components at one circumferential location—e.g., immediately upstream of the vane leading edge. Note that the two waves are in phase near the hub and tip but approximately 180 deg out of phase in the midspan region. No clear explanation exists for these observations at this time.

77
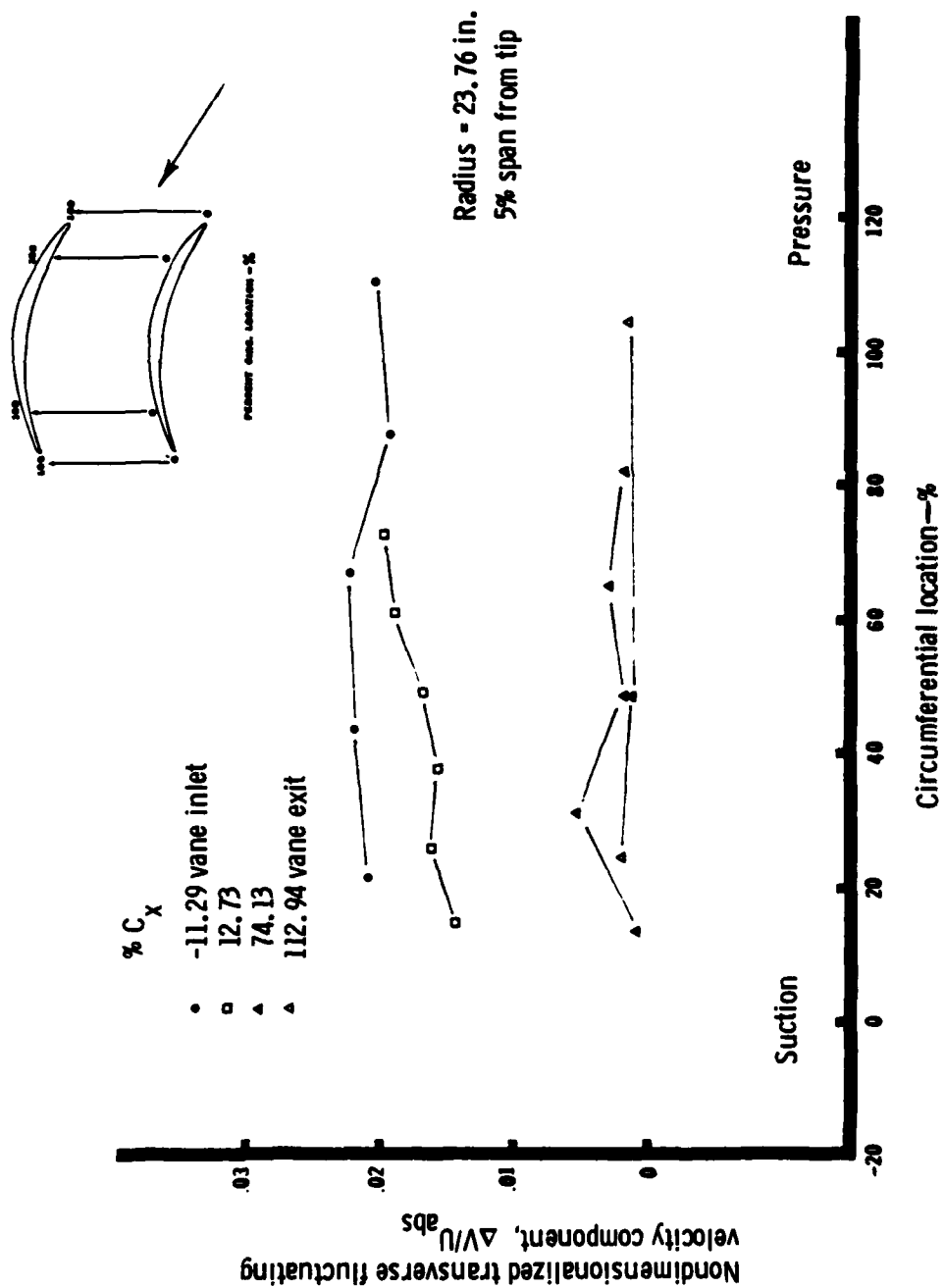
Figure 42. Circumferential and axial variation of transverse fluctuating velocity components at 23.76-in. radius for data point 3.

TE81-7078

78

Radius = 22.8 in.
25% span from tip

TE81-7079

Pressure

Circumferential location—%

Suction

% C_x

- -10.22 vane inlet
- □ 13.29
- ▲ 74.23
- ▲ 113.08 vane exit

.03

.02

.01

0

Nondimensionalized transverse fluctuating velocity component, $\Delta V/U_{abs}$
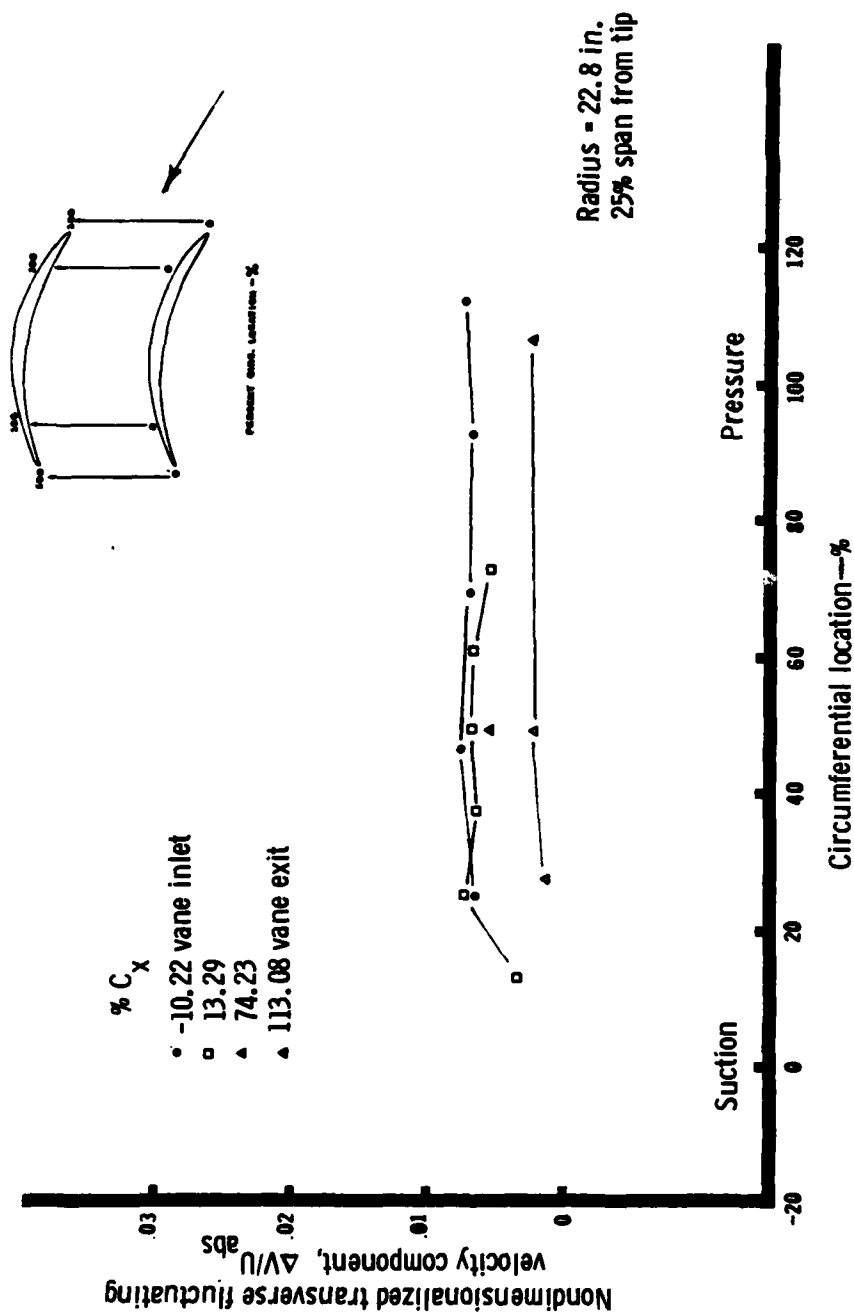
Figure 43. Circumferential and axial variation of transverse fluctuating velocity components at 22.80-in. radius for data point 3.

79
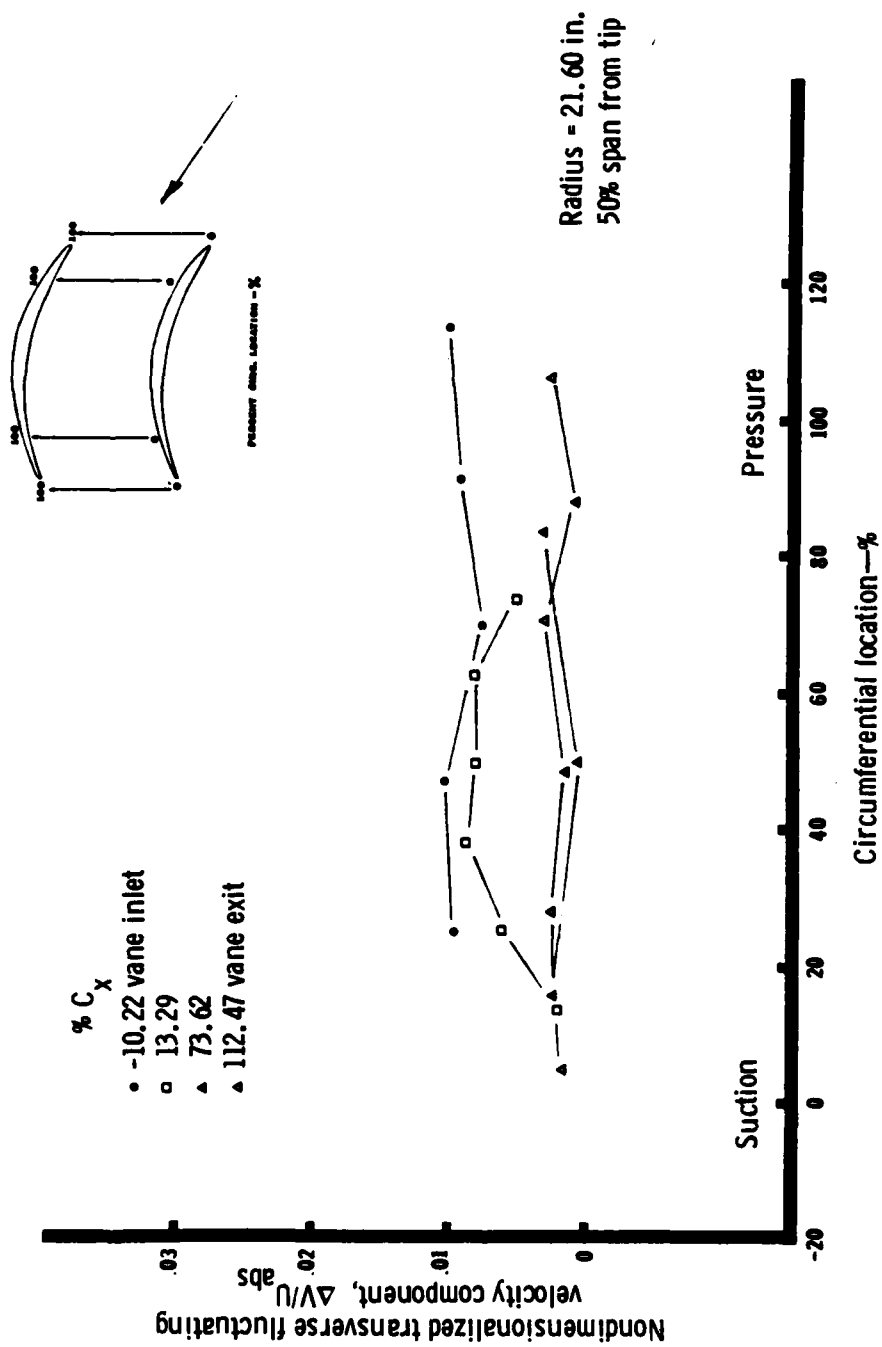
Figure 44. Circumferential and axial variation of transverse fluctuating velocity components at 21.60-in. radius for data point 3.
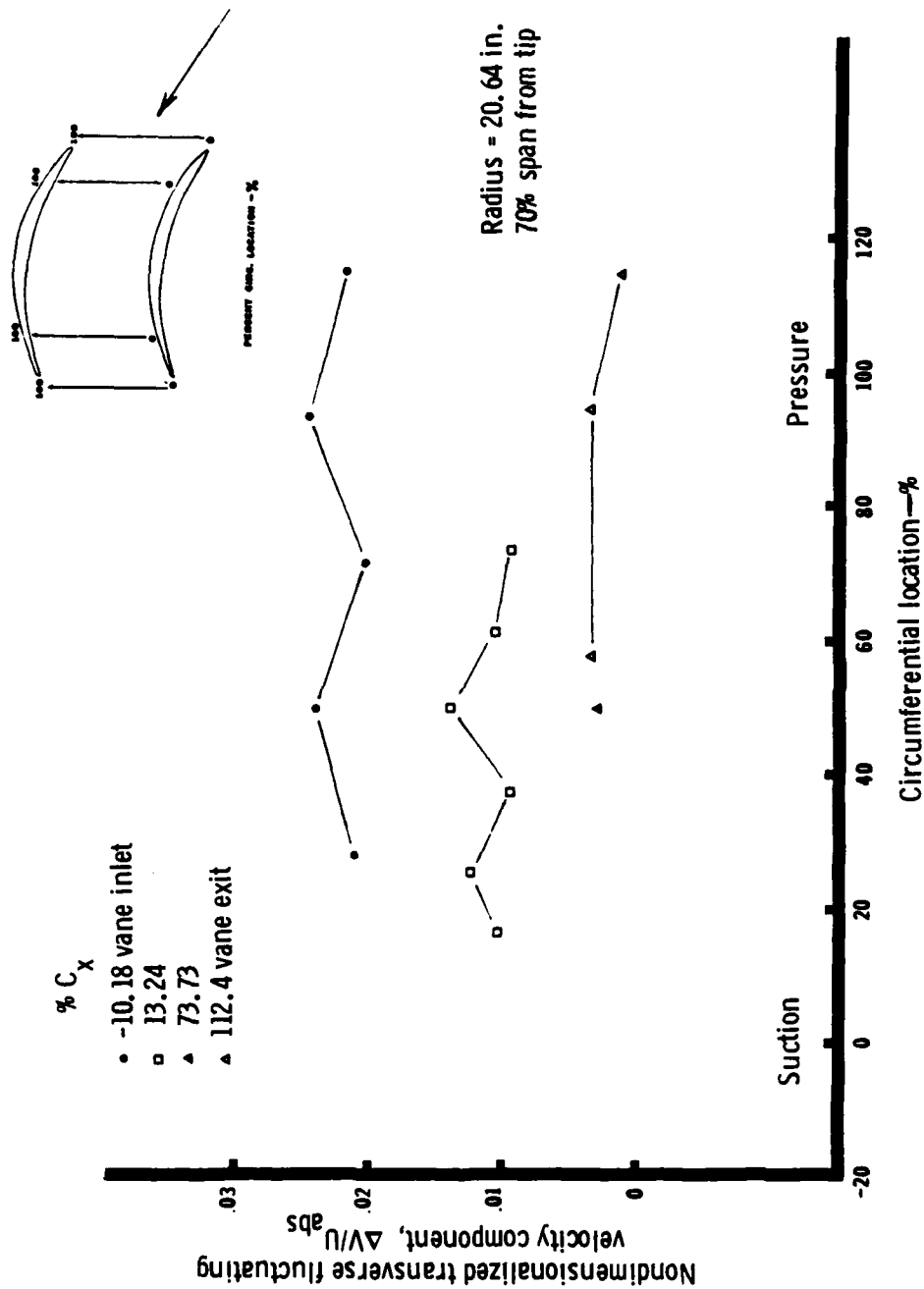
Figure 45. Circumferential and axial variation of transverse fluctuating velocity components at 20.64-in. radius for data point 3.

TE81-7081

81
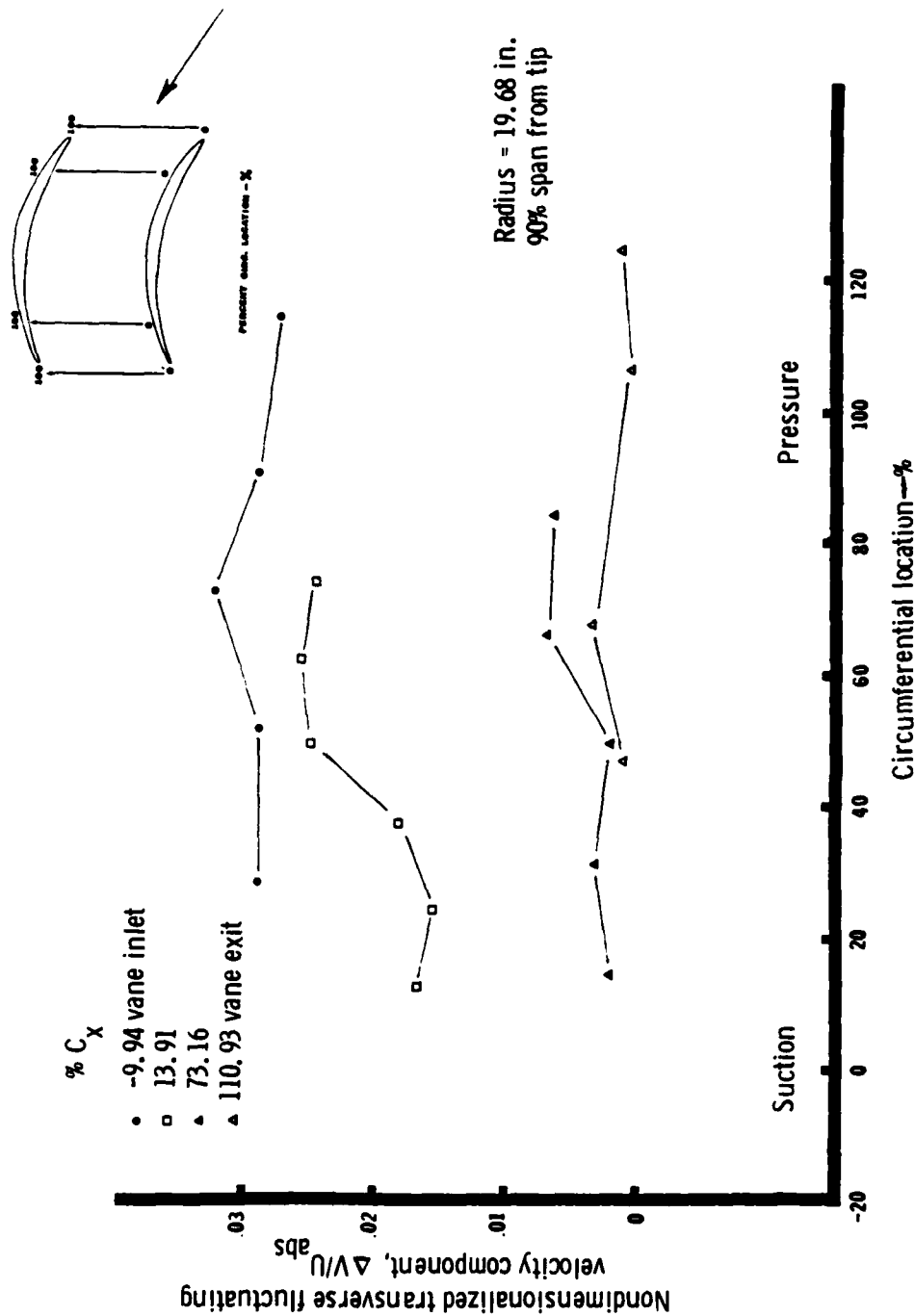
Figure 46. Circumferential and axial variation of transverse fluctuating velocity components at 19.68-in. radius for data point 3.

TE81-7082

82

Radius = 23.76 in.
5% span from tip

PERCENT AXIAL LOCATION - %

Pressure

TE81-7083

120

100

80

60

40

20

0

-20

Circumferential location—%

Suction

% C_x
- -11.29 vane inlet
□ 12.73
▲ 74.13
△ 112.94 vane exit

.03

.02

.01

0

Nondimensionalized streamwise fluctuating
velocity component, $\Delta U/U_{abs}$
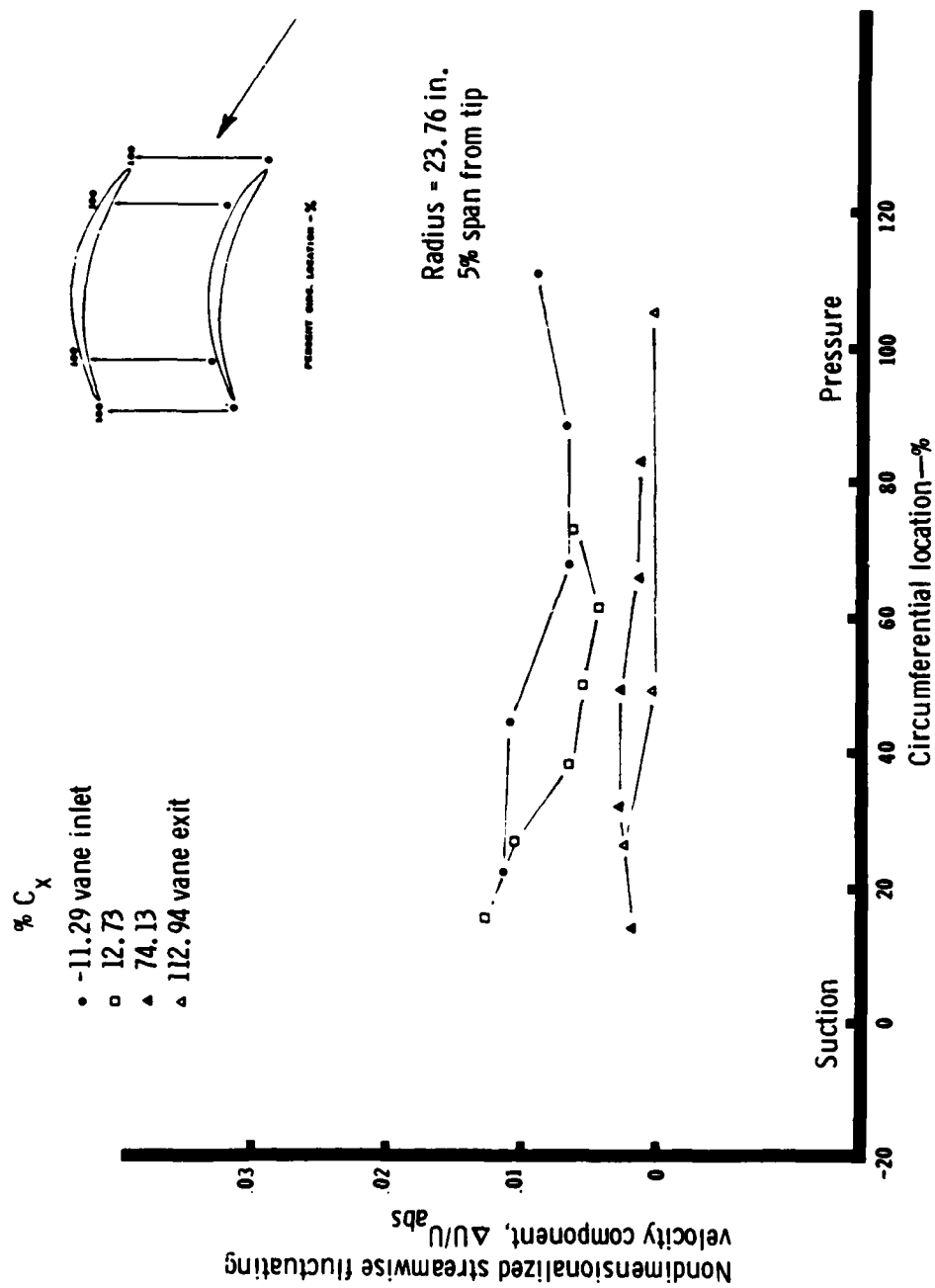
Figure 47. Circumferential and axial variation of streamwise fluctuating
velocity components at 23.76-in. radius for data point 3.
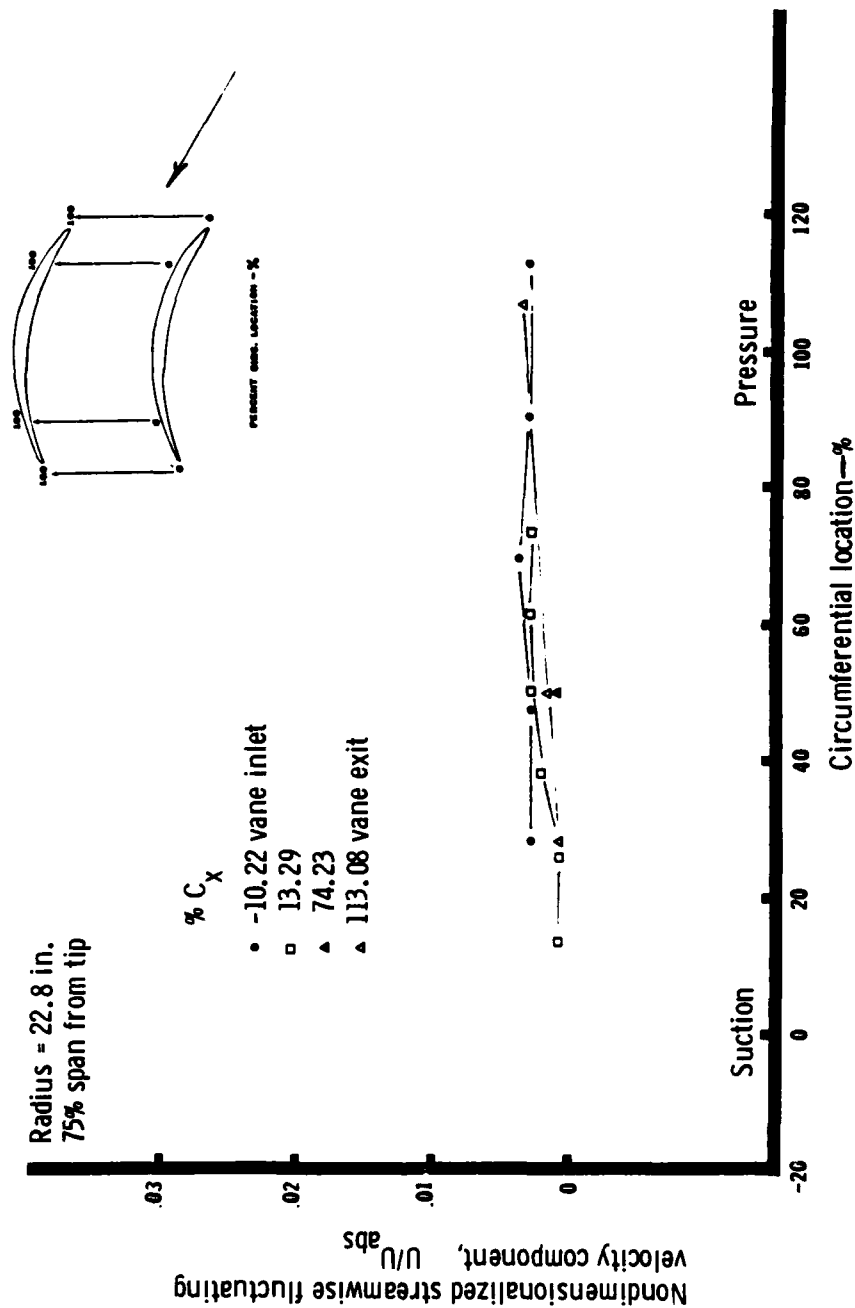
Figure 48. Circumferential and axial variation of streamwise fluctuating velocity components at 22.80-in. radius for data point 3.
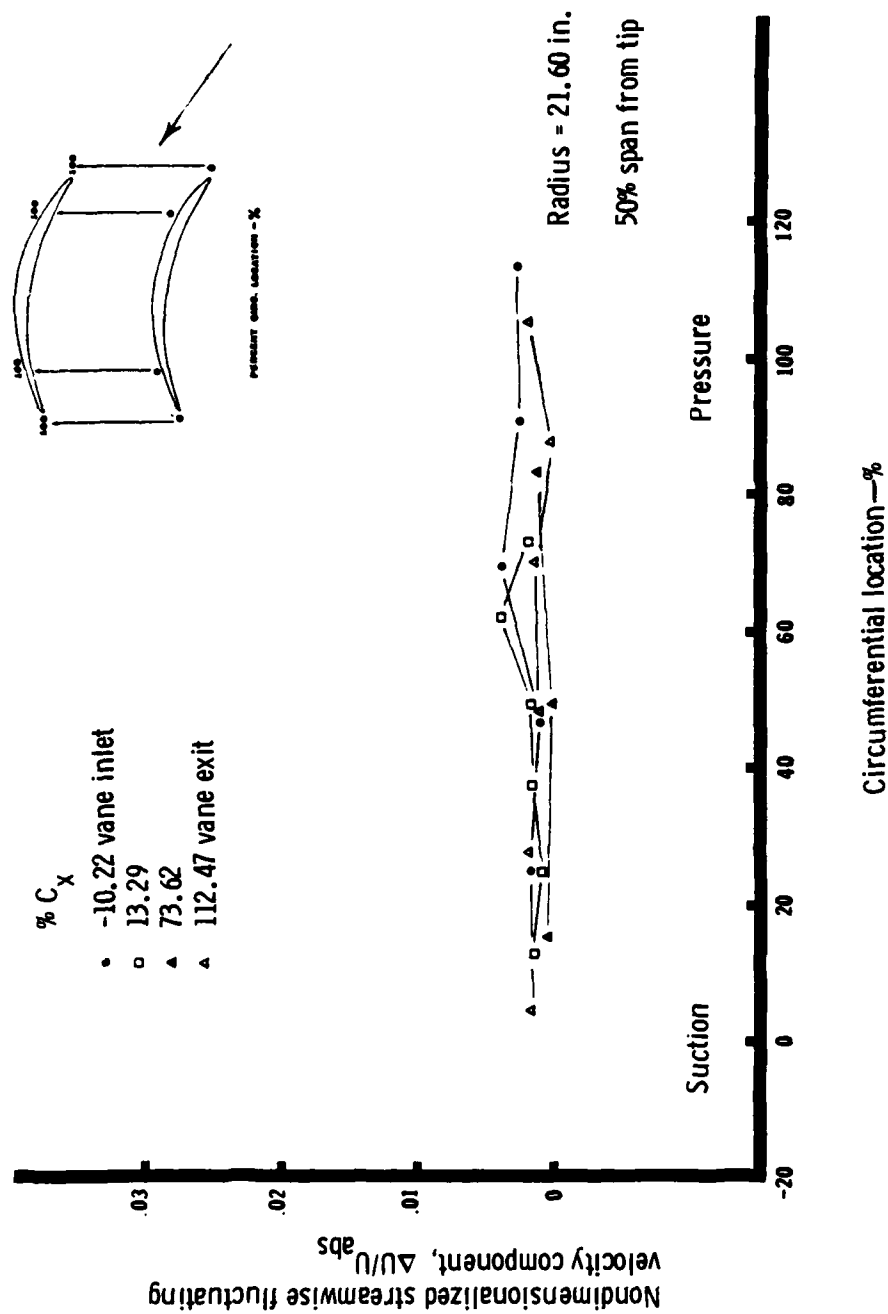
TE81-7084

Figure 49. Circumferential and axial variation of streamwise fluctuating velocity components at 21.60-in. radius for data point 3.

TE81-7085
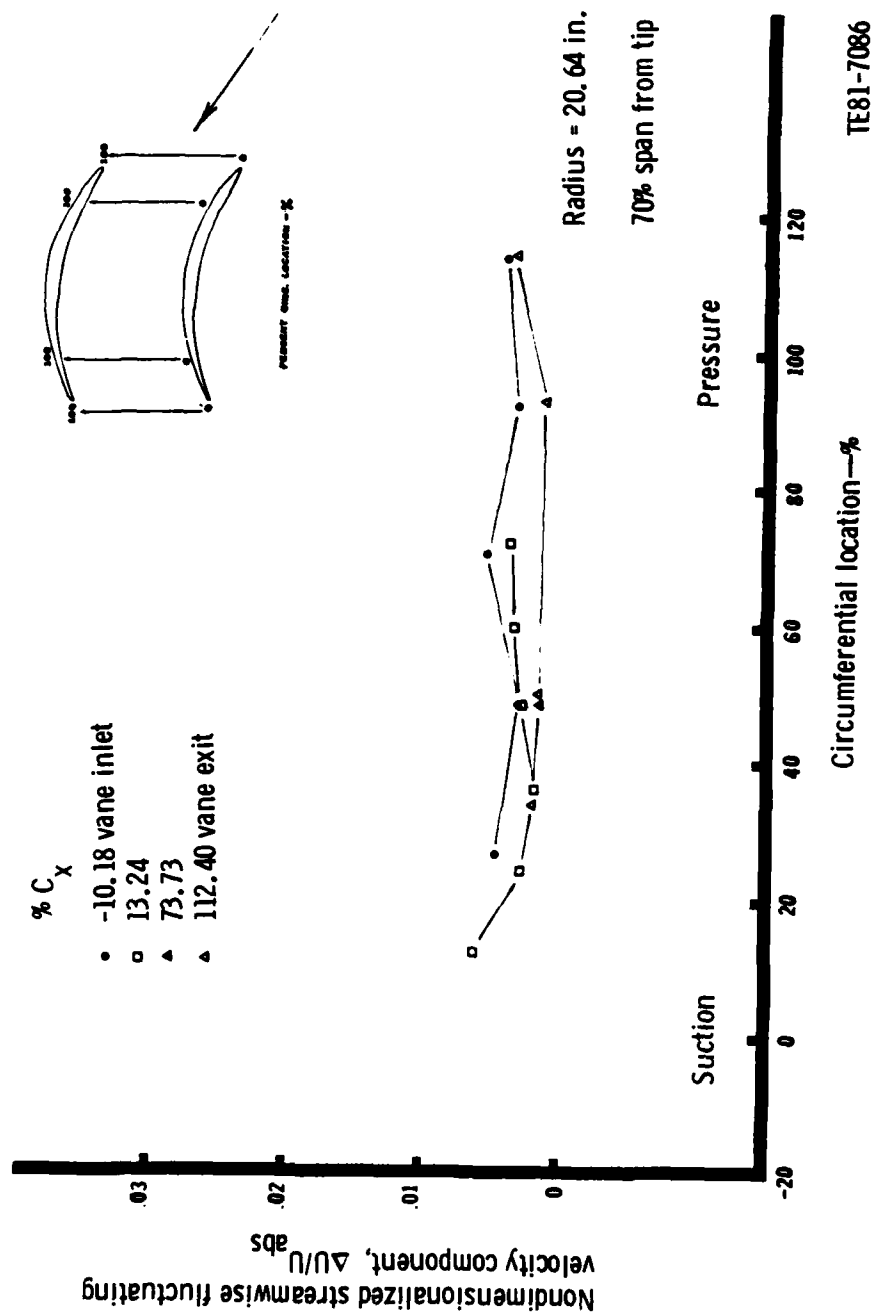
Figure 50. Circumferential and axial variation of streamwise fluctuating velocity components at 20.64-in. radius for data point 3.
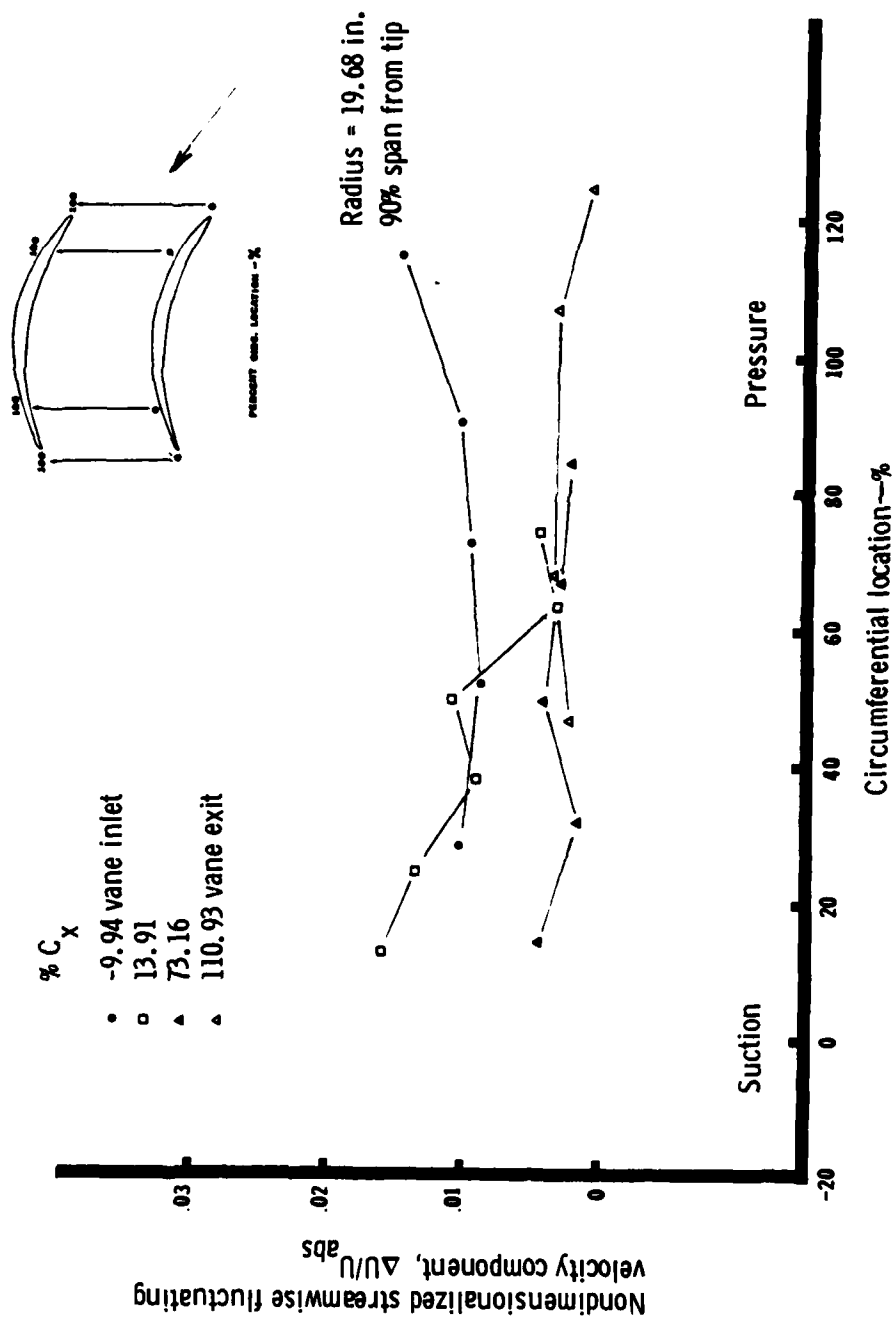
Figure 51. Circumferential and axial variation of streamwise fluctuating velocity components at 19.68-in. radius for data point 3.

TE81-7087

87
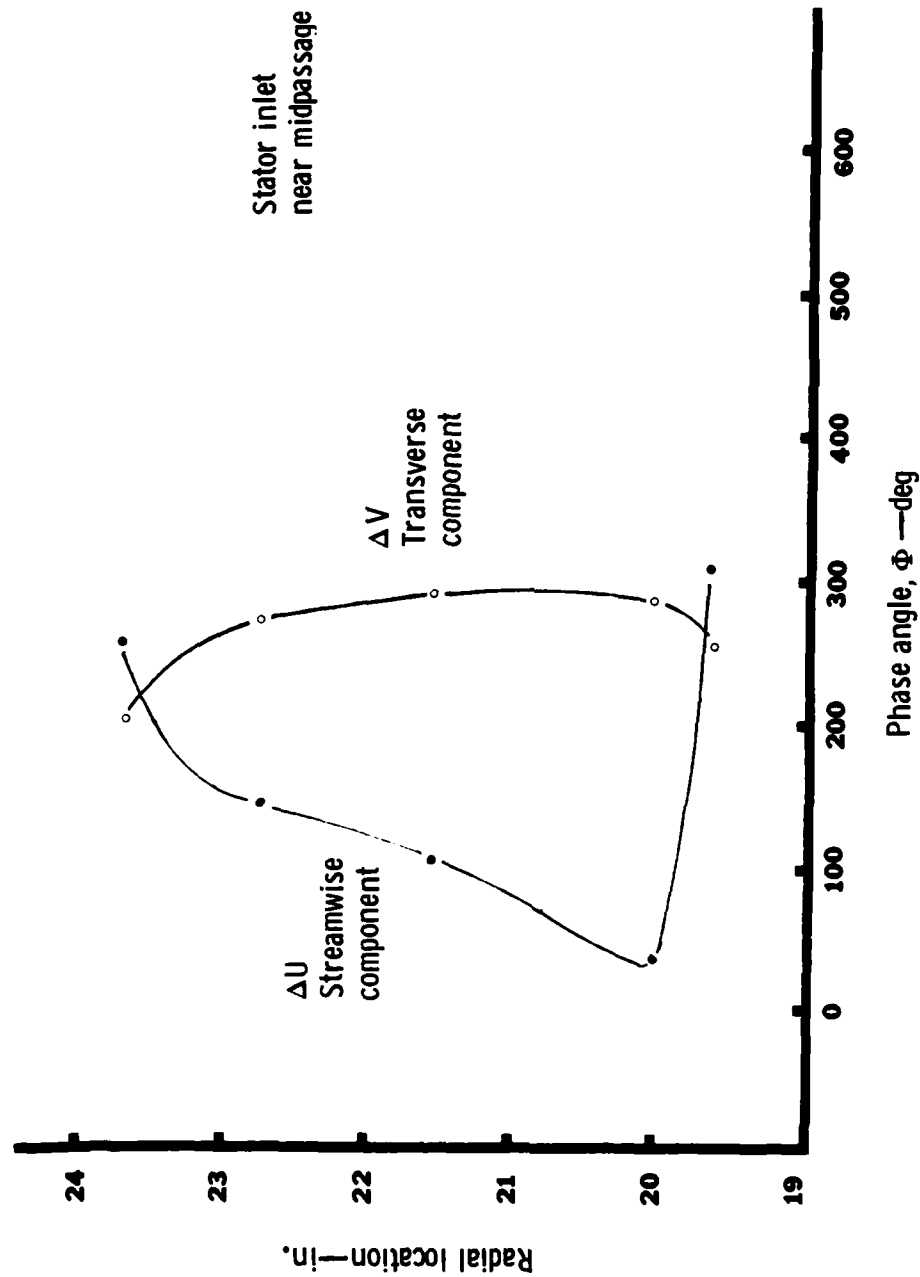
Figure 52. Radial variation of streamwise and transverse fluctuating velocity component phase angles at inlet to stator for data point 3.

88

Figures 53, 54, and 55 present near-tip, midspan, and near-hub circumferential variation of the phase angle of ΔU and ΔV at the inlet station and first survey plane inside the vane passage. It can be seen that the slope of the phase angle versus circumferential location is nearly constant as a function of radius, and that the phase angle varies a full 360 deg from one passage to the next. It can also be seen that $\Phi_{\Delta U}$ and $\Phi_{\Delta V}$ are nearly in phase at the near-hub and near-tip sections and very much out of phase in the midspan region.

One final comment concerning the phase angle relationships noted in Figures 53, 54, and 55 is in order at this point. In the circumferential coordinate, if one considers the distance traveled across the passage and phase angle as the time required to travel that distance, the slope of the $\Phi-\Theta$ curves is related to wheel speed at each respective radial location. The curves of Figures 53, 54, and 55 satisfy these conditions.

Hot Wire Signal Photographic Description of Flow Field

At each radial, circumferential, and axial location in the flow field where hot wire wake measurements were performed, a photograph of the corresponding oscilloscope trace was also recorded. The hot wire output signal was put into the oscilloscope so that both wire signals could be viewed simultaneously. Figures 56 through 59 present an array of hot wire wake signals obtained at various radial and circumferential positions at the four axial locations of vane inlet, fore intervane survey plane, aft intervane survey plane, and vane exit. The upper trace of each photo generally represents the ΔV component. Similarly, the lower trace generally represents the variation of the ΔU fluctuating component.

The photos of Figures 56 through 59 are generally arranged with three photos at the tip (5% span) section and three photos at the hub (90% span) section showing the circumferential variation of the ΔU and ΔV signals. Also shown on each figure, midway through the circumferential direction (50% Θ), are the midspan (50% span) ΔU and ΔV signal characteristics. In this manner, a fairly representative radial and circumferential variation of the fluctuating component signals is presented for each specific axial plane surveyed.
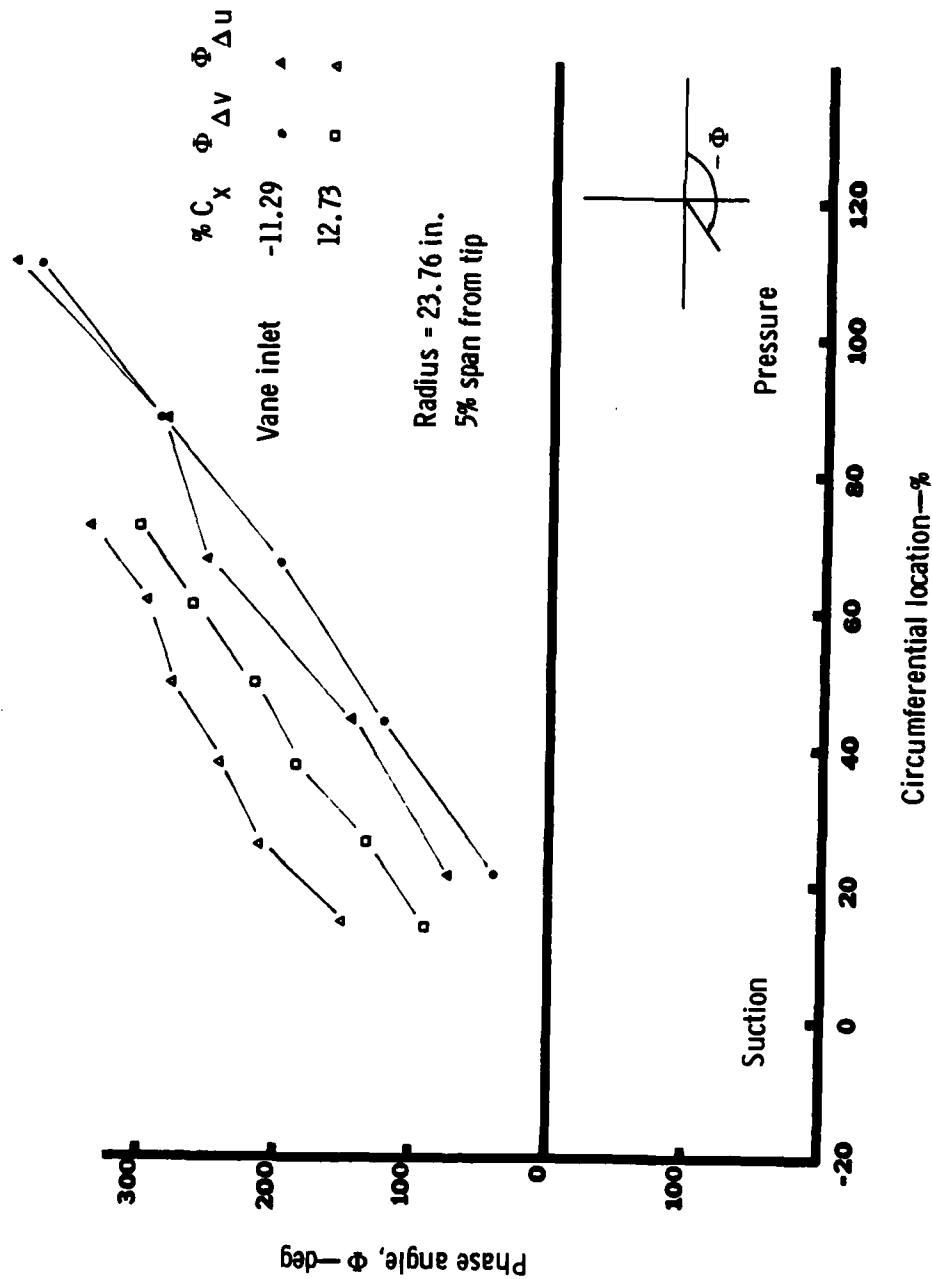
Figure 53. Circumferential variation of streamwise and transverse fluctuating velocity component phase angles at 23.76-in. radius for data point 3.
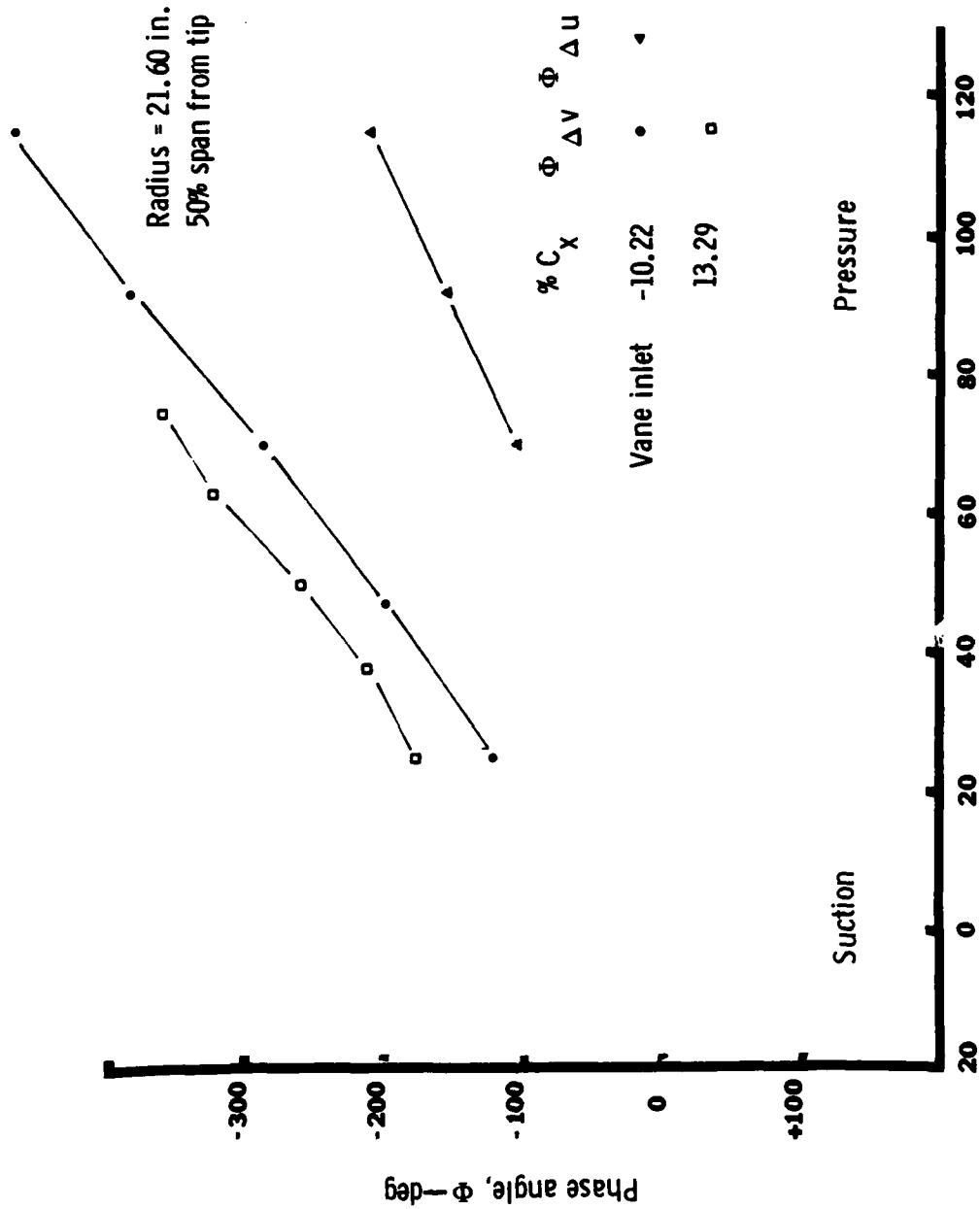
TE81-7089

Figure 54. Circumferential variation of streamwise and transverse fluctuating velocity component phase angle at 21.60-in. radius for data point 3.
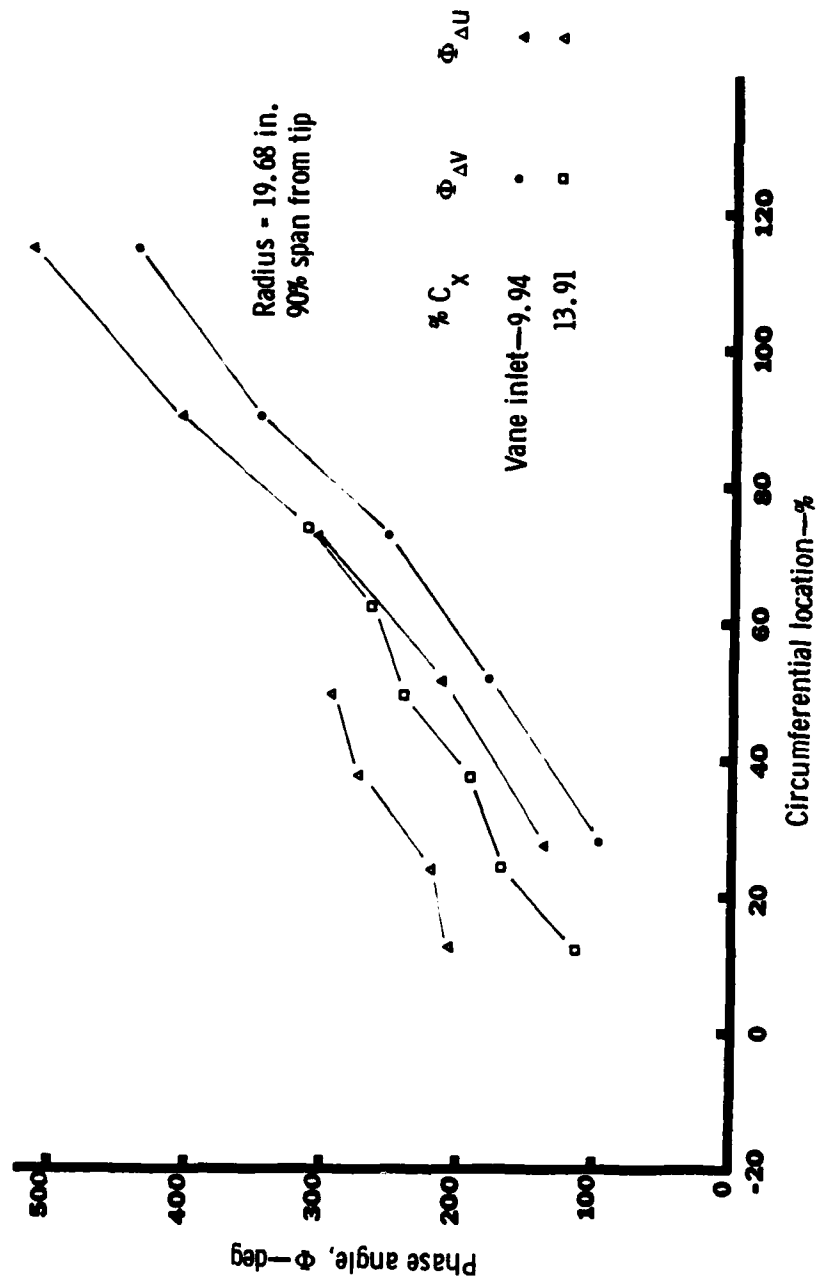
Figure 55. Circumf :ential variation of streamwise and transverse fluctuating velocity component phase angle at 19.68-in. radius for data point 3.

TE81-7091
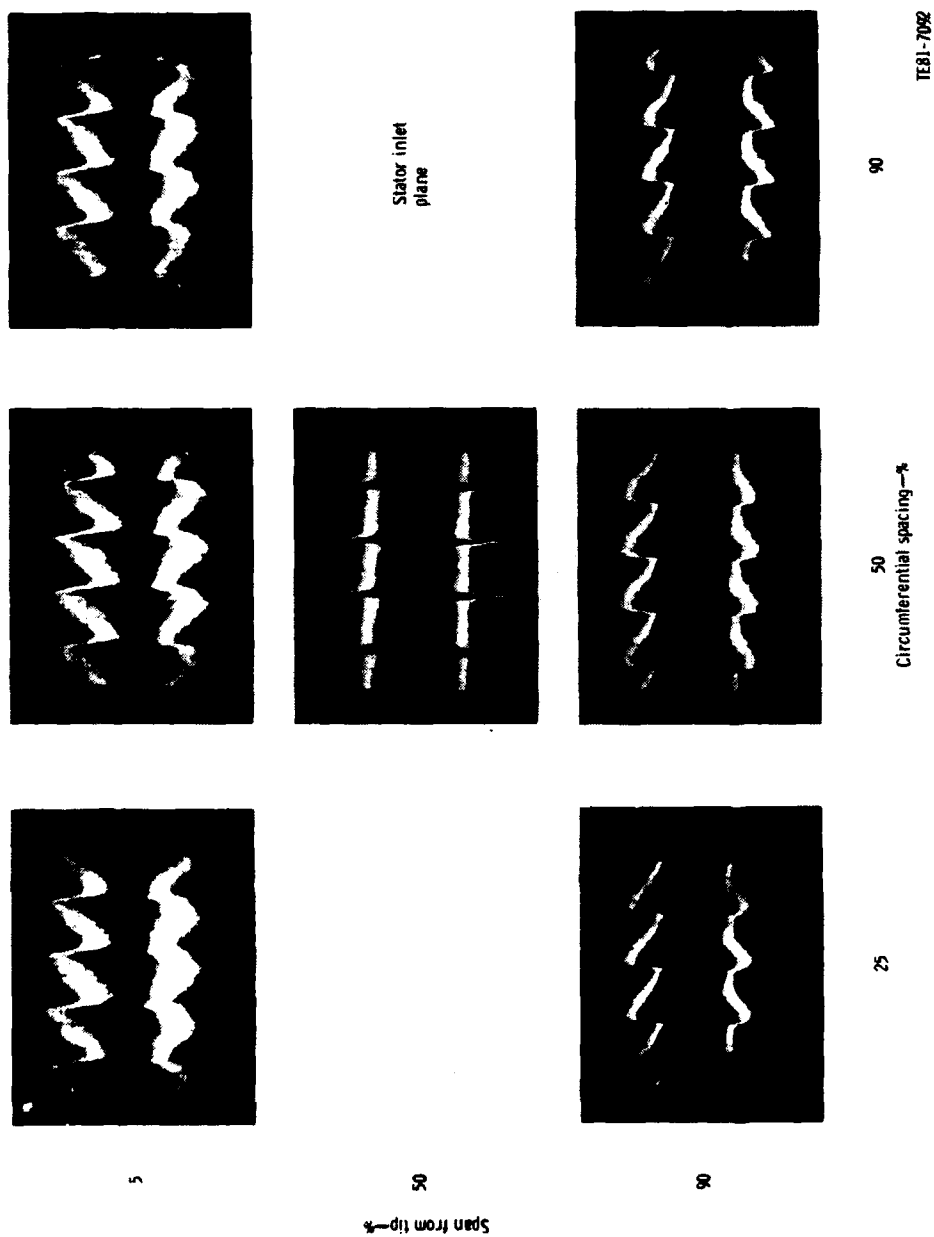
Figure 56. Radial- and circumferential-position hot wire anemometer oscilloscope traces at the vane inlet station. Compressor operating at near-design conditions.

93
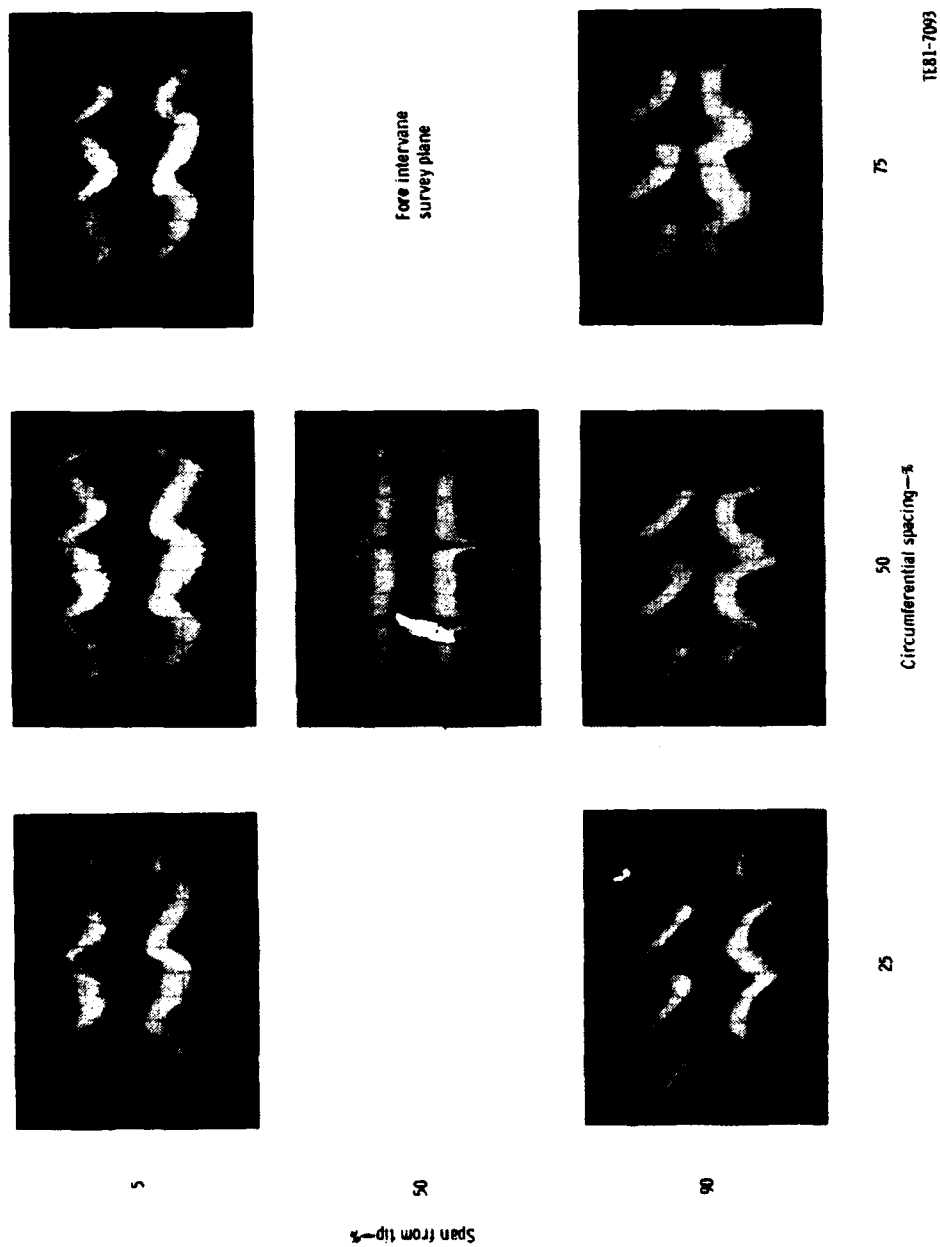
Figure 57. Radial- and circumferential-position hot wire anemometer oscilloscope traces at the fore intervane survey plane. Compressor operating at near-design conditions.
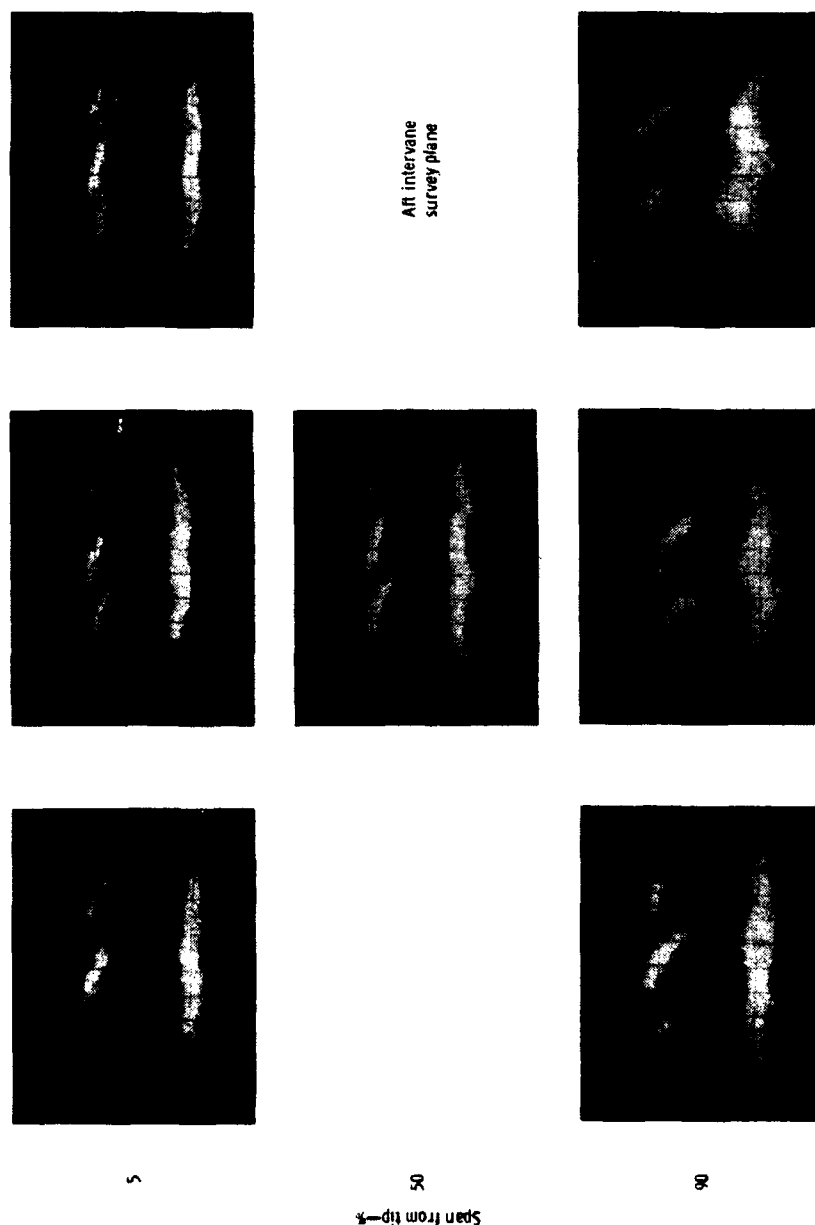
Figure 58. Radial- and circumferential-position hot wire anemometer oscilloscope traces at the aft intervane survey plane. Compressor operating at near-design conditions.

95
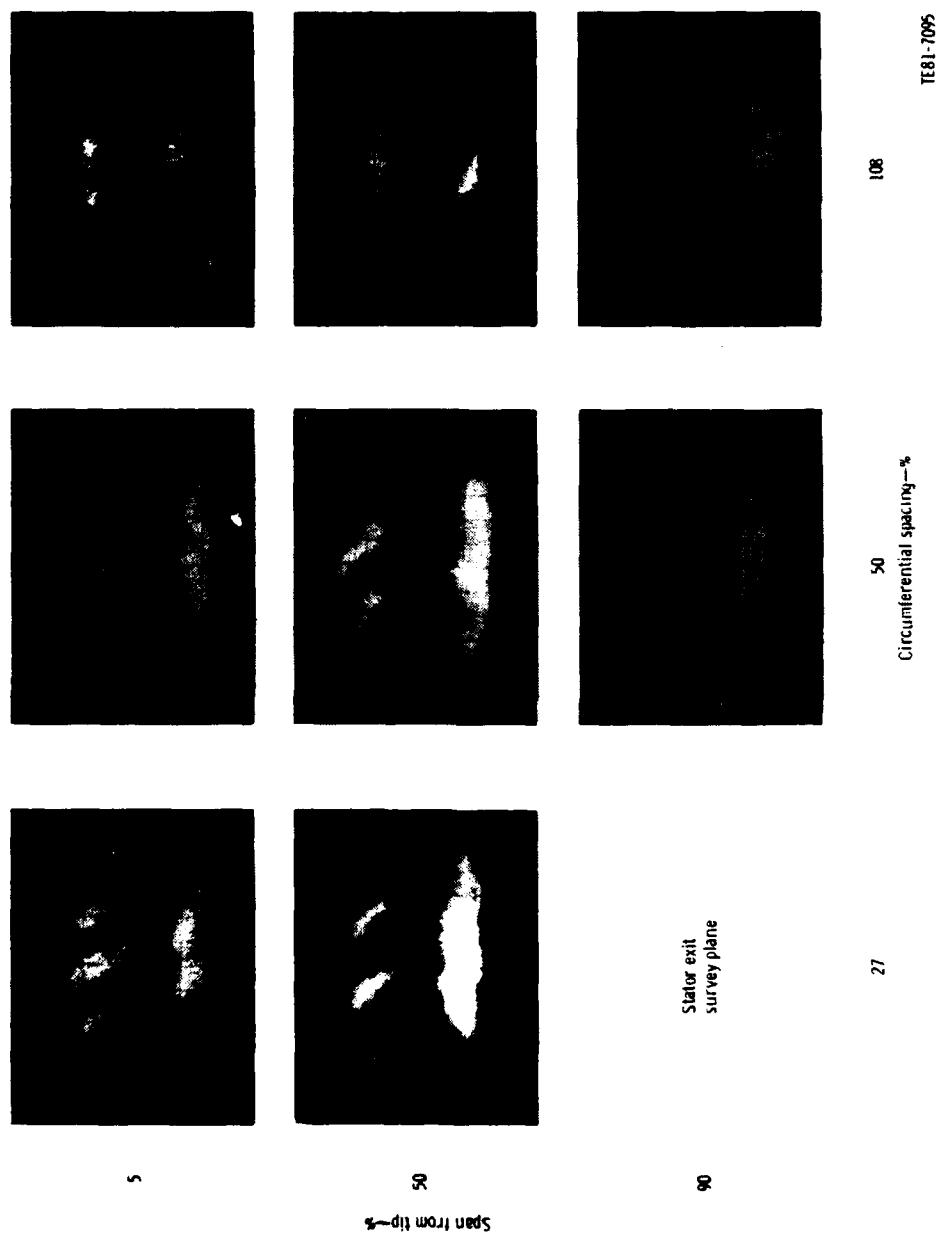
Figure 59. Radial- and circumferential-position hot wire anemometer oscilloscope traces at the stator exit survey place. Compressor operating at near-design conditions.

96

1.0

2.8   2.5

3.2   2.2

3.6

4.0   2.0

1.1

1.8

1.25   1.4   1.6

MICROCOPY RESOLUTION TEST CHART
NATIONAL BUREAU OF STANDARDS 1963 A.

Consider first Figure 56, the radial circumferential survey results obtained at the vane inlet plane. Several observations are immediately apparent. First, the wake at the midspan location is very sharp and well defined, indicating a well-defined blade trailing edge with very little flow separation in the blade trailing edge region. Second, as the hub (90% span) is approached, the signals become broader and less well defined, demonstrating increased strength. This condition is due to the viscous endwall boundary layer flow developing inside the blade passage on the rotating hub wall. Finally, near the tip (5% span), a completely different signal response was recorded. The tip clearance for this build was very large (3% of blade span). Based on past experience with much smaller tip clearances (down to 0.6% span) and the behavior of the tip section signals as they proceed downstream, it is felt that the signal characteristics observed near the tip endwall are due entirely to the large blade tip clearance circumferential flow. Specifically, the highly loaded tip section, with the attendant large pressure-to-suction side pressure gradient in the circumferential direction, results in a significant amount of flow through the large blade tip clearance. This clearance flow spreads circumferentially, resulting in a much larger blade wake in the tip region.

As the flow proceeds downstream, an interesting transformation occurs. It can be seen from Figures 57 and 58 that the quality of the signal decreases substantially as both ΔU and ΔV components are damped out. However, the character of the hub region signal observed at the vane inlet is still evident (though somewhat smeared) at the vane trailing edge. This is not true, however, of the tip region, as the character of the tip section signal observed at the vane inlet station is transformed to the type of signal that existed at the vane inlet hub section. In other words, the tip clearance effects on the signal at the vane inlet are completely eliminated by the time the flow arrives at the vane exit. It is the viscous effects on the stator tip endwall boundary layer that bring about this transformation and damp out ΔU and ΔV fluctuating components.

97

Summary

o Very large (20%-30%) transverse fluctuating components were generated in
  the hub and tip region of the rotor blade row. These fluctuations were
  the result of (1) endwall boundary layer development in the rotor hub re-
  gion and (2) pressure-to-suction-surface clearance flows through the large
  (3% span) clearance in the blade tip region.

o Both ΔV and ΔV fluctuating components were damped out to about 1% of inlet
  velocity level by the time the flow reached the vane trailing edge.

o In general, the fluctuating components were in phase with each other near
  the endwalls, but 180 deg out of phase in the midspan region.

o A photographic description of the hot wire wake signals showed clean,
  well-defined wakes in the midspan region at the vane inlet. All wake sig-
  nals were heavily damped as the flow moved through the stator passage. In
  the endwall regions, the wakes were much less well defined. They were
  dominated by viscous boundary layer flow in the hub region of the stator
  passage. However, in the tip region, the wake character, which was ini-
  tially dictated by clearance flow effects, was eventually controlled by
  the viscous stator tip endwall boundary layer flow.

V. CONCLUSIONS

Steady-state fluctuating static pressure and hot wire wake measurements have been performed on the DDA single-stage low-speed compressor operating over a range of flow, speeds, and pressure ratios. Based on analysis of the experimental results, the following conclusions are drawn:

o The flow field is strongly three-dimensional with large transverse and streamwise fluctuating components generated by the rotor blades.

o In the rotor hub region, the wake pattern is dominated by the buildup and subsequent shedding of the rotor hub/endwall boundary layer.

o In the tip region, the wake pattern at stator inlet is controlled by the tangential flow through the large (3% span) blade tip end clearance.

o At the hub and tip, respectively, the transverse fluctuating components are 20%-30% of the inlet freestream velocity level. In the midspan region, these fluctuations were reduced to about 10% of the inlet freestream velocity.

o All streamwise and transverse fluctuating components were damped to about 1% of inlet free-stream velocity by the time the flow reached the stator exit plane.

o These fluctuating velocity components induce time-dependent variations of static pressure on the suction and pressure surfaces of stators positioned downstream of the unsteady flow generating rotor.

o Two variables have been identified which appear to describe the response of the vane surface pressures to the upstream streamwise and transverse fluctuating velocity components. Those variables are the local stator incidence angle and the normalized transverse fluctuating velocity component.

o Existing analytical methods do not satisfactorily model the induced pressure amplitude or phase relationships.

99

VI. RECOMMENDATIONS

It has been shown that very large streamwise and transverse fluctuating velocity components exist in the hub and tip regions immediately downstream of the DDA low-speed compressor. It is further stated that these components were generated within the rotor system. In the hub region, the large fluctuations were due to the development of rotor hub endwall viscous, secondary flow, whereas in the tip region, the large fluctuations were the result of tangential clearance flow in the large blade tip clearance gap.

It is recommended that a follow-on program be initiated that would result in the generation of significantly reduced fluctuating velocity components in the vane inlet hub and tip regions. This would be accomplished by redesigning the low-speed compressor rotor blade. The redesign would feature airfoil contours in the tip region very similar to what has been employed in the rotor for this present program, i.e. BU18, except that much smaller (0.5% span) clearances would be allowed. The major redesign effort would come about in the lower half of the rotor airfoil, where the camber would be reduced to eliminate the large overturning and overpressuring that exist with the existing airfoil design.

The experimental program would be similar to this program, and the end result would be to show that improved rotor design leads to reduced fluctuating velocity components and reduced vane response to those fluctuating velocities. The application of these research findings could lead to improved understanding of vane response to induced vibrations and would contribute to preventing engine vane structural failures.

APPENDIX

The surface pressures measured during the 100% corrected speed investigation
are tabulated here. The first set of tabulations involve amplitude and phase
angle of the basic pressure signals. The second set of tabulations present
the same data normalized on the term ρU_{abs}^2.

MEASURED PRESSURES

Rotor speed = 100%   Data point 1

Kulite location	Pressure difference (pressure--suction) (psia)	Resultant phase--deg
1		
2	0.00275	-109.33
3	0.00658	-135.71
4		
5	0.00424	-171.51
6	0.00177	-164.64
7	0.00117	-33.07
8	0.00328	-118.77
9	0.00426	-122.91
10	0.00406	-169.60
11	0.00272	-148.54
12	0.07944	-122.09
13	0.01887	-196.25
14	0.00576	-128.46
15	0.00255	-32.75
16	0.00534	-120.35
17	0.06016	-197.71
18	0.00452	-195.82
19	0.04126	-202.52
20	0.04998	-157.53
21	0.00684	-142.95
22	0.05578	-111.36
23	0.01235	-101.92
24	0.00366	-269.89
25	0.00356	-257.17
26	0.00357	-125.79

Rotor speed = 100%   Data point 1

Kulite location	Pressure surface		Suction surface	
	Amplitude (psia)	Phase (deg)	Amplitude (psia)	Phase (deg)
1				
2	0.00657	345.70	0.00734	7.64
3	0.00331	206.30	0.00358	60.85
4				
5	0.00050	199.31	0.00374	7.04
6	0.00081	188.28	0.00097	21.29
7	0.00121	333.80	0.00015	46.98
8	0.00176	278.94	0.00217	31.46
9	0.00177	321.12	0.00444	33.75
10	0.00137	290.09	0.00450	352.90
11	0.00291	242.03	0.00150	309.70
12	0.00835	226.00	0.07129	59.29
13	0.00695	228.40	0.01709	322.19
14	0.00065	286.23	0.00541	45.89
15	0.00034	312.60	0.00222	149.50
16	0.00331	308.04	0.00514	22.89
17	0.04371	147.79	0.02094	13.80
18	0.00245	361.50	0.00689	350.25
19	0.03163	142.54	0.01345	14.78
20	0.03747	183.89	0.01875	62.01
21	0.00280	354.64	0.00911	25.08
22	0.02013	256.07	0.03591	64.49
23	0.01044	246.37	0.00300	123.05
24	0.00295	40.87	0.00283	322.33
25	0.00205	120.60	0.00172	261.53
26	0.00277	356.39	0.00556	29.29

Rotor speed = 100%   Data point 2

Kulite location	Pressure difference (pressure--suction) (psia)	Resultant phase--deg
1		
2	0.00678	-186.99
3	0.00643	-122.68
4		
5	0.00327	-208.23
6	0.00136	-159.28
7	0.00041	-87.82
8	0.00218	-117.68
9	0.00329	-158.85
10	0.00324	-148.42
11	0.00571	-145.46
12	0.05060	-139.35
13	0.01239	-182.82
14	0.00701	-147.19
15	0.00193	-145.91
16	0.00435	-168.48
17	0.03200	-182.70
18	0.00521	-207.07
19	0.02146	-195.88
20	0.03483	-149.37
21	0.00694	-217.91
22	0.06793	-121.27
23	0.01845	-127.62
24	0.00158	-126.26
25	0.00302	-51.35
26	0.00533	-275.01

Rotor speed = 100%   Data point 2

Kulite location	Pressure surface		Suction surface	
	Amplitude (psia)	Phase (deg)	Amplitude (psia)	Phase (deg)
1				
2	0.00174	149.55	0.00522	0.64
3	0.00291	233.70	0.00354	60.30
4				
5	0.00229	197.80	0.00235	287.26
6	0.00290	224.20	0.00174	242.40
7	0.00291	241.50	0.00256	236.80
8	0.00295	252.68	0.00089	278.40
9	0.00641	203.50	0.00313	205.97
10	0.00813	205.32	0.00492	201.20
11	0.00339	197.10	0.00268	56.80
12	0.01132	241.90	0.04025	34.80
13	0.00313	226.00	0.01060	344.33
14	0.00115	98.60	0.00756	40.80
15	0.00155	22.90	0.00346	29.10
16	0.00048	52.85	0.00472	15.40
17	0.01656	167.19	0.01596	7.80
18	0.00260	178.80	0.00309	311.44
19	0.01163	126.22	0.01421	14.30
20	0.01083	203.10	0.02413	34.00
21	0.00105	189.30	0.00627	315.00
22	0.02873	242.60	0.03931	55.90
23	0.01386	217.10	0.00626	88.10
24	0.00258	340.00	0.00338	6.70
25	0.00021	248.10	0.00292	132.20
26	0.00219	319.50	0.00684	280.10

Rotor speed = 100%   Data point 3

Kulite location	Pressure difference (pressure--suction) (psia)	Resultant phase--deg
1		
2	0.01320	-189.63
3	0.00859	-156.41
4		
5	0.00521	-191.15
6	0.00185	-240.24
7	0.00314	-119.06
8	0.00486	-169.94
9	0.00390	-169.02
10	0.00759	-186.74
11	0.00862	-175.27
12	0.06110	-148.22
13	0.02369	-173.46
14	0.00589	-173.93
15	0.00210	-204.67
16	0.00097	-197.95
17	0.03391	-196.14
18	0.00295	-298.49
19	0.02908	-216.39
20	0.06179	-208.60
21	0.00167	-195.03
22	0.12714	-169.32
23	0.03547	-155.48
24	0.00592	-132.26
25	0.00203	-320.88
26	0.00522	-172.36

Rotor speed = 100%   Data point 3

Kulite location	Pressure surface		Suction surface	
	Amplitude (psia)	Phase (deg)	Amplitude (psia)	Phase (deg)
1				
2	0.00962	187.20	0.00487	315.50
3	0.00752	164.60	0.00547	83.50
4				
5	0.00445	191.00	0.00200	291.80
6	0.00363	185.90	0.00335	216.30
7	0.00225	214.30	0.00151	103.00
8	0.00308	200.80	0.00192	352.70
9	0.00281	185.30	0.00114	25.13
10	0.00500	185.40	0.00290	332.00
11	0.00357	187.60	0.00506	2.70
12	0.02353	200.30	0.03833	38.80
13	0.01096	165.40	0.01404	22.90
14	0.00265	131.80	0.00485	32.40
15	0.00231	123.30	0.00123	58.63
16	0.00314	88.30	0.00302	70.30
17	0.01706	147.23	0.01823	359.40
18	0.00218	95.20	0.00166	194.80
19	0.01440	146.70	0.01473	320.60
20	0.02149	162.70	0.04093	325.50
21	0.00258	124.50	0.00170	84.90
22	0.04222	211.90	0.08910	0.80
23	0.03398	176.30	0.01699	95.50
24	0.00836	179.20	0.00628	134.20
25	0.00254	65.90	0.00117	117.20
26	0.00488	176.70	0.00102	72.90

Rotor speed = 100%, Data point 4

Kulite location	Pressure difference (pressure--suction) (psia)	Resultant phase--deg
1		
2	0.01374	-197.50
3	0.00955	-160.65
4		
5	0.00424	-124.43
6	0.00116	-223.81
7	0.00229	-163.84
8	0.00285	-188.81
9	0.00453	-179.50
10	0.00897	-174.95
11	0.00762	-178.46
12	0.08598	-185.70
13	0.01670	-152.59
14	0.00500	-191.28
15	0.00093	-110.91
16	0.00509	-83.28
17	0.04608	-169.91
18	0.00213	-298.09
19	0.01965	-215.04
20	0.11524	-220.44
21	0.00200	-258.91
22	0.11269	-172.82
23	0.03056	-149.30
24	0.00469	-165.73
25	0.00181	-152.96
26	0.00628	-231.68

Rotor speed = 100%   Data point 4

Kulite location	Pressure surface		Suction surface	
	Amplitude (psia)	Phase (deg)	Amplitude (psia)	Phase (deg)
1				
2	0.01064	165.70	0.00317	331.70
3	0.00522	136.00	0.00859	52.30
4				
5	0.00420	242.20	0.00049	333.20
6	0.00340	135.80	0.00224	135.60
7	0.00558	174.50	0.00355	160.70
8	0.00526	168.90	0.00242	166.20
9	0.00284	153.20	0.00239	33.40
10	0.00483	165.20	0.00472	25.40
11	0.00321	184.20	0.00441	359.60
12	0.01796	170.50	0.06807	355.30
13	0.00919	161.10	0.01230	60.10
14	0.00490	148.65	0.00173	65.30
15	0.00299	118.60	0.00366	107.50
16	0.00335	129.40	0.00811	109.60
17	0.02175	173.80	0.02593	23.70
18	0.00425	87.10	0.00249	108.50
19	0.01246	138.60	0.00740	335.70
20	0.01559	161.90	0.10099	316.20
21	0.00333	98.20	0.00134	93.90
22	0.04147	206.10	0.07468	356.80
23	0.03322	182.10	0.01596	115.70
24	0.00886	179.48	0.00449	164.00
25	0.00258	183.40	0.00117	145.20
26	0.00697	119.60	0.00122	68.30

NORMALIZED PRESSURES

Rotor speed = 100%   Data point 1

Kulite location	Pressure difference (pressure--suction) (norm)	Resultant phase--deg
1		
2	0.28282	-201.53
3	0.67589	-227.91
4		
5	0.43545	-263.71
6	0.18200	-256.84
7	0.12073	-125.27
8	0.33721	-210.97
9	0.43740	-215.11
10	0.41702	-261.80
11	0.27976	-240.74
12	1.34415	-311.89
13	0.31931	-26.05
14	0.09744	-318.26
15	0.04307	-222.55
16	0.09038	-310.15
17	4.62783	-336.01
18	0.34761	-334.12
19	4.23920	-294.72
20	2.56825	-272.85
21	0.35163	-258.27
22	0.63812	-248.05
23	0.14128	-238.61
24	0.04183	-46.58
25	0.04073	-33.86
26	0.04084	-262.48

Rotor speed = 100%   Data point 1

Kulite location	Pressure surface		Suction surface	
	Amplitude (norm)	Phase (deg)	Amplitude (norm)	Phase (deg)
1				
2	0.67458	253.50	0.75401	-84.56
3	0.33970	114.10	0.36806	-31.35
4				
5	0.05179	107.11	0.38471	-85.16
6	0.08358	96.08	0.09959	-70.91
7	0.12423	241.60	0.01509	-45.22
8	0.18126	186.74	0.22328	-60.74
9	0.18157	228.92	0.45582	-58.45
10	0.14098	197.89	0.46214	260.70
11	0.29932	149.83	0.15382	217.50
12	0.14129	36.20	1.20626	-130.51
13	0.11761	38.60	0.28919	132.39
14	0.01105	96.43	0.09150	-143.91
15	0.00581	122.80	0.03748	-40.30
16	0.05604	118.24	0.08706	-166.91
17	3.36192	9.49	1.61046	-124.50
18	0.18826	223.20	0.53031	211.95
19	3.24968	50.34	1.38204	-77.42
20	1.92557	68.57	0.96351	-53.31
21	0.14388	239.32	0.46804	-90.24
22	0.23032	119.38	0.41081	-72.20
23	0.11949	109.68	0.03431	-13.64
24	0.03374	-95.82	0.03233	185.64
25	0.02348	-16.09	0.01972	124.84
26	0.03168	219.70	0.06364	-107.40

Rotor speed = 100%   Data point 2

Kulite location	Pressure difference (pressure--suction) (norm)	Resultant phase--deg
1		
2	0.73421	-309.89
3	0.69701	-245.57
4		
5	0.35374	-331.13
6	0.14777	-282.18
7	0.04454	-210.72
8	0.23655	-240.58
9	0.35652	-281.75
10	0.35130	-271.32
11	0.61881	-268.36
12	0.78200	-328.45
13	0.19152	-11.92
14	0.10839	-336.29
15	0.02977	-335.01
16	0.06720	-357.58
17	2.03850	-289.60
18	0.33209	-313.97
19	2.32549	-318.78
20	1.13292	-258.87
21	0.22569	-327.41
22	0.54017	-246.47
23	0.14673	-252.82
24	0.01258	-251.46
25	0.02401	-176.55
26	0.04240	-40.21

Rotor speed = 100%   Data point 2

Kulite location	Pressure surface		Suction surface	
	Amplitude (norm)	Phase (deg)	Amplitude (norm)	Phase (deg)
1				
2	0.18873	26.65	0.56609	-122.26
3	0.31473	110.80	0.38342	-62.60
4				
5	0.24800	74.90	0.25460	164.36
6	0.31462	101.30	0.18852	119.50
7	0.31473	118.60	0.27736	113.90
8	0.32004	129.70	0.09696	155.50
9	0.69447	80.60	0.33857	83.07
10	0.88072	82.42	0.53288	78.30
11	0.36696	74.20	0.29036	-66.10
12	0.17496	52.80	0.62218	-154.30
13	0.04840	36.90	0.16376	155.23
14	0.01781	-90.50	0.11683	-148.30
15	0.02397	-166.20	0.05349	-160.00
16	0.00748	-136.25	0.07298	-173.70
17	1.05509	60.29	1.01682	-99.10
18	0.16535	71.90	0.19701	204.54
19	1.26002	3.32	1.53998	-108.60
20	0.35247	93.60	0.78484	-75.50
21	0.03432	79.80	0.20394	205.50
22	0.22850	117.40	0.31257	-69.30
23	0.11022	91.90	0.04977	-37.10
24	0.02049	214.80	0.02687	-118.50
25	0.00165	122.90	0.02324	7.00
26	0.01742	194.30	0.05439	154.90

Rotor speed = 100%   Data point 3

Kulite location	Pressure difference (pressure--suction) (norm)	Resultant phase--deg
1		
2	0.54069	-264.43
3	0.35161	-231.21
4		
5	0.21340	-265.95
6	0.07582	-315.04
7	0.12838	-193.86
8	0.19886	-244.74
9	0.15989	-243.82
10	0.31076	-261.54
11	0.35284	-250.07
12	0.92854	-307.72
13	0.36000	-332.96
14	0.08951	-333.43
15	0.03194	-4.17
16	0.01475	-357.45
17	1.44282	-282.24
18	0.12555	-24.59
19	1.19102	-291.19
20	0.87516	-280.10
21	0.02365	-266.53
22	0.83206	-275.12
23	0.23216	-261.28
24	0.03875	-238.06
25	0.01326	-66.68
26	0.03415	-278.16

Rotor speed = 100%   Data point 3

Kulite location	Pressure surface		Suction surface	
	Amplitude (norm)	Phase (deg)	Amplitude (norm)	Phase (deg)
1				
2	0.39394	112.40	0.19943	240.70
3	0.30794	89.80	0.25393	8.70
4				
5	0.18231	116.20	0.08148	217.00
6	0.14885	111.10	0.13702	141.50
7	0.09230	139.50	0.06179	28.20
8	0.12600	126.00	0.03864	277.90
9	0.11523	110.50	0.04664	-49.67
10	0.20467	110.60	0.11876	257.20
11	0.14611	112.80	0.20704	-72.10
12	0.35754	40.80	0.58252	-120.70
13	0.16653	5.90	0.21331	-136.60
14	0.04024	-27.70	0.07365	-127.10
15	0.03509	-36.20	0.01874	-100.87
16	0.04772	-71.20	0.04584	-89.20
17	0.72596	61.13	0.77557	273.30
18	0.09268	9.10	0.07064	108.70
19	0.58952	71.90	0.60319	245.80
20	0.30439	91.20	0.57975	254.00
21	0.03654	53.00	0.02408	13.40
22	0.27633	106.10	0.58312	-105.00
23	0.22235	70.50	0.11119	-10.30
24	0.05470	73.40	0.04107	28.40
25	0.01663	-39.90	0.00766	11.40
26	0.03194	70.90	0.00668	-32.90

Rotor speed = 100%   Data point 4

Kulite location	Pressure difference (pressure--suction) (norm)	Resultant phase--deg
1		
2	0.28979	-261.40
3	0.20146	-224.55
4		
5	0.08938	-188.33
6	0.02445	-287.71
7	0.04841	-227.74
8	0.06010	-252.71
9	0.09557	-243.40
10	0.18919	-238.85
11	0.16070	-242.36
12	1.91067	-333.00
13	0.37109	-299.89
14	0.11113	-338.58
15	0.02059	-258.21
16	0.11306	-230.58
17	1.30905	-252.21
18	0.06064	-20.39
19	0.41459	-278.94
20	1.57212	-292.54
21	0.02724	-331.01
22	0.86152	-283.52
23	0.23362	-260.00
24	0.03587	-276.43
25	0.03193	-244.41
26	0.02617	-121.50

Rotor speed = 100%   Data point 4

Kulite location	Pressure surface		Suction surface	
	Amplitude (norm)	Phase (deg)	Amplitude (norm)	Phase (deg)
1				
2	0.22447	101.80	0.06686	267.80
3	0.11023	72.10	0.18116	-11.60
4				
5	0.08861	178.30	0.01032	269.30
6	0.07171	71.90	0.04726	71.70
7	0.11772	110.60	0.07489	96.80
8	0.11097	105.00	0.05097	102.30
9	0.05983	89.30	0.05051	-30.50
10	0.10192	101.30	0.09954	-38.50
11	0.06781	120.30	0.09302	295.70
12	0.39911	23.20	1.51267	208.00
13	0.20420	13.80	0.27333	-87.20
14	0.10882	1.35	0.03840	-82.00
15	0.06644	-28.70	0.08133	-39.80
16	0.07438	-17.90	0.18020	-37.70
17	0.61790	91.50	0.73665	-58.60
18	0.12074	4.80	0.07074	26.20
19	0.26287	74.70	0.15608	271.80
20	0.21269	89.80	1.37776	244.10
21	0.04548	26.10	0.01834	21.80
22	0.31705	95.40	0.57095	246.10
23	0.25398	71.40	0.12204	5.00
24	0.06774	68.78	0.03430	53.30
25	0.01970	72.70	0.02204	-26.95
26	0.02268	229.49	0.00518	101.80

LIST OF SYMBOLS

AR	Aspect ratio, c/l
c	True chord, in.
C_x	Axial chord, in.
i	Incidence angle, $(\beta_1 - \beta_m)$, deg
l	Airfoil height, in.
le	Leading edge radius, in.
N	Shaft speed, rpm
$N/\sqrt{\theta}$	Corrected shaft speed, rpm
P_S	Static pressure, psia
P_{T1}	Stage inlet total pressure, psia
P_{T2}	Stage exit total pressure, psia
ΔP	Pressure difference across airfoil, $(P_{sp} - P_{ss})$, psia
R	Radial coordinate, in.
s	Airfoil spacing, in.
T	Total temperature, °R
te	Trailing edge radius, in.
U_{abs}	Stator inlet midpassage freestream absolute velocity, ft/sec
U_t	Blade tip speed, ft/sec
$U_t/\sqrt{\theta}$	Blade corrected tip speed, ft/sec
ΔU	Streamwise fluctuating velocity component, ft/sec
ΔV	Transverse fluctuating velocity component, ft/sec
W	Flow rate, lb/sec
$W\sqrt{\theta}/\delta$	Corrected flowrate, lb/sec
x	Axial coordinate, in.

GREEK SYMBOLS

β_1	Inlet air angle, deg
β_2	Exit air angle, deg
β_{m1}	Inlet metal angle, deg
β_{m2}	Exit metal angle, deg
δ	Ratio of compressor inlet total pressure to absolute pressure at standard sea level conditions

125

Θ	Ratio of compressor inlet total temperature to total temperature at standard sea level conditions
Θ	Circumferential coordinate, deg
ρ	Density, lbm/ft^3
τ	Blade tip end clearance, in.
τ/l	Blade tip clearance as percent span, %
Φ	Airfoil camber angle, deg
Φ	Phase angle, deg

SUBSCRIPTS

h	hub
t	tip
m	metal
ΔP	Pressure difference across vane
ss	suction surface
ps	pressure surface
Δu	Streamwise fluctuating component
ΔV	Transverse fluctuating component

END

DATE
FILMED

3-82

DTIC